

1-1-1998

Neutron dosimetry, moderated energy spectrum, and neutron capture therapy for $^{25}\{45\}\text{R}^2\text{Cf}$ medical sources

Mark Joseph Rivard

Follow this and additional works at: http://digitalcommons.wayne.edu/oa_dissertations

Recommended Citation

Rivard, Mark Joseph, "Neutron dosimetry, moderated energy spectrum, and neutron capture therapy for $^{25}\{45\}\text{R}^2\text{Cf}$ medical sources" (1998). *Wayne State University Dissertations*. Paper 1207.

**NEUTRON DOSIMETRY, MODERATED ENERGY SPECTRUM, AND
NEUTRON CAPTURE THERAPY FOR ^{252}Cf MEDICAL SOURCES**

by

MARK JOSEPH RIVARD

DISSERTATION

Submitted to the Graduate School

of Wayne State University,

Detroit, Michigan

in partial fulfillment of the requirements

for the degree of

DOCTOR OF PHILOSOPHY


1998

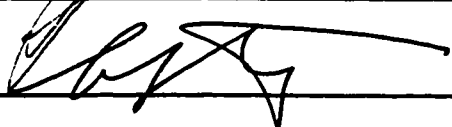
MAJOR: MEDICAL PHYSICS

Approved by:

Advisor

Date





R. L. Maughan

R. C. Martin

© COPYRIGHT BY
MARK JOSEPH RIVARD
1998
All Rights Reserved

DEDICATION

To my dearest wife Joanna Sganga, with all my love.

ACKNOWLEDGEMENTS

The research presented in this dissertation could not have been possible without the assistance and support of many individuals. The faculty and staff with whom I interacted at the WSU Department of Radiation Oncology, especially my advisor Dr. Jacek Wierzbicki, need to be recognized for their efforts and sense of humor. This work would have been deficient without critical review by my dissertation committee members, Drs. Colin Orton, Richard Maughan, Rodger Martin, and Robert Zamenhof. Drs. John Bigelow and Dick Haire, as well as Robert McMahon, Chuck Alexander, Bob Laxson, and Joe Knauer Jr. of Oak Ridge National Laboratory have embraced the goals of this work, and are appreciated for their practical insight, patience, and efforts. While at Fermilab, Drs. Dick Gustafson, James Bjorken, and Myron Campbell offered extraordinary opportunities in which my bent towards scientific research first took root and to whom I am forever grateful. Financial support was provided through a variety of sources; foremost was an AAPM/ASTRO sponsored medical physics residency fellowship acquired in collaboration with Dr. Orton. Various research trips were financed by the Fund for Medical Research and Education. Supplies were obtained in part through a Blue Cross Blue Shield of Michigan Grant #276-SAP/97. This publication is based on work performed in the Laboratory Graduate Research Participation Program sponsored by the U.S. Department of Energy, Office of Energy Research, and the Oak Ridge Institute for Science and Education. Finally, I thank my sister, Kris Rivard, and my parents, Dr. James Rivard and Mary Ann Rivard, for their unwavering support of my academic pursuits throughout the years.

TABLE OF CONTENTS

Dedication		ii
Acknowledgements		iii
List of Tables		v
List of Figures		vii
Chapter 1	Introduction to Dosimetry for ^{252}Cf Brachytherapy	1
Chapter 2	^{252}Cf Dosimetry: Protocol, Measurements, and Calculations	7
Chapter 3	Calculated Neutron Dosimetry for a General ^{252}Cf Source in Various Media Using AAPM TG-43 Formalism	27
Chapter 4	Calculation and Measurement of Thermal Neutrons Resulting from Moderation of ^{252}Cf Neutrons	43
Chapter 5	Calculated Boron Neutron Capture Dose and Moderated ^{252}Cf Neutron Energy Spectra in Brain Tissue	61
Chapter 6	Calculation and Measurement of Photon Dose from the ^{157}Gd Neutron Capture Reaction	74
Chapter 7	Health Physics and ^{252}Cf	86
Chapter 8	Feasibility of a High Dose Rate ^{252}Cf Source	106
Chapter 9	Dissertation Summary and Future Directions	124
References		128
Abstract		137
Autobiographical Statement		139

LIST OF TABLES

Table 2.1 Measured Nx values for various ionization chambers	12
Table 2.2 ^{252}Cf total transverse axis dose	15
Table 2.3 ^{252}Cf total off-axis dose	16
Table 2.4 T1 total dose when scanned along the ^{252}Cf source long-axis	16
Table 2.5 ^{252}Cf AT photon transverse axis dose	17
Table 2.6 Measured ^{252}Cf AT neutron transverse axis dose	17
Table 2.7 ^{252}Cf neutron kerma at 1 cm, and normalized kerma for other sources	18
Table 2.8 ^{252}Cf Neutron kerma (cGy/h- μg) at 0.5, 1.0, 2.0, and 5.0 cm, for various phantom materials	19
Table 2.9 Experimental parameters of Colvett <i>et al.</i> and this study	20
Table 2.10 Calculative parameters of Krishnaswamy and this study	21
Table 2.11 ^{252}Cf AT transverse axis neutron dose rate	24
Table 3.1 Air kerma rate, reference dose rate in muscle, and dose rate constant	30
Table 3.2 Reference dose rates for four source types and four materials	31
Table 3.3 Radial dose function 5th order polynomial fit	33
Table 3.4 Radial dose function non-linear fit	33
Table 3.5 Select calculated $F_N(r, \theta)$ for ^{252}Cf AT neutron dosimetry in water	34
Table 3.6 Comparison of reference neutron dose rates at r_0 and θ_0	41
Table 4.1 Intrinsic experimental parameters according to ASTM protocol	47
Table 4.2 Measured net TLD response for various radii from a ^{252}Cf AT source	51
Table 4.3 Comparison of MCNP relative thermal neutron fluence with net TLD results	55

Table 5.1	^{252}Cf brachytherapy and BNCR enhancement at 6.0 cm with a D_2O reflector	70
Table 5.2	BNCR dose enhancement for ^{252}Cf brachytherapy and 50 ppm ^{10}B	71
Table 6.1	GdNCR photon dosimetry kernel parameters for ^{252}Cf brachytherapy	79
Table 6.2	Photon dose enhancement (cGy/h-mg) for various ^{157}Gd loadings	82
Table 6.3	Photon dose enhancement for 160 ppm ^{157}Gd	84
Table 7.1	Mass densities of Clear-Pb[®] and acrylic	88
Table 7.2	Comparison of mass attenuation coefficients for Clear-Pb[®]	93
Table 7.3	Personnel badge results after a 5 hour exposure to 136.2 μg ^{252}Cf	101
Table 7.4	Dose-equivalent rates (mrem/h) outside the ^{252}Cf Suite	105
Table 8.1	Precipitation of ^{249}Cf and chemical volumes	113
Table 8.2	Precipitation yields using a ^{249}Cf radiotracer	114
Table 8.3	Maximum ^{252}Cf source strength for a variety of medical sources	123

LIST OF FIGURES AND DIAGRAMS

Figure 3.1	^{252}Cf AT, VariSource, $\mu\text{Selectron}$, and point source geometry factors	31
Figure 3.2	Radial dose function in water, brain, muscle, and A-150 plastic	32
Figure 3.3	Anisotropy factor for AT, $\mu\text{Selectron}$, VariSource, and point source	35
Figure 3.4	Neutron isodose distribution of a ^{252}Cf AT source in muscle	36
Figure 3.5	Neutron isodose distribution of a $\mu\text{Selectron}$ source in muscle	37
Figure 3.6	Neutron isodose distribution of a VariSource in muscle	37
Figure 3.7	Neutron isodose distribution of a ^{252}Cf point source in muscle	38
Figure 3.8	Comparison of neutron radial dose functions for ^{252}Cf sources	42
Figure 4.1	A-150 phantom for TLD irradiations	49
Figure 4.2	^{198}Au relative yields, $\text{Au}(n,\gamma)^{198}\text{Au}$, and $\text{Cd}(n,\text{abs})$ cross-sections	52
Figure 4.3	Neutron energy spectrum in water at a radius of 5.0 cm	53
Figure 4.4	Neutron energy spectra in water for various radii	54
Figure 4.5	Neutron energy spectra of A-150 plastic, brain, water, and muscle	54
Figure 5.1	Impact of ^{10}B loading on the calculated BNCR dose rate in a 15 cm diameter brain phantom	64
Figure 5.2	Impact of phantom size on the calculated BNCR dose rate in brain loaded with 30 ppm ^{10}B	64
Figure 5.3	High LET dose distribution for a clinical tumor model of BNCR enhanced ^{252}Cf brachytherapy	65
Figure 5.4	BNCR dose rate in a head phantom with / without a D_2O reflector	66
Figure 5.5	Normalized ^{252}Cf fast neutron and BNCR dose enhancements with a D_2O reflector	67

Figure 5.6	Moderated ^{252}Cf neutron energy spectrum at 0.5, 1.0, 2.0, 3.0, 4.0, and 5.0 cm with 30 ppm ^{10}B	67
Figure 5.7	Moderated ^{252}Cf neutron energy spectrum for ^{10}B loadings of 1 to 500 ppm at 5 cm	68
Figure 5.8	Moderated ^{252}Cf neutron energy spectrum for a variety of phantom sizes at 3 cm	68
Figure 6.1	GdNCR photon dose enhancement in brain for 100 and 1000 ppm ^{157}Gd	77
Figure 6.2	GdNCR photon dose kernel in water and brain	77
Figure 6.3	Radial dose functions for GdNCR photons and brachytherapy sources	79
Figure 6.4	Moderated ^{252}Cf neutron energy spectrum in brain, with / without 1000 ppm ^{157}Gd	80
Figure 6.5	GdNCR spatial distribution in brain for 100 and 1000 ppm loadings	81
Figure 6.6	Measured gadolinium photon dose enhancement ratio	82
Figure 7.1	MCNP calculation geometry	89
Figure 7.2	Calculated Clear-Pb [®] and plain acrylic photon μ/ρ	91
Figure 7.3	Calculated Clear-Pb [®] and plain acrylic neutron μ/ρ	91
Figure 7.4	Calculated μ/ρ for ^{252}Cf photons and neutrons	92
Figure 7.5	Comparison of Hubbell and Seltzer data with MCNP results	94

CHAPTER I

INTRODUCTION TO DOSIMETRY FOR ^{252}Cf BRACHYTHERAPY

In this dissertation, a series of Monte Carlo calculations and experimental measurements were performed to characterize ^{252}Cf emissions for clinical application in brachytherapy. The Monte Carlo radiation transport code was MCNP,¹ which can track neutrons, photons, and electrons and has been rigorously validated for a variety of problems.²⁻¹⁴ All these studies were reliant on accurate neutron transport and nuclear cross section data which are used by the author to perform the calculations presented in following chapters. For deep penetration problems, agreement between experimental results and those determined with MCNP are generally within a few percent.¹⁵ While the results determined herein are believed to be the most precise due to improvements in nuclear data and experimental techniques, the dosimetry of ^{252}Cf was first examined over 30 years ago.¹⁶⁻¹⁹

The first widely accessible ^{252}Cf dosimetry results²⁰⁻²³ were published by Krishnaswamy. The approach taken here was to model an encapsulated ^{252}Cf point source and sum the dose at various radii in a 30 cm diameter tissue-equivalent (TE) phantom as a means of determining dose distributions for an extended line-segment source. Monte Carlo calculations were performed where the total photon dose was calculated from the combination of ^{252}Cf prompt and delayed photons as well as the 2.225 MeV ^1H neutron capture photons. The neutron source was modeled as a Watt fission spectrum with an average neutron energy of 2.35 MeV. This spectrum differs from that of a Maxwellian which has been measured^{24,25} to be more representative of the ^{252}Cf neutron energy spectrum, and was suggested by Anderson.²⁶

The paper by Colvett *et al.*²⁷ was considered the first publication in which ^{252}Cf

dosimetry was measured in a reasonably accurate manner.^{19,28,29} In this study,²⁷ the ²⁵²Cf mixed-field dosimetry of a needle-type source was measured using paired proportional counters. Experimentally determined neutron dose rate measurements^{19,26,28,29} and calculations by others^{20,21,30,31} were significantly less than results of Colvett *et al.*²⁷ Due to improved measurements of nuclear data used for Monte Carlo determination of coefficients such as $K_{\text{MUSCLE}}/K_{\text{A-150}}$, $N(E_N)$, and $(W/e)_N/(W/e)_C$, and evolution of ICRU 45 neutron dosimetry formalism,³² improved experimental dosimetry results for ²⁵²Cf may now be obtained.

Two review articles by Anderson^{26,33} summarized the current status of measured and calculated dosimetry. A 20% agreement between calculative and measured ²⁵²Cf dosimetry was discussed.²⁶ The more recent article³³ concluded that the results of Colvett *et al.*²⁷ may be considered the best measured data available for ²⁵²Cf mixed-field dosimetry. However, the neutron dosimetry results of Colvett *et al.*²⁷ should be significantly reduced to account for exclusion of various factors such as differences in kerma between the TE ion chamber and human tissue. While the aim of modern dosimetry formalisms, such as TG-43,³⁴ is to determine the absorbed dose in water, determination of absorbed dose in human tissue from ²⁵²Cf neutrons must incorporate kerma coefficients as water is not tissue-equivalent.³²

Yanch and Zamenhof calculated the neutron and photon dose in water for a ²⁵²Cf Applicator Tube (AT) type source, and also calculated dose enhancement from the boron neutron capture reaction.²⁶ The calculations used ENDF-Vb libraries and Monte Carlo (MCNP3B) methods. Cross-section libraries for platinum, iridium, and palladium were not available so only bismuth was used to model the encapsulation and active source. The

capsule and source densities were set to 21.4 g/cm^3 and 9.8 g/cm^3 , respectively, in slight disagreement with that (21.51 g/cm^3 and 12.0 g/cm^3) expected for Pt/10%-Ir and Pd, respectively. However, these effects were expected to only impact results of photon dosimetry. A simple symmetrical source geometry of two right cylinders, 15 mm long 0.8 mm diameter and 23.1 mm long and 2.8 mm diameter, was used with no air, curved ends, or Bodkin eyelet. Fifty thousand histories were calculated in a cylindrical water phantom 60 cm long and 60 cm in diameter with a density of 1.000 g/cm^3 . An MCNP $S(\alpha, \beta)$ library was employed for accurate thermal neutron transport.²⁷ Up-to-date values of half-life and specific source strength, 2.645 year and $2.31 \times 10^6 \text{ n/s-}\mu\text{g}$, respectively, were used in these calculations. Spatial bins close to the source were bounded by planes separated by 4 mm and cylinders with radii (cm) of 0.14, 0.34, 0.54, 0.74, 0.94, etc. These relatively large bin sizes may have caused volume averaging which may have decreased the accuracy of the results obtained herein. Dosimetric results at radii (cm) of 0.25, 0.50, 0.75, etc., were interpolated from calculated results obtained using the above binning scheme.

It is clear that the current literature describing ^{252}Cf mixed-field dosimetry is lacking in both accuracy and scope. While there was general agreement, $\pm 20\%$, among the authors for fast neutron, photon, and $^{10}\text{B}(n, \alpha)$ dosimetry, a more rigorous analysis is necessary for future clinical applications. Consequently, the results presented within this dissertation are essential for proper delivery of ^{252}Cf brachytherapy.

An experimental dosimetry protocol was developed in Chapter 2 for measuring the total dose to muscle for ^{252}Cf . While this protocol was similar in form to that of ICRU 45, parameters were determined specific to ^{252}Cf brachytherapy. Using ionization chambers and a GM counter, results of experimentally measured mixed-field dosimetry were

compared with results of other investigators in the literature and those calculated using Monte Carlo methods. Neutron dosimetry calculations were performed for virtually all clinically relevant media in which ^{252}Cf brachytherapy could occur. The ^{252}Cf prompt neutrons were modeled with an isotropic Maxwellian neutron energy spectrum as presented in Equation 1. The unnormalized neutron energy spectrum, $N(E)$, is given in Equation 1 where E has units MeV and 1.42 is a fitting parameter.

$$N(E) = e^{-\frac{E}{1.42}} E^{1/2} \quad (1)$$

A distributed computing environment³⁵⁻³⁷ using MCNP4B¹ was used for all computations of neutron dosimetry and spectra. Absorbed dose from neutrons was calculated using the MCNP F6 heating tally which determined kerma in the material of interest based on energy deposition and microscopic cross-sections. In this method, the integral of energy deposition over all energies was equal to the total energy absorbed within a volume element (voxel). To obtain absorbed dose, the energy deposited in a given voxel was divided by the mass of the voxel. These efforts revealed a clinically significant 11.3% discrepancy in ^{252}Cf total dose rate between that measured herein and that in the literature. Differences in results between those in the literature and those determined herein from experiments and calculations were accounted for.

In Chapter 3 a modern dosimetry formalism similar to TG-43 was developed for clinical application of ^{252}Cf neutron brachytherapy. Capsule and source self-absorption was demonstrated to be negligible for calculations of ^{252}Cf neutron dose in water, A-150 TE plastic, and brain and muscle tissues. Should a ^{252}Cf high dose rate (HDR) source, or any medical source of other geometry be constructed, its neutron isodose distributions may be well approximated by the geometry factor for a line source model.

Chapter 4 presents the experimental and calculated results of thermal neutron flux from ^{252}Cf in a variety of media. In this section, the moderated ^{252}Cf thermal neutron flux was determined in a relative manner with LiF thermoluminescent dosimeters of varying $^6\text{Li}/\text{Li}$ enrichment. These studies involved relative measurements and were conducted in A-150 TE plastic to support calculative results determined for the same material. The specific aim of these experiments was to validate results of calculative neutron transport and the resulting spatial distribution of thermalized neutrons.

The purpose of Chapters 5 and 6 are to present the dose enhancement for neutron capture therapy (NCT) in combination with ^{252}Cf brachytherapy and demonstrate the feasibility of NCT in conjunction with ^{252}Cf fast neutron brachytherapy. Chapter 5 presents computational results of high linear energy transfer (LET) dose enhancement of ^{252}Cf brachytherapy following the boron-10 (^{10}B) neutron capture reaction (BNCR). A variety of ^{10}B loadings and phantom sizes were examined as a means to predict the enhancement that would be expected in clinical situations. With the current ^{10}B loadings available from drugs such as BPA-f, it appears that the dose enhancement from the BNCR is small in comparison to the doses obtained from ^{252}Cf brachytherapy. In Chapter 6, both computational and experimental means were used to measure the photon dose enhancement one would expect if gadolinium-157 (^{157}Gd) were introduced concurrently with ^{252}Cf brachytherapy. This study examined the non-specific photon dose component which would diminish the efficacy of ^{157}Gd enhanced ^{252}Cf brachytherapy.

In Chapter 7, the importance of shielding radiation workers or hospital personnel from ^{252}Cf emissions is presented, in light of no significant literature addressing the carcinogenic potential of low doses of ^{252}Cf . The utility of a proposed material for

shielding ^{252}Cf emissions as a means to diminish personnel exposure is analyzed.

Measurements with personnel radiation monitoring badges and bubble detectors were performed, and the maximum allowable patient load was determined from the measured exposure rates.

Efforts towards fabricating a ^{252}Cf HDR source are presented in Chapter 8.

Results of californium radiochemistry and metallurgical research at Oak Ridge National Laboratory (ORNL) are summarized. Also discussed are modified chemical procedures developed with ^{252}Cf stand-ins to produce sources with higher specific source strengths (mg/mm^3) than were currently available before these efforts. Examination of helium production from alpha decay was made for helium burst calculations to determine the maximum permissible ^{252}Cf loading for a variety of proposed HDR sources.

Chapter 9 is the final chapter which assimilates all the scientific results produced in the dissertation. Important advancements in ^{252}Cf mixed-field dosimetry and potential for NCT enhanced ^{252}Cf brachytherapy are discussed. Clinical logistics and radiation dosimetry for a miniature ^{252}Cf HDR source are addressed as a means to provide guidance for this important application of the ^{252}Cf radioisotope.

CHAPTER 2

²⁵²Cf DOSIMETRY: PROTOCOL, MEASUREMENTS, AND CALCULATIONS

I. INTRODUCTION

This chapter presents the experimental mixed-field dosimetry of ²⁵²Cf AT sources, and Monte Carlo calculations of the neutron dose from ²⁵²Cf sources in a variety of media. Ionization chambers and a miniature GM counter were used to measure the total and photon dose, respectively, close to ²⁵²Cf AT type sources. A brachytherapy neutron dosimetry protocol was formulated similar to the external neutron beam formalism presented in ICRU 45.³² Comparisons of experimental dosimetry were made with results of Colvett *et al.*²⁷ Finally, the neutron kerma in a variety of materials³⁸ and for varying depths within each material was calculated using Monte Carlo (MCNP)¹ methods and compared with other neutron sources.³⁹

II. MATERIALS AND METHODS

A. Experimental Studies

Two types of TE ion chambers and a miniature GM counter were used as the dosimetry equipment for the experimental studies. Measurements of Savannah River Laboratory-made (SRL) and ORNL-made ²⁵²Cf AT source dosimetry were made using a dosimetry protocol based on the ICRU 45 protocol for external neutron beam dosimetry.³²

TE Ion Chambers

For calibration of ORNL-made ²⁵²Cf AT source strengths, two types of TE ion chambers were used. The first type was manufactured by Far West Technology Inc. (FWT, model IC-17) and had a collecting volume of approximately 1 cm³. The second chamber (Exradin, model T1) had a 0.05 cm³ collecting volume. Both chambers were comprised of

A-150 TE plastic with methane-based TE gas flowing through each chamber. The TE gas was comprised of 3.2% N₂, 63.8% CH₄, and 33.0% CO₂ by volume.³⁸ A single Matheson type flow meter was used with a setting of 9.1 cm³/minute for controlling and monitoring the TE gas flow through each chamber. This flow rate displaced air within the chambers, yet did not cause over-pressurization.

Each chamber was placed in a 54 liter (28.6 x 30.8 x 61.1 cm³) thin-walled plastic water phantom. A plastic jig was used to centrally position each ion chamber among a circumferential array of AT sources with the chamber stem and source transverse axes parallel. The ion chambers were generally positioned such that measurements would obtain “away” data as the center of the ionization chamber collecting volume was placed at the active source mid-plane height. However, off-axis measurements were also taken using the smaller Exradin chamber due to its smaller collecting volume for better spatial discrimination. A high voltage bias of +500 volts was obtained from a power supply (Canberra, model #3102). An electrometer (Keithley, model 35617EBS) was used to measure the integrated charge over time, and the programmable time option (1 minute) was used for time consistency. Determination of charge leakage was measured before data was taken. Repeated one minute readings were taken to establish reproducibility.

Miniature GM Counter

A miniature GM counter (TGM Inc., model N115, ZP 1301 equivalent) was used to discriminate photon dose from the total dose as determined with the TE chambers. Due to its construction and the ²⁵²Cf neutron energies, the miniature GM counter was less sensitive to neutrons than to photons.^{32,40} GM counter photon sensitivity was determined through calibration with a ¹³⁷Cs source. The same water phantom and experimental setup

as used with the TE chambers was used; counts were integrated for 100 seconds using a scaler. Additionally, a ${}^6\text{LiF}$ cap was used in ${}^{252}\text{Cf}$ experimental measurements to minimize the effect of thermal neutrons. This approach, as compared to utilizing paired chambers such as A-150/TE and Mg/Ar chambers was chosen as the GM counter was less sensitive to low energy neutrons than the magnesium chambers.³²

A ${}^{252}\text{Cf}$ Brachytherapy Dosimetry Protocol

The goal here was to derive a modern dosimetry protocol similar to ICRU 45³² with parameters explicitly chosen for ${}^{252}\text{Cf}$ mixed-field dosimetry. This radiation source is unique as its fast neutrons are of relatively low energy and there is an appreciable photon dose component. In a mixed neutron-photon radiation field, the neutron and photon absorbed dose components can be determined from measurements made with two dosimeters. Since dosimeters which are sensitive to neutrons or photons alone are not available, it is necessary to use two dosimeters with differing sensitivities to neutrons and photons. The response of each dosimeter is related to the neutron and photon absorbed dose components in the following equations.

$$R'_T = k_T D_N + h_T D_G \quad (1)$$

$$R'_U = k_U D_N + h_U D_G \quad (2)$$

where:

R'_T = response of a dosimeter having approximately the same sensitivity to neutron and photon dose, divided by the chamber sensitivity used for calibration [cGy]

R'_U = response of a dosimeter having lower sensitivity to neutron than to photon dose, divided by the chamber sensitivity used for calibration [nC]

k_T = relative neutron sensitivity of a dosimeter having approximately the same sensitivity to neutron and photon dose [dimensionless]

k_U = relative neutron sensitivity of a dosimeter having lower sensitivity to neutron than to photon dose [dimensionless]

h_T	=relative photon sensitivity of a dosimeter having approximately the same sensitivity to neutron and photon dose	[dimensionless]
h_U	= relative photon sensitivity of a dosimeter having lower sensitivity to neutron than to photon dose	[dimensionless]
D_N	= fast neutron dose	[cGy]
D_G	= total photon dose	[cGy]

In the protocol that follows, the dosimeter having approximately the same sensitivity to neutron and photon dose was an A-150 TE ion chamber while the dosimeter having lower sensitivity to neutron than to photon dose was the miniature GM counter. From Equations 1 and 2, one may derive the mixed-field dosimetry formalism for total dose according to the European neutron dosimetry protocol⁴¹ for corrected responses.

$$R'_T = R_T (\prod k_M)_T d_T \alpha_C \quad R'_U = R_U (\prod k_M)_T d_T \alpha_C$$

where:

R_T	= unnormalized response of a dosimeter having approximately the same sensitivity to neutron and photon dose, divided by the chamber sensitivity used for calibration	[nC]
R_U	= unnormalized response of a dosimeter having lower sensitivity to neutron than to photon dose, divided by the chamber sensitivity used for calibration	[nC]
d_T	= replacement correction factor due to perturbation of the secondary charged particle energy fluence determined by replacing the phantom material with the ionization chamber	[dimensionless]
$(\prod k_M)_T$	= product of total correction factors	[dimensionless]
α_C	= photon calibration factor	[cGy/nC]

After manipulating the TE chamber response, rearrangement of terms, and separating common factors, Equations 3 through 6 follow.

$$R_T (\prod k_M)_T d_T G \alpha_C = (k_T D_N + h_T D_G) + (k_T D_G - k_T D_G) \quad (3)$$

$$R_T (\prod k_M)_T d_T G \alpha_C = (k_T D_N + k_T D_G) + (h_T D_G - k_T D_G) \quad (4)$$

$$R_T (\prod k_M)_T d_T G \alpha_C = (k_T D_N + k_T D_G) \left[1 + \frac{h_T D_G - k_T D_G}{k_T D_N + k_T D_G} \right] \quad (5)$$

$$R_T (\prod k_M)_T d_T G \alpha_C = k_T (D_N + D_G) \left[1 + \frac{D_G (h_T - k_T)}{(D_N + D_G) k_T} \right] \quad (6)$$

For simplicity, substitute in δ and sum the neutron and photon doses.

$$R_T (\prod k_M)_T d_T G \alpha_C = k_T (D_T) [1 + \delta] \quad \delta = \frac{D_G (h_T - k_T)}{(D_N + D_G) k_T} \quad (7)$$

where:

$$\begin{aligned} D_T &= \text{total (neutron + photon) absorbed dose} && [\text{cGy}] \\ \delta &= \text{response correction factor accounting for difference in} && [\text{dimensionless}] \\ &\quad \text{response of TE chamber for neutrons and photons} \end{aligned}$$

Finally, replace α_C with the appropriate coefficients used for chamber calibration,⁴¹ and replace the response (R_T) with measurement (M_T) to solve for total absorbed dose.

$$D_T = M_T (\prod k_M)_T d_T G N_X A_{WALL} (f)_C \frac{1}{k_T} \frac{1}{1 + \delta} \quad (8)$$

where:

$$\begin{aligned} M_T &= \text{raw electrometer reading} && [\text{nC}] \\ N_X &= \text{exposure calibration factor in } ^{60}\text{Co} && [\text{R/nC}] \\ A_{WALL} &= \text{wall absorption correction factor} && [\text{dimensionless}] \\ (f)_C &= \text{exposure-to-absorbed dose to reference tissue} && [\text{cGy/R}] \\ &\quad \text{correction factor} \end{aligned}$$

The relative neutron sensitivity of each TE chamber, k_T , was derived using formula 3.9 from ICRU 45,³² and is presented below in Equation 9. Using this formalism with appropriate values for ²⁵²Cf sources, the total dose was determined.

$$\frac{1}{k_T} = \frac{(\tau_{A-150,TE\text{ GAS}})_n}{\left[\left(\frac{L}{\rho} \right)_{TE\text{ GAS}}^{A-150} \right]_C} \frac{W_N}{W_C} \frac{(K_{MUSCLE} / K_{A-150})_n}{\left[\left(\frac{\mu_{en}}{\rho} \right)_{A-150}^{MUSCLE} \right]_C} \quad (9)$$

where:

$$\begin{aligned} (\tau_{A-150,TE\text{ GAS}})_n &= \text{A-150 wall to TE gas absorbed dose conversion factor} && [\text{dimensionless}] \\ L/\rho &= \text{ratio of mean restricted mass collision stopping power} && [\text{dimensionless}] \\ &\quad \text{for A-150 plastic ion chamber wall and TE gas} \\ W_N &= \text{energy per ion pair for } ^{252}\text{Cf neutrons} && [\text{J/C}] \\ W_C &= \text{energy per ion pair for } ^{60}\text{Co} && [\text{J/C}] \\ K_{MUSCLE} &= \text{neutron kerma in ICRU muscle} && [\text{J/kg}] \\ K_{A-150} &= \text{neutron kerma in A-150 dosimeter wall} && [\text{J/kg}] \end{aligned}$$

μ_{en}/ρ = mass-energy absorption coefficient for ICRU muscle or A-150 plastic ion chamber wall [cm²/g]

B. Monte Carlo Calculations

Neutron kerma was calculated with a distributed computing environment³⁵⁻³⁷ using Monte Carlo methods (MCNP)¹ for eleven materials. These materials were: water, A-150 plastic, PMMA, brain, muscle, fat, pancreas, lung, bone, skin, and blood. The elemental composition and mass densities of the materials were taken from ICRU 44 and the CRC Handbook.^{38,42} Each material subtended a 15 cm diameter spherical phantom in which a centrally placed isotropic neutron point source was positioned. Neutron kerma for each material was calculated for radii of 0.1 to 5.0 cm. Transport of at least 1 million particles was necessary to achieve relative errors (1 σ) of 0.1%.

III. RESULTS

A. Experimental Studies

Ion Chamber Calibration

Before measurements of ²⁵²Cf sources could begin, the exposure calibration factor, N_x , for each chamber was measured on the ⁶⁰Co total body irradiation unit. These N_x results agreed well ($\pm 2\%$) with previous measurements.³⁹ Results of the calibrations are presented in Table 1. As the Exradin T1 chamber had a volume approximately 5% of the

Table 1. Measured N_x values for various ionization chambers.

chamber	IC-17 #1	IC-17 #2	T1
exposure factor(R/nC)	2.933 \pm 0.029	3.051 \pm 0.031	45.53 \pm 0.46

two FWT IC-17 chambers, its N_x was expected to be approximately 20 times greater.

The Exradin N_x was approximately a factor 15 times larger than for the average FWT N_x .

Before measurements of the sources, determination of the system leakage was conducted.

None of the ion chambers produced leakage currents exceeding 10^{-15} A.

GM Counter Calibration

Specific to the GM counter, measurement of the dead-time was necessary as this instrument was used in pulse mode instead of current mode as were the other 5 chambers. Using a Tektronix 2440 digital oscilloscope, the dead-time was measured visually through identification of ensuing random pulses as 25-30 μ s; the 1985 FWT calibration data stated a dead-time of 30.6 μ s. Results were obtained using ^{252}Cf and ^{137}Cs sources, there was no discernable difference in measured dead-time using either isotope. Calibration was performed at distances of from 15 to 50 cm from a 122 mCi (4.51 MBq) ^{137}Cs source. With the non-paralyzable model,⁴³ the true count rate (n) could be calculated from the measured count rate (m) and knowledge of the 30.6 μ s dead-time (τ) using the following equation; background count rate was subtracted from all readings.

$$n = \frac{m}{1 - m\tau} \quad (10)$$

A calibration factor of $5.10 \pm 0.11 \times 10^{-7}$ cGy/ct, was determined with a ^{137}Cs Γ of 3.25 R-cm²/mCi-h, μ_{en}/ρ muscle to air ratio of 1.10, and photon W/e value of 33.97 J/C.

TE Ion Chamber Results

It was necessary to provide specific values for all of the parameters in Equations 8 and 9 to obtain the ^{252}Cf total dose as measured using the FWT and Exradin TE chamber current readings. Many parameters are recommended by ICRU 45,³² and are independent of the neutron source. An A_{WALL} value of 0.983 for the FWT IC-17 chambers and 0.992 for the Exradin T1 chamber is recommended.⁴⁴ The exposure-to-absorbed dose to reference tissue correction factor (f)_C was 0.966. Also according to ICRU 45,³² the value of the μ_{en}/ρ ratio for ICRU muscle and A-150 plastic is 1.001. A value of $(r_{\text{m,g}})_{\text{n}}/[(L/\rho)_{\text{m}}/(L/\rho)_{\text{g}}]_{\text{c}} = 1.00 \pm 0.02$ is recommended by ICRU 45 for neutrons.³² The product of total

correction factors $(\Pi k_M)_T$ was reduced to 1.0291, with C_{TP} (1.025) and C_{el} (1.004). The energy necessary to produce an ion pair in methane-based gas when irradiated by ^{60}Co is 29.3 eV. For recoil protons from ^{252}Cf neutrons, the energy per ion pair was calculated to be 31.65 eV based on convolving the ^{252}Cf neutron energy in ICRU muscle with methane-based TE gas data from Goodman and Coyne.⁴⁵ The W_N/W_C ratio was 1.080 for ^{252}Cf in methane-based TE gas. The ratio of the kerma for ICRU muscle to A-150 plastic was calculated to be 0.958 which did not change significantly with distance from the source ranging in the range from 0.5 to 5 cm. Using the above parameters in Equation 9, a value of 0.969 ± 0.02 for k_T was obtained, which was within 1% of a calculated k_T value of 0.96 for neutrons with energy between zero and 5 MeV determined by Waterman *et al.*⁴⁶ For a $d(4)+\text{Be}$ external neutron beam, k_T was measured as 0.945 ± 0.033 by Maughan *et al.* within an A-150 TE plastic phantom.⁴⁷

The ratio of photon dose to total dose ranged from 25% to 40%, with higher values occurring at larger distances.^{21,27,33,48} For distances of 1.0, 2.0, 3.0, and 5.0 cm, the ratio of photon to total dose was approximately 32, 33, 36, and 44% with values of 0.010, 0.011, 0.012, and 0.014 for δ . The value of h_T was unity. Using a fixed value of 0.011 for δ , the above parameters may be incorporated into Equation 8 with no significant radial dependence.

ICRU 45 defines the displacement correction factor, d_T , to account for differences in absorption and scattering of the primary radiation field due to replacing the phantom material with the gas cavity in the ion chamber.³² While it has been shown that for low energy neutrons and for small chambers that d_T may be assumed to be unity,⁴⁹ it is possible to separate a correction factor from this term which accounts for the dose gradient in the

phantom.⁵⁰ This was contemplated since one can orient the ²⁵²Cf sources in such a way that there are no dose gradients. Measurements of dose gradient were conducted for both chamber types through laterally offsetting each chamber by 5 mm. Within experimental uncertainties of these measurements, $\pm 1\%$, the dose gradient correction factor may be assumed unity for both chambers. For the IC-17 chambers, Equation 8 may be simplified as Equation 11. The value of 0.967 ± 0.008 differs by +1.4% of that, 0.954, determined by Colvett *et al.*²⁷ Total dose for the transverse axis was calculated for each TE chamber and is presented in Table 2 along side the values of Colvett *et al.*²⁷ and Krishnaswamy.²¹

$$D_T = 0.967 M_T (\prod k_M)_T N_X \quad (11)$$

Table 2. ²⁵²Cf total transverse axis dose.

distance (cm)	IC-17 #1 (cGy/h- μ g)	IC-17 #2 (cGy/h- μ g)	T1 (cGy/h- μ g)	Colvett <i>et al.</i> (cGy/h- μ g)	Krishnaswamy (cGy/h- μ g)
1.0			2.582	2.895	2.809
1.5			1.264	1.357	1.324
2.0	0.659	0.654	0.663	0.769	0.765
2.5			0.439	0.489	0.493
3.0	0.296	0.291	0.290	0.337	0.331
3.5			0.218	0.244	0.238
4.0			0.164	0.186	0.179
4.5			0.131	0.146	0.142
5.0	0.102	0.099	0.103	0.118	0.112

One should note that dosimetry data obtained by Colvett *et al.*²⁷ and Krishnaswamy²¹ were for an SRL-made *needle* source which was constructed in a markedly different manner than that of the SRL-made or ORNL-made AT sources. The T1 chamber had the smallest collecting volume of the chambers available, and was used to measure off-axis dosimetry. Using the same dosimetry formalism as for the transverse axis, total dose was determined. These results (Table 3) are compared with data of Colvett *et al.*²⁷ and Krishnaswamy.²¹

Table 3. ^{252}Cf total off-axis dose.

position (cm) along x away	T1 (cGy/h- μg)	Colvett <i>et al.</i> (cGy/h- μg)	Krishnaswamy (cGy/h- μg)
2.0 x 2.0	0.336	0.386	0.393
4.0 x 2.0	0.128	0.143	0.140
2.0 x 4.0	0.131	0.147	0.143
5.0 x 3.0	0.075	0.0839	0.079
3.0 x 5.0	0.077	0.0858	0.082
3.0 x 3.0	0.142	0.163	0.159
4.0 x 4.0	0.080	0.0902	0.086

As shown in Table 4, misalignment of the T1 chamber on this axis by 4–6 mm led to

Table 4. T1 total dose when scanned along the ^{252}Cf source long-axis.

position along x away (cm x cm)	T1 total dose (cGy/h- μg)	normalized dose
-0.6 x 2.0	0.618	0.932
-0.4 x 2.0	0.645	0.973
-0.2 x 2.0	0.660	0.995
0.0 x 2.0	0.663	1.000
0.2 x 2.0	0.655	0.989
0.4 x 2.0	0.639	0.964
0.6 x 2.0	0.613	0.925

errors of 4 to 8%. While it was a straightforward task of centrally positioning the chambers within the circumferential array of AT sources, properly aligning the chambers along the AT source long-axis was initially problematic as there were no outside demarkations on either the AT sources or the T1 chamber buildup cap. Therefore, the T1 chamber was manually scanned in the “along” axis to determine the centerline position; negative “along” values were towards the AT Bodkin eyelet end.

GM Counter Results

At an energy of approximately 4 MeV, an average k_U value of $0.6\% \pm 0.2\%$ was adopted for five different GM counter types studied.^{32,51} Results by Jones⁵¹ determined the k_U

value ($0.05\% \pm 0.05\%$) of a single GM counter type (ZP1320) for energies less than 1 MeV. From knowledge of the ^{252}Cf neutron energy spectrum⁵² and other studies,^{40,51} the N115 GM k_U value may be inferred as $0.2 \pm 0.2\%$. When accounting for measurement reproducibility and systematic uncertainties, a k_U value of zero may be used. Measured N115 photon dose results (Table 5) were obtained using the calibration factor of 5.10×10^{-7} cGy/ct, the dead-time correction of Equation 10, and a k_U value of zero.

Table 5. ^{252}Cf AT photon transverse axis dose.

distance (cm)	N115 (cGy/h- μg)	Colvett <i>et al.</i> (cGy/h- μg)	Krishnaswamy (cGy/h- μg)
1.0		0.845	0.925
2.0	0.2248	0.242	0.263
3.0	0.1093	0.118	0.120
4.0	0.0658	0.072	0.072
5.0	0.0436	0.050	0.049
6.0	0.0314	0.037	
7.0	0.0238		

Table 6. Measured ^{252}Cf AT neutron transverse axis dose.

distance (cm)	T1 - N115 (cGy/h- μg)	IC-17 - N115 (cGy/h- μg)
2.0	0.438	0.432
3.0	0.181	0.184
4.0	0.098	
5.0	0.059	0.0572

The ^{252}Cf neutron dose (Table 6) was obtained by subtracting the photon dose measurements taken with the N115 GM counter (Table 5) from the total dose determined with the T1 chamber and average of the two IC-17 TE chambers (Table 3).

B. Calculative Results

Table 7 presents the neutron kerma for 11 materials of interest at a clinically relevant

radial distance of 1.0 cm; ^{252}Cf neutron kerma is normalized to muscle at 1.0 cm for comparison with dosimetry properties of other neutron sources normalized to muscle.³⁹

Table 7. ^{252}Cf neutron kerma at 1 cm, and normalized kerma for other sources.

material	this study		Awschalom <i>et al.</i>		
	^{252}Cf kerma (cGy/h- μg)	^{252}Cf kerma muscle'	d(16) + Be muscle'	d + T muscle'	p(41) + Be muscle'
muscle	1.907 \pm 0.0011	1.000 \pm 0.0006	1.00	1.00	1.00
water	2.064 \pm 0.0012	1.083 \pm 0.0007	1.08	1.06	1.05
brain	2.009 \pm 0.0012	1.054 \pm 0.0006	1.05	1.04	1.04
skin	1.910 \pm 0.0011	1.002 \pm 0.0006	0.99	0.99	1.00
blood	1.928 \pm 0.0012	1.011 \pm 0.0007	0.98	0.98	0.98
fat	2.183 \pm 0.0013	1.145 \pm 0.0007	1.13	1.13	1.16
pancreas	1.997 \pm 0.0012	1.047 \pm 0.0006	0.96	0.97	0.96
lung	1.943 \pm 0.0012	1.019 \pm 0.0006	0.97	0.98	0.98
bone	0.809 \pm 0.0005	0.424 \pm 0.0003	0.44	0.52	0.52
A-150	2.005 \pm 0.0012	1.053 \pm 0.0006	1.02	1.04	1.07
PMMA	1.654 \pm 0.0010	0.868 \pm 0.0005	0.83	0.88	0.90

For illustrative purposes, the impact of material on the moderated ^{252}Cf neutron spectrum is presented in Table 8. Convolution of various kerma coefficients⁵³ was performed on the moderated neutron energy spectrum in water, A-150 plastic, brain,³⁸ and muscle³⁸ at radial distances of 0.5, 1.0, 2.0, and 5.0 cm. The merit of this approach permitted, for example, determination of kerma to muscle in water where the kerma coefficients⁵³ for muscle were convolved with the moderated ^{252}Cf neutron energy spectrum in a water phantom.

IV. DISCUSSION

Due to moderation of the ^{252}Cf neutron spectrum, there was a slight dependence on the W_N/W_C ratio and water to muscle kerma ratios as a function of depth. However, these effects for varying depths of 0.5 to 5.0 cm were typically less than 3%. The most significant parameter change was in δ . As δ was relatively small, variations of δ by even

40% (0.010 to 0.014) caused a shift in total dose calculations of only 0.4% which was not considered significant. Comparisons between the average total dose measurements with

Table 8. ^{252}Cf Neutron kerma (cGy/h- μg) at 0.5, 1.0, 2.0, and 5.0 cm, for various phantom materials.

kerma / radii (cm)	brain phantom	muscle phantom	water phantom	A-150 phantom
brain 0.5	8.054	8.070	8.038	8.107
muscle 0.5	7.613	7.628	7.598	7.664
water 0.5	8.311	8.327	8.295	8.366
A-150 0.5	7.956	7.971	7.941	8.007
brain 1.0	2.009	2.016	2.001	2.031
muscle 1.0	1.900	1.907	1.892	1.921
water 1.0	2.072	2.080	2.064	2.095
A-150 1.0	1.984	1.992	1.977	2.005
brain 2.0	0.483	0.487	0.480	0.490
muscle 2.0	0.457	0.461	0.454	0.464
water 2.0	0.497	0.502	0.495	0.505
A-150 2.0	0.477	0.481	0.474	0.484
brain 5.0	0.0591	0.0607	0.0591	0.0588
muscle 5.0	0.0561	0.0576	0.0561	0.0558
water 5.0	0.0605	0.0623	0.0606	0.0602
A-150 5.0	0.0584	0.0600	0.0585	0.0581

the two IC-17 chambers and the T1 chamber were within 1% for the three common measurement distances of 2.0, 3.0, and 5.0 cm. However, there were significant differences between the results of Colvett *et al.*,²⁷ Krishnaswamy,²¹ and those determined herein.

A. Comparison of Experimental Measurements with Data of Colvett *et al.*

Experimental results obtained herein were compared with measured ^{252}Cf dosimetry of Colvett *et al.*²⁷ For both the on- and off-axis measurements, the total dose measured with the T1 chamber was $11.3 \pm 2.0\%$ less than that determined by Colvett *et al.*²⁷ However, this discrepancy may be explained when details of each experimental setup are examined (Table 9) where many of the parameters used for derivation of total dose are presented.

Table 9. Experimental parameters of Colvett *et al.* and present this study.

parameter	Colvett <i>et al.</i>	this study (IC-17 and T1)
phantom size	0.200 m ³	0.054 m ³
phantom composition	0.109 g/cm ³ H 0.13 g/cm ³ C 0.79 g/cm ³ O	0.112 g/cm ³ H 0.888 g/cm ³ O
phantom temperature	22°C ?	18°C
chamber volume(s)	0.0018 cm ³	1.0 and 0.05 cm ³
chamber wall thickness	3.4 mm	4.1 mm
detector type	proportional counter	ionization chamber
chamber fill gas	55% C ₃ H ₈ , 39.6% CO ₂ , 5.4% N ₂	63.84% CH ₄ , 32.97% CO ₂ , 3.19% N ₂
$(W/e)_N / (W/e)_C$	1.057	1.080
$K_{\text{MUSCLE}} / K_{A-150}$	not included	0.958
$(\mu_{\text{en}}/\rho)_{\text{MUSCLE}} / (\mu_{\text{en}}/\rho)_{A-150}$	not included	1.001
d_T	not included	1.000
A_{WALL}	not included	0.983 and 0.992
²⁵² Cf source strength	~ 5 µg	326.23 µg
²⁵² Cf source type	needle	Applicator Tube
²⁵² Cf half-life	2.58	2.645
²⁵² Cf source arrangement	along-away (gradient)	cylindrical symmetry (uniform)

In a ²⁵²Cf dosimetry review by Anderson,²⁶ many of the differences in experimental setups were first examined. Anderson²⁶ derived a 7% dose over-estimation obtained by Colvett *et al.*,²⁷ accounted for in part by exclusion of $K_{\text{MUSCLE}} / K_{A-150}$. An additional discrepancy of 2% is expected when accounting for the difference in the calculated ratio of W/e for neutrons and photons (1.057) of Anderson²⁶ and Colvett *et al.*²⁷ versus the value used herein (1.080). Finally, an approximate 2% under-estimation in source strength was derived from the half-life (2.58 years) used by Colvett *et al.*²⁷ and that (2.645 years) currently accepted, thus forcing calculations of both neutron and photon dose rates (cGy/h-µg) to be 2% high. Upon comparison of the average total dose rates of 0.663,

0.290, 0.164, and 0.103 cGy/h- μg obtained on-axis at 2.0, 3.0, 4.0, and 5.0 cm using the T1 chamber with those of Colvett *et al.*,²⁷ 0.769, 0.337, 0.186, and 0.118 cGy/h- μg at the same distances, and by including this 11% over-estimation, it is evident the ratio of results obtained herein to those of Colvett *et al.*²⁷ were 0.969, 0.967, 0.991 and 0.981 at 2.0, 3.0, 4.0 and 5.0 cm, respectively. The average of these ratios was 0.977 which may be considered good agreement due to the aforementioned differences in Table 9, the source strength calibration accuracy ($\pm 3\%$) determined by SRL and ORNL, and in light of clinically acceptable source strength uncertainties according to the guidelines ($\pm 3\%$) set forth in TG-56.⁵⁴ Due to improved measurements of nuclear data used for determination of factors such as $K_{\text{MUSCLE}} / K_{\text{A-150}}$, $N(E_N)$, and $(W/e)_N / (W/e)_C$, and application of ICRU 45³² dosimetry formalism, the results obtained herein were determined to be more reliable than those obtained by Colvett *et al.*²⁷

B. Comparison of Calculated Neutron Dosimetry Results with Krishnaswamy Data

As was the case for the comparison with Colvett *et al.*,²⁷ there were many differences between the Monte Carlo results obtained herein and those obtained by Krishnaswamy.²¹ These differences are presented in Table 10, along with the appropriate correction factors

Table 10. Calculative parameters of Krishnaswamy and this study.

parameter	Krishnaswamy	this study	correction factor			
			0.5,	1.0,	2.0,	5.0 cm
²⁵² Cf source spectrum	Watt fission	Maxwellian	1.049,	1.050,	1.055,	1.076
specific ²⁵² Cf strength	2.34×10^6 n/s- μg	2.314×10^6 n/s- μg	1.011,	1.011,	1.011,	1.011
²⁵² Cf source geometry	needle	point	0.655,	0.858,	0.957,	0.993
¹ H proportion	10.5 %	10.2 %	1.029,	1.029,	1.029,	1.029
voxel bin spacing	0.50 cm	0.01 cm	1.083,	1.021,	1.005,	1.001

to compare the two calculative studies. A Maxwellian spectrum was used in this work to model the ²⁵²Cf neutrons while Krishnaswamy²¹ employed a Watt fission spectrum as

presented in Equation 12 where E has units MeV.

$$N(E) = \sinh(2E)^{1/2} e^{-0.88E} \quad (12)$$

Comparing the moderated neutron kerma in muscle using the Krishnaswamy Watt fission spectra with the kerma determined when using a Maxwellian spectrum, a difference in neutron kerma to muscle was expected. At radii of 0.5, 1.0, 2.0, and 5.0 cm, the correction factors used to compare kerma calculated using the two different neutron energy spectra were 1.049, 1.050, 1.055, and 1.076, respectively. Krishnaswamy²¹ employed a specific source strength of 2.34×10^6 n/s- μ g instead of the more recently determined value of 2.314×10^6 n/s- μ g,⁵⁵ which resulted in a 1.1% correction factor. As Krishnaswamy²¹ modeled an extended (*needle*) source, $L = 15$ mm, instead of a point source, geometry factors³⁴ were necessary to compare the two studies. A simple correction (1.029) was applied for the different mass percentages of hydrogen used in the calculations; 10.5% by Krishnaswamy and 10.3% in the present work. Finally, Krishnaswamy²¹ used excessively large voxels near the ²⁵²Cf source where volume averaging within the voxel would markedly decrease the results.²⁶ The effect of these corrections on Krishnaswamy's results²¹ was 8.3, 2.1, 0.5, and 0.1% for radial distances of 0.5, 1.0, 2.0, and 5.0 cm, respectively.²⁶ The ratio of MCNP results to those of Krishnaswamy²¹ after implementing the corrections of Table 10 were 1.012, 0.969, 0.970, and 1.017 at radii of 0.5, 1, 2, and 5 cm, respectively, or on average 0.992 ± 0.027 . This agreement was within the Monte Carlo uncertainties (~ 4%) of Krishnaswamy; uncertainties in the present Monte Carlo calculations are negligible by comparison.

C. Comparison of Calculative Results with Data of Awschalom *et al.*

From Table 7, one can make comparisons of the ²⁵²Cf neutron kerma in a variety of

clinically and radiologically interesting materials. Due to the higher hydrogen mass content of fat (11.4%) and water (11.1%), respectively, the kermas relative to muscle were significantly larger, 14.5 and 8.3 %, respectively, in these two materials. Similarly, the relative hydrogen content of bone (3.4%) and PMMA (8.1%) reduce the neutron kerma to 42.4% and 86.8%, respectively, compared to muscle.

From Table 7, comparisons may also be made between different neutron sources.³⁹ Kermas normalized to muscle were arranged in order of increasing average neutron energy. While there were general similarities in relative kermas among the various neutron sources, there were significant differences, 9 and 4% respectively, between ²⁵²Cf and the external beam sources for pancreas and lung. From ICRU 44,³⁸ a 10.6 and 10.3% mass hydrogen content was used for pancreas and lung, respectively. As cited in Awschalom *et al.*,³⁹ the pancreas and lung compositions were 9.7 and 9.9% mass hydrogen, respectively, as taken from ICRP 23.⁵⁷ These differences in hydrogen content had the correct sign and magnitude as would be expected from the differences in kerma between the neutron sources. The pancreas and lung were the only materials with different ICRU 44 and ICRP 23 hydrogen mass content greater than 0.2%.^{38,57} Of note are the similarities of neutron kerma for A-150 plastic and brain tissue for the ²⁵²Cf source. Therefore, A-150 plastic may be considered an optimal material with which to measure ²⁵²Cf fast neutron dosimetry in the brain tissue. Additionally, the 5% kerma enhancement between brain and muscle due to a 5% increase in hydrogen content may not be considered detrimental for future applications such as cerebral ²⁵²Cf brachytherapy.

D. Impact of Kerma Coefficients and Phantom Material on Neutron Kerma

Table 8 lists the neutron kerma for various depths in two clinical media and two dosimetry

materials. Through comparing data horizontally for all depths, the impact of phantom material on neutron kerma is much less important than choice of kerma coefficients as evidenced in vertical comparisons. For example, at a depth of 1.0 cm, the variation in neutron kerma among the four phantom materials when employing kerma coefficients⁵³ for muscle amounts to 0.6%. However, when using neutron transport in a muscle phantom and varying the kerma coefficients, the variation then becomes 3.6%. Even at a depth of 5.0 cm where the ²⁵²Cf neutrons are significantly moderated, the variations were 1.4 and 3.2%, respectively. Consequently, the impact of neutron transport through a given material was less important than choice of kerma coefficients.

E. Comparison of Calculated and Experimental Neutron Dose Rates

Using a geometry factor³⁴ with $L = 15$ mm to compare point source calculations and extended source measurements, one may convert the MCNP calculated neutron dose rate to that for an extended source such as the AT. This is presented in Table 11 where the ratio of geometry factors for a point source and extended source ($L = 15$ mm) were 0.9567, 0.9799, 0.9885, and 0.9926 at distances of 2.0, 3.0, 4.0, and 5.0 cm, respectively.³⁴ For comparison, measured neutron rates of AT sources are presented in Table 11, as are ratios of experimental neutron dose rates to those calculated with MCNP.

Table 11. ²⁵²Cf AT transverse axis neutron dose rate.

distance (cm)	T1 - N115 (cGy/h- μ g)	IC-17 - N115 (cGy/h- μ g)	MCNP (cGy/h- μ g)	T1 - N115 ratio to MCNP	IC-17 - N115 ratio to MCNP
2.0	0.438 \pm 0.021	0.432 \pm 0.011	0.44030 \pm 0.00035	0.995 \pm 0.050	0.982 \pm 0.025
3.0	0.181 \pm 0.009	0.184 \pm 0.005	0.18764 \pm 0.00017	0.965 \pm 0.048	0.981 \pm 0.025
4.0	0.098 \pm 0.005		0.097809 \pm 0.00011	1.002 \pm 0.050	
5.0	0.059 \pm 0.003	0.057 \pm 0.001	0.056656 \pm 0.000068	1.041 \pm 0.052	1.005 \pm 0.025

From inspection of Table 11, the neutron dose rate as derived using the combination of

FWT chambers and GM counter were in approximately the same level of agreement with

MCNP results as the neutron dose rate derived using the combination of Exradin chamber and GM counter. The average ratio for the FWT chambers and GM counter combination was 0.989 while the average ratio for the Exradin chamber and GM counter combination was 1.001. Measurements with both chamber combinations agreed with the calculated neutron dose rates at all distances within the uncertainties.

F. Clinical Use of Dosimetric Data

The Wayne State University (WSU) Department of Radiation Oncology is currently the only institution in the Western Hemisphere which uses ^{252}Cf for clinical use. Clinical practice of this modality was relocated from the University of Kentucky (UK) where extensive studies were performed with ^{252}Cf AT sources to determine the relative biological effectiveness (RBE) of ^{252}Cf neutrons for a variety of clinical sites.^{58,59} At UK, a neutron RBE of 6 was used for multifractionated treatments of malignant soft tissue. This was determined using an RBE of 1 for ^{252}Cf photons. As the photon dose contributes approximately 30% of the total dose at clinically relevant distances, the dose-equivalent using the UK RBE values may be determined as follows where the proportion of photon dose-eq is 6.7% of the total dose-eq.

$$\text{Dose-eq} = \text{RBE}_N (D_N) + \text{RBE}_G (D_G) \quad (13)$$

$$\text{Dose-eq} = 6 (D_N) + 1 (D_G) \quad (14)$$

At WSU, an RBE_N of 7 is used and patients are treated twice a day with typically 7 fractions.⁶⁰ Clinical prescriptions account only for the neutron dose and the photon dose is neglected. To illustrate the impact of this methodology, the total dose-eq is examined.

$$\text{Dose-eq} = 7 (D_N) + 1 (D_G) \quad (15)$$

The effect of this prescription choice by WSU physicians appears to over-estimate the total dose-eq by 8.9% as compared to the UK treatments. If the dosimetry data presented herein is used in favor of the Colvett *et al.*²⁷ data as modified by Anderson,²⁶ a decrease in the total dose-eq of 11% would occur if the WSU ²⁵²Cf prescription, using an RBE_N of 6, remained constant, and this would cancel out to some extent the total dose-eq over-estimation (8.9%) currently in effect as compared to the UK prescriptions where the majority of the clinical results were obtained.

If an HDR ²⁵²Cf source (1 - 5 mg) is used, it is expected that the RBE_N would diminish to approximately 3.5.⁶¹⁻⁶³ Using Equation 13 with this new RBE_N value, it is evident that an 11% under-estimation in the total dose-eq would be made if the photon dose-eq was neglected by WSU physicians. As the magnitude of these changes in dose-eq for AT and HDR sources are clinically relevant, it is imperative that consensus occurs between physicians and physicists to assure accurate prescription for ²⁵²Cf brachytherapy.

V. CONCLUSION

For the first time, an ICRU 45-like dosimetry protocol was applied to ²⁵²Cf brachytherapy sources. Kerma of ²⁵²Cf neutrons, as determined using Monte Carlo methods, was analyzed for a variety of clinically relevant tissues and dosimetry media. Measurements using a GM counter and two types of TE chambers were used to determine the mixed-field dosimetry of ²⁵²Cf AT sources. Comparisons were made between results of Colvett *et al.*,² and Krishnaswamy¹⁸ with factors derived to permit reasonable comparisons.

CHAPTER 3

CALCULATED NEUTRON DOSIMETRY FOR A GENERAL ^{252}Cf SOURCE IN VARIOUS MEDIA USING AAPM TG-43 FORMALISM

I. INTRODUCTION

This chapter presents the calculative neutron dosimetry of ^{252}Cf sources in a variety of media. A general dosimetry equation using AAPM Task Group 43 (TG-43)³⁴ formalism and dosimetry results from Monte Carlo calculations is created using the physical dimensions of a ^{252}Cf source and phantom coefficients for water, brain, muscle, and A-150 plastic. Results are compared to those of the literature.

II. MATERIALS AND METHODS

A distributed computing environment³⁵⁻³⁷ using MCNP¹ was used for the computation of neutron dosimetry and flux. Absorbed dose from neutrons was calculated using the MCNP heating tally which determined absorbed dose deposited in the material of interest based on energy deposition and microscopic cross-sections. In this method, the integral of energy deposition over all energies was equal to the total energy absorbed within a voxel. To obtain absorbed dose, the energy deposited in a given voxel was divided by the mass of the voxel. Four dosimetry materials were studied. The first was light water with 0.015% atomic abundance ^2H relative to ^1H , and a mass density of 0.998 g/cm^3 . Brain and muscle materials, with compositions described in ICRU 44,³⁸ were studied as these are clinical materials in which ^{252}Cf neutron brachytherapy may be performed. A-150 plastic was also studied as it is a useful neutron dosimetry material for experimental measurements.^{32,38}

For calculations of neutron dose using MCNP, four ^{252}Cf source models were analyzed. These were the AT source as made by ORNL, a proposed HDR $\mu\text{Selectron}$

source, a proposed HDR VariSource, and a hypothetical point source. For the first three source models, neutrons were emitted from a cylindrical active element which was modeled as the Pd:CeF₂O₃ ceramic-metal (cermet) matrix. The active element of the AT source was 15 mm long and 1.3 mm in diameter, and encapsulated in a 2.8 mm diameter and 23.1 mm long cylinder comprised of Pt/Ir-10% mass.⁶⁴ The proposed HDR μ Selectron source active element was modeled as a 3.5 mm long and 0.6 mm diameter Pd:CeF₂O₃ cermet, and encapsulated in a 4.7 mm long and 1.1 mm diameter 316 stainless steel tube.⁶⁵ The proposed HDR VariSource had a Pd:CeF₂O₃ cermet active element 0.34 mm in diameter and 10.0 mm long, and was contained in a nickel-titanium (nitinol) capsule 12 mm long and 0.57 mm in diameter.⁶⁶ The hypothetical point source was bare, and did not incorporate any encapsulating material.⁵² All four source models employed an isotropic Maxwellian neutron energy spectrum as recommended by Anderson.²⁶

The active element of each of the four aforementioned source models was centrally placed within a 30 cm diameter phantom. Spherical shells of increasing diameter were positioned around each source, these spheres were divided into conics so as to determine both radial and anisotropic effects of neutron dose distributions. The sampling space was chosen to provide results which could later be used for dosimetry analysis using TG-43 formalism. The general TG-43 dosimetry equation³⁴ is presented in Equation 1 where the reference dose rate is defined at a radius, r_0 , of 1 cm and angle, θ_0 , of 90° for any material. The reference dose rate is the product of the air kerma strength and dose rate constant.

$$\dot{D}(r, \theta) = S_K \Lambda g(r) \left[\frac{G(r, \theta)}{G(r_0, \theta_0)} \right] F(r, \theta) \quad (1)$$

where:

$$\dot{D}(r, \theta) = \text{neutron dose rate} \quad [\text{cGy/h-}\mu\text{g}]$$

r	= the radial distance from source center to point of interest	[cm]
θ	= angle from source long axis to point of interest	[radians]
S_K	= air kerma strength	[cGy-cm ² /h- μ g]
Λ	= dose rate constant	[cm ⁻²]
$g(r)$	= radial dose function	[dimensionless]
$G(r, \theta)$	= geometry factor	[cm ⁻²]
$G(r_0, \theta_0)$	= geometry factor at $r = 1$ cm, and $\theta = 90^\circ$	[cm ⁻²]
$F(r, \theta)$	= anisotropy function	[dimensionless]

In this study, parameters describing the dose rate constant, radial dose function, geometry factor, and anisotropy function were determined for the four source types: AT, μ Selectron, VariSource, point, and four materials: water, brain, muscle, A-150 plastic. Data from each Monte Carlo run was analyzed for statistical uncertainty. Those calculative runs that necessitated improved statistical accuracy were continued to meet the desired 0.1 percent relative error criterion. In general, each calculative run required at least 10^8 particle histories.

III. RESULTS

A. Air Kerma Strength

The neutron air kerma strength, S_K , was calculated using neutron transport of a Maxwellian neutron energy spectrum in free space with all four sources. The neutron kerma coefficients for air from Caswell *et al.*⁵³ were convolved with the calculated neutron energy flux at a distance of 1 meter in free space on the transverse axis to yield the air kerma rate. As a finite region was necessary with which to tally results over, the region from 82° to 98° ($90^\circ \pm 8^\circ$) at 1 meter was chosen. Here, 10^8 particles were transported which yielded relative errors in each energy bin of typically 0.5% with a total relative error of 0.02% over all energies studied, 1 eV to 20 MeV. The average air kerma rate for all four sources was 3.961×10^{-15} cGy/neutron or 3.060×10^{-5} cGy/h- μ g with only a 0.05%

variation among the four source types.. A specific neutron rate⁵⁵ of 2.314×10^6 neutrons per second per μg ^{252}Cf was used. By multiplying the air kerma rate by the square of the distance at which it was determined, the air kerma strength, $0.306 \text{ cGy-cm}^2/\mu\text{g-h}$, was found. The air kerma strength conversion factor was calculated to be $3.268 \text{ U}/\mu\text{g}$.

B. Dose Rate Constant

According to TG-43, water should be the reference medium for describing dose rate distributions around brachytherapy sources.³⁴ While this practice is adequate for photon sources, it is inadequate for brachytherapy neutron sources such as ^{252}Cf as there are significant differences (8%) in neutron kerma between water and human tissue.^{38,52,53,56} Therefore, the reference material of muscle³² is employed for calculation of the dose rate constant for the four sources, and is presented in Table 1. For comparison, the reference dose rates in all four materials for each source type are presented in Table 2. Similarities in dose rates between the point source and the $\mu\text{Selectron}$ were expected as the $\mu\text{Selectron}$ was the shortest extended-source model examined in this study.

Table 1. Air kerma rate, reference dose rate in muscle, and dose rate constant.

source type	air kerma rate (cGy/h- μg)	reference dose rate in muscle (cGy/h- μg)	dose rate constant (cm^{-2})
AT	3.058×10^{-5}	1.636	5.350
$\mu\text{Selectron}$	3.061×10^{-5}	1.887	6.165
VariSource	3.059×10^{-5}	1.768	5.780
point source	3.061×10^{-5}	1.907	6.230

C. Geometry Factor

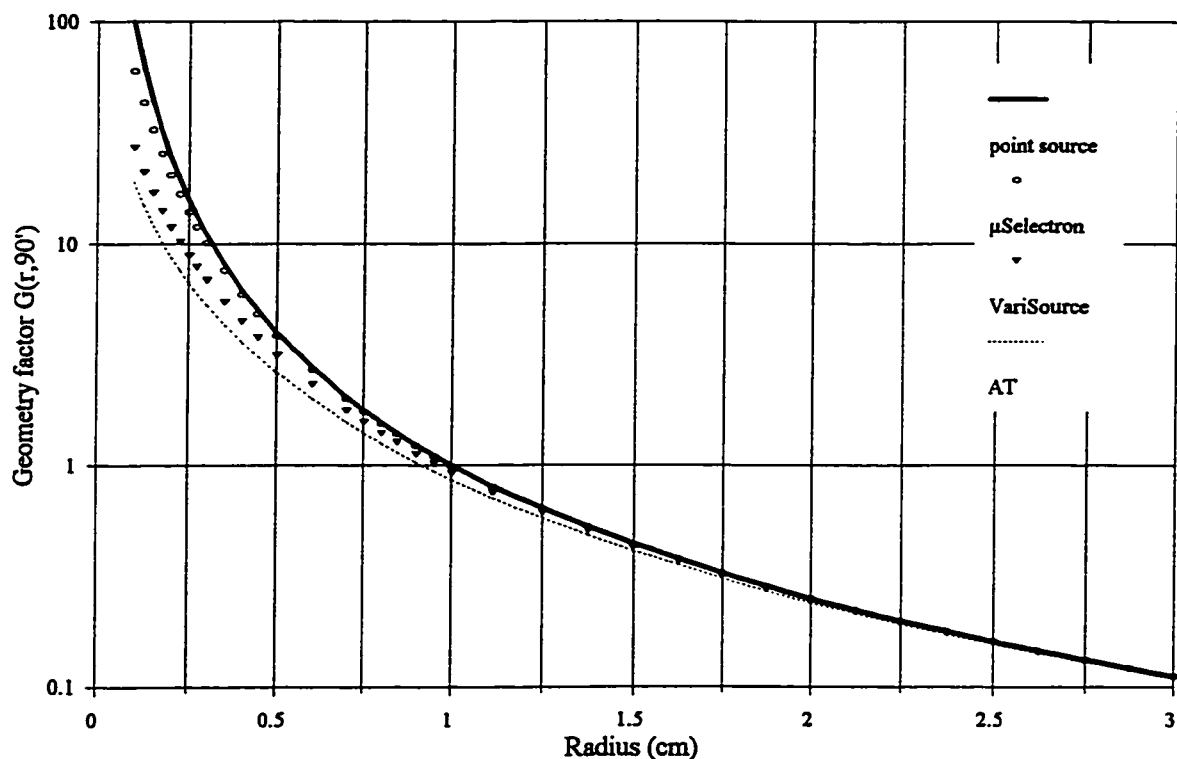
The general form of the geometry factor, $G(r, \theta)$, is given in Equation 2. The definition of variables r and θ are identical to that of Equation 2, while L is the active source length.

Table 2. Reference dose rates for four source types and four materials.

source type	phantom material			
	water (cGy/h- μ g)	brain (cGy/h- μ g)	muscle (cGy/h- μ g)	A-150 plastic (cGy/h- μ g)
AT	1.772	1.723	1.636	1.722
μ Selectron	2.045	1.989	1.887	1.987
VariSource	1.916	1.863	1.768	1.861
point source	2.066	2.009	1.907	2.007

$$G(r,\theta) = \frac{\arctan\left[\frac{L}{2r \sin\theta} + \cot\theta\right] + \arctan\left[\frac{L}{2r \sin\theta} - \cot\theta\right]}{L r \sin\theta} \quad (2)$$

A plot of the geometry factor on the transverse axis for the four sources studied is shown in Figure 1. From Equation 2, the reference geometry factors, $G(r_0, \theta_0)$, for the AT, μ Selectron, VariSource, and point sources are 0.858, 0.990, 0.927, and 1, respectively.

**Figure 1.** ^{252}Cf AT, VariSource, μ Selectron, and point source geometry factors.

D. Radial Dose Function

The radial dose function was determined for all four source types and four phantom materials. There were no significant differences in the radial dose function among the four source types studied, and the average radial dose function is presented in Figure 2. As suggested by Meisberger *et al.*,⁶⁷ the radial dose function may be fit to a polynomial equation for manipulation in applications such as clinical treatment planning. The coefficients for a 5th order polynomial fit for the four phantom materials are given in Table 3 for radial distance r in units cm. The clinical treatment planning workstation used at the ROC employed a non-linear equation (3) to fit the radial dose function data. The parameters α and β have units cm^{-2} ; γ is unitless.

$$g(r) = \gamma \frac{(1 + \alpha r^2)}{(1 + \beta r^2)} \quad (3)$$

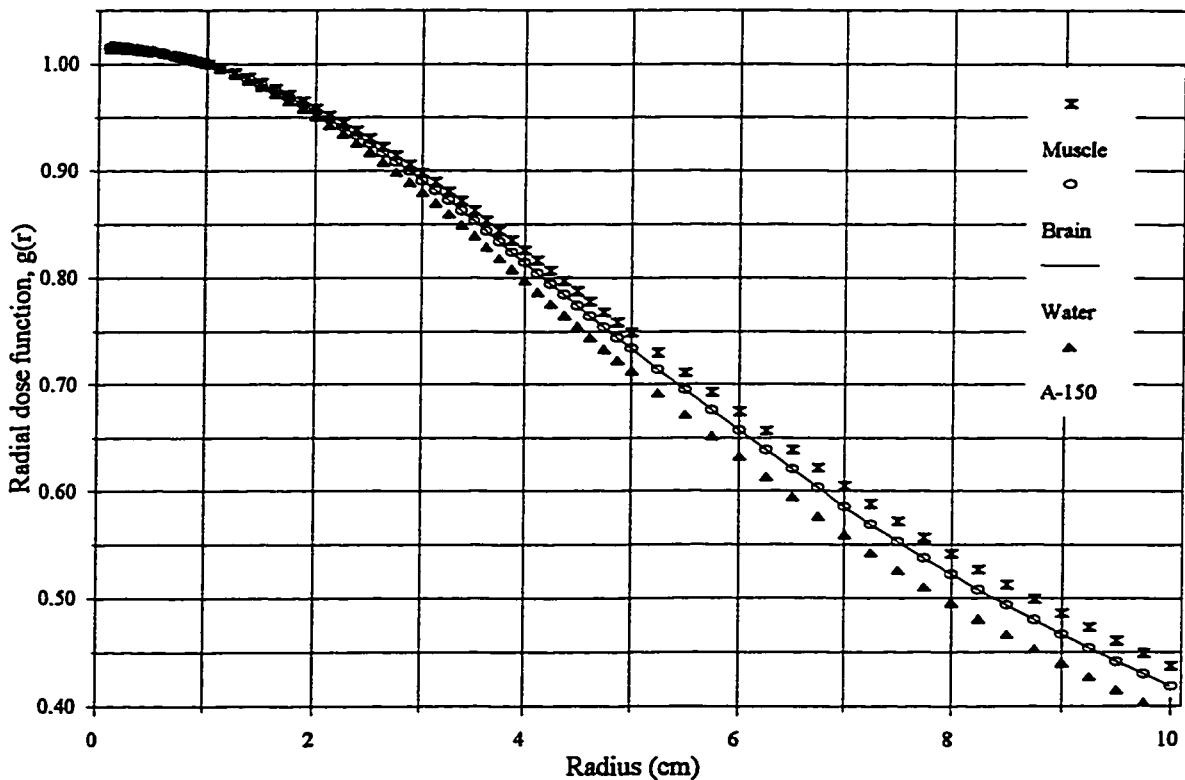


Figure 2. Radial dose function in water, brain, muscle, and A-150 plastic.

Table 3. Radial dose function 5th order polynomial fit.

polynomial coefficients	phantom material			
	water	brain	muscle	A-150 plastic
a_0	1.0088	1.0088	1.0289	1.0159
a_1	1.55×10^{-2}	1.55×10^{-2}	-2.28×10^{-2}	5.78×10^{-3}
a_2	-2.82×10^{-2}	-2.82×10^{-2}	-4.91×10^{-3}	-2.42×10^{-2}
a_3	4.19×10^{-3}	4.19×10^{-3}	-1.44×10^{-3}	2.64×10^{-3}
a_4	-3.00×10^{-4}	-3.00×10^{-4}	2.84×10^{-4}	-8.98×10^{-5}
a_5	8.82×10^{-6}	8.82×10^{-6}	-1.28×10^{-5}	-1.40×10^{-8}

The parameters necessary for fitting the equation to the radial dose function data for each material are given in Table 4.

Table 4. Radial dose function non-linear fit.

polynomial coefficients	phantom material			
	water	brain	muscle	A-150 plastic
α	0.001	0.001	0.001	0.001
β	0.0167	0.0167	0.0155	0.0185
γ	1.0157	1.0157	1.0145	1.0175

E. Anisotropy Function

Select values of the anisotropy function for an AT source in water are presented (Table 5) where coordinates not available for calculation within the source were indicated by NA. For photon emitting sources such as ^{125}I and ^{103}Pd , there may be significant interaction of photons within the source encapsulation, and subsequent attenuation of these photons along the source axis, $\theta = 0^\circ$ and 180° .³⁴ For ^{252}Cf neutrons, interactions in the Pt/Ir-10% encapsulation are minimal.²¹ Thus, the impact on the anisotropy function was minimal and so it may be considered unity for practical purposes with no significant loss in accuracy for brachytherapy clinical treatment planning due to the small relative volume subtended by

Table 5. Select calculated $F_N(r, \theta)$ for ^{252}Cf AT neutron dosimetry in water.

radius (cm)	$\theta = 0^\circ$	$\theta = 5^\circ$	$\theta = 10^\circ$	$\theta = 20^\circ$	$\theta = 30^\circ$	$\theta = 45^\circ$	$\theta = 60^\circ$	$\theta = 90^\circ$
0.25	NA	NA	NA	NA	NA	1.008	1.004	1.000
0.50	NA	NA	NA	1.023	1.012	1.008	1.006	1.000
0.75	NA	NA	1.012	1.001	1.001	1.000	1.000	1.000
1.00	NA	NA	0.985	0.993	0.997	1.001	1.000	1.000
1.50	0.961	0.968	0.978	0.999	0.995	1.002	1.000	1.000
2.00	0.948	0.964	0.975	0.995	0.999	1.001	0.999	1.000
3.00	0.953	0.961	0.976	0.998	0.998	1.000	1.000	1.000
5.00	0.998	0.983	0.974	0.999	0.998	1.000	1.001	1.000
10.00	1.008	0.983	0.977	0.995	0.998	1.001	1.000	1.000

the 5 degree cone. This recommendation simplifies the calculation of ^{252}Cf fast neutron dosimetry for a variety of source and phantom types.

F. Anisotropy Factor

The anisotropy factor, $\phi(r)$, for all four ^{252}Cf source types was calculated from the ratio of dose rate integrated over a 4π solid angle and dose rate determined on the transverse axis as shown in Equation 4.

$$\phi(r) = \frac{\dot{D}(r)}{\dot{D}(r, \theta_0)} \quad (4)$$

The anisotropy factors for all four ^{252}Cf sources in muscle are presented in Figure 3. As the ORNL-made ^{252}Cf AT sources are relatively large and the encapsulation and active element do not readily attenuate the neutrons, $\phi(r)$ is typically greater than one. This is not the case for most photon emitting brachytherapy sources at distances greater than 1 cm.³⁴ The anisotropy constant for the $\mu\text{Selectron}$, VariSource , and point source was approximately unity. For the AT source, the anisotropy constant was not determined as the anisotropy factor was not constant over the radial distances examined. A generalized

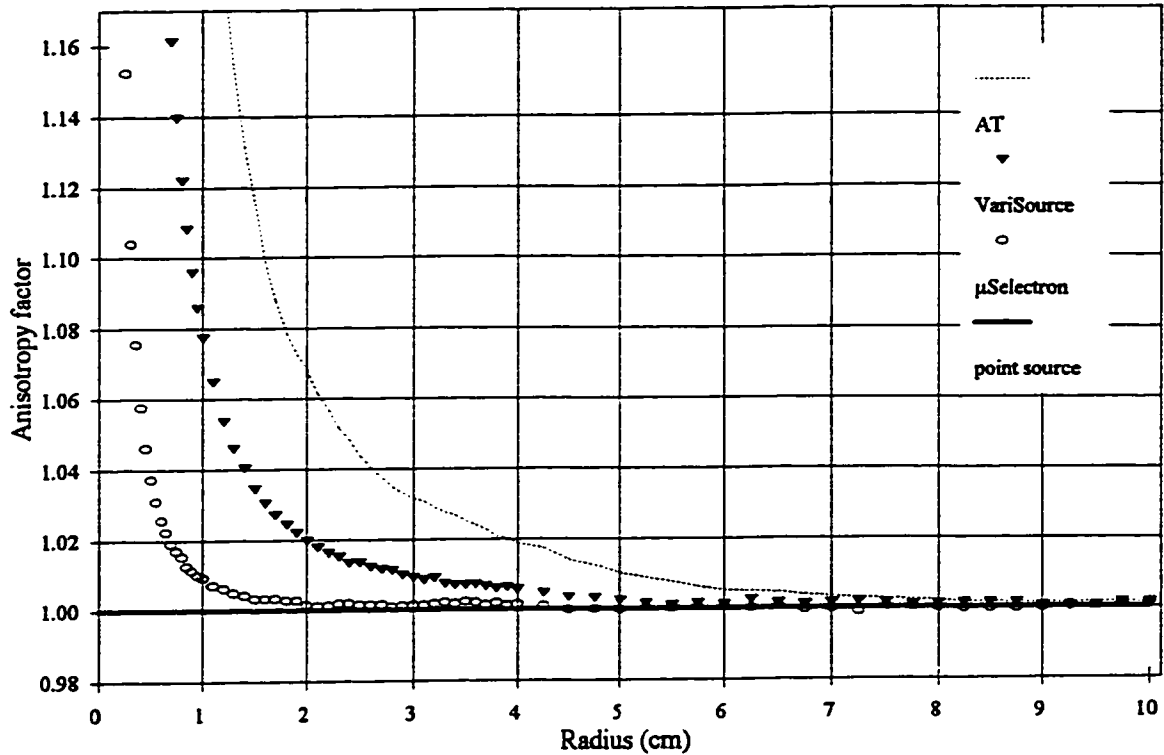


Figure 3. Anisotropy factor for AT, μ Selectron, VariSource, and point source.

equation for expressing ^{252}Cf fast neutron dosimetry in a variety of materials and any physical source configuration is presented in Equation 5 where parameters used in the equation are given in Tables 1 through 4. Equation 5 may be reduced to Equation 6 where dominance of the dose distribution by the geometry factor is made apparent.

$$\dot{D}(r, \theta) = \dot{D}(r_0, \theta_0) g(r) \left[\frac{G(r, \theta)}{G(r_0, \theta_0)} \right] \quad (5)$$

$$\dot{D}(r, \theta) = G(r, \theta) \frac{\dot{D}(r, \theta_0)}{G(r, \theta_0)} \quad (6)$$

G. Neutron Isodose Curves

For treatment planning calculations, the ^{252}Cf anisotropy function was set to unity for all materials. Consequently, the fast neutron dosimetry distribution in these four materials for any physical source configuration could be represented by an the analytical function of

Equation 6. A LINUX-based treatment planning program was written to develop isodose distributions based on TG-43 formalism.³⁴ The radius for a given dose rate, polar angle, and material was determined using bracketing techniques combined with the van Wijngaarden-Dekker-Brent root finding method.⁶⁸ Starting from the outside isodose curve, the calculated neutron dose rates in muscle are: 0.5, 1, 2, 5, 10, and 50 cGy/h- μ g for Figures 4 through 7 using the recommended parameters for the four ^{252}Cf sources.

IV. DISCUSSION

A. Comparison of ^{252}Cf Neutron Dosimetry

Currently, only ^{252}Cf AT medical sources with a 15 mm active length are available. However, experiments and calculations have been performed for other ^{252}Cf medical sources such as needles and AT sources fabricated at SRL. In this section, dosimetry results of the ORNL-made AT sources using the generalized equation (5) and TG-43

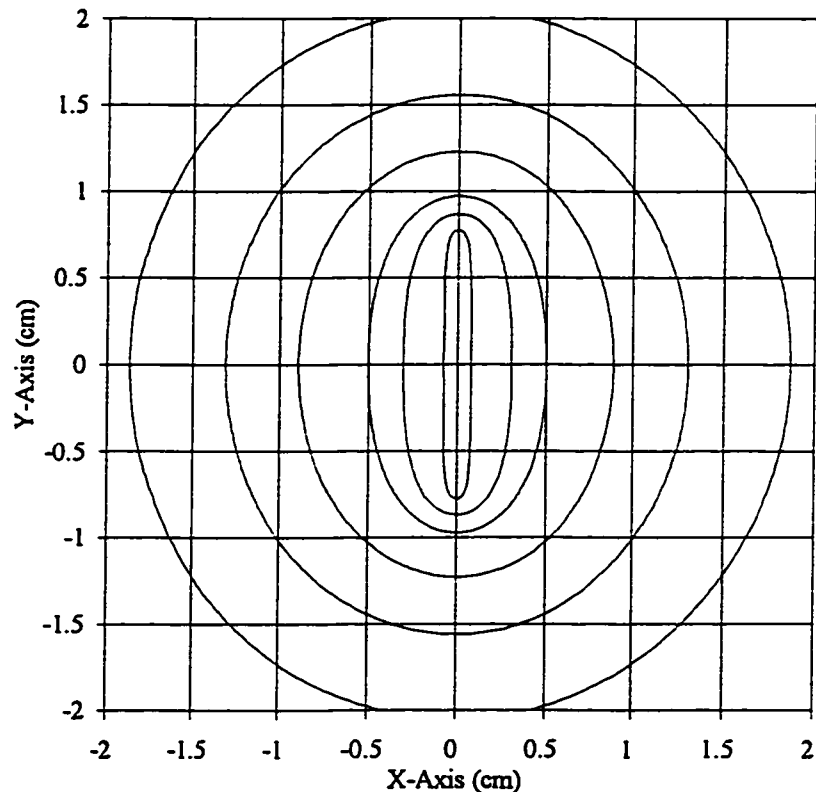


Figure 4. Neutron isodose distribution of a ^{252}Cf AT source in muscle.

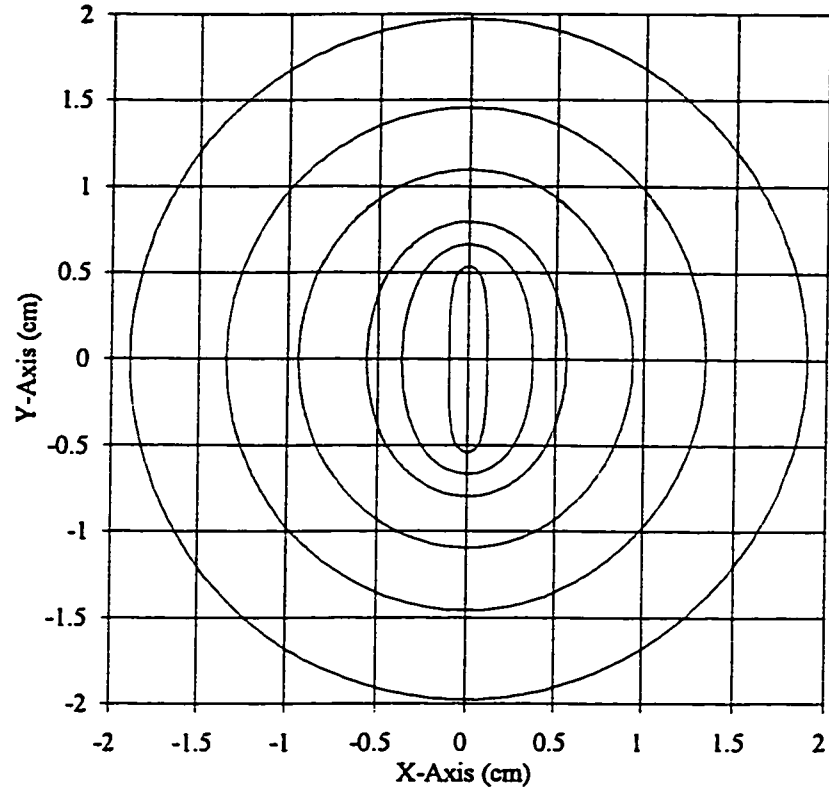


Figure 5. Neutron isodose distribution of a μ Selectron source in muscle.

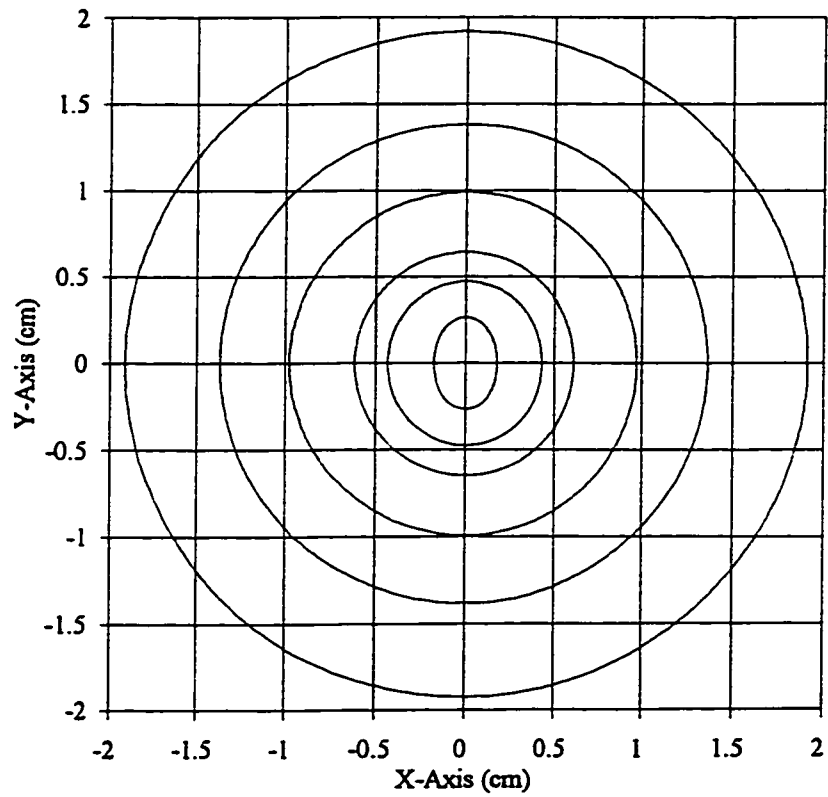


Figure 6. Neutron isodose distribution of a VariSource in muscle.

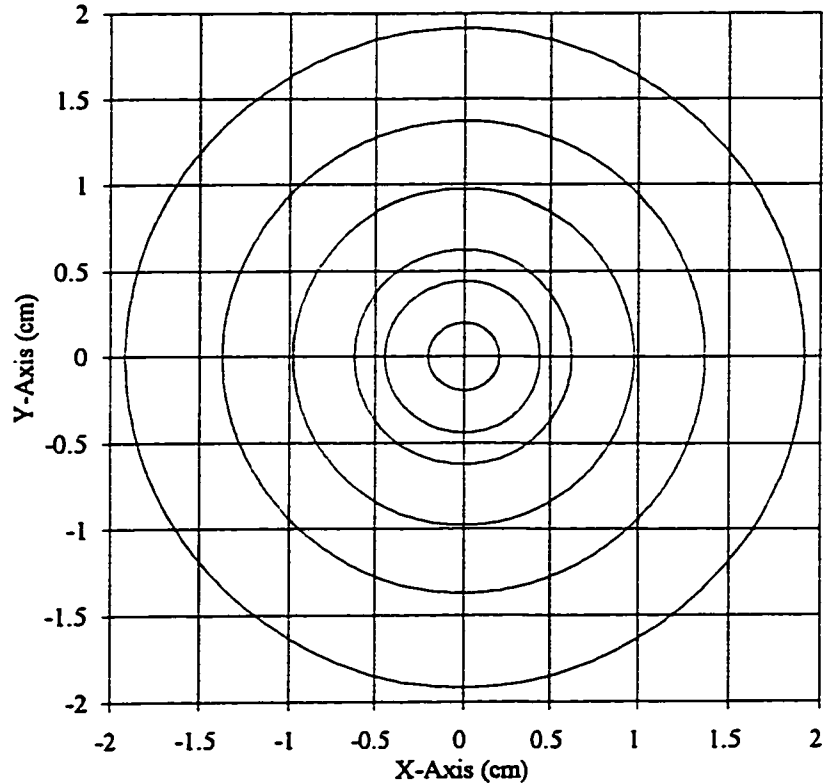


Figure 7. Neutron isodose distribution of a ^{252}Cf point source in muscle.

formalism are compared with those in the literature.

Four studies were chosen for comparison as they all employed a ^{252}Cf source of 15 mm in length. These were by Colvett *et al.*,²⁷ Krishnaswamy,²¹ Yanch and Zamenhof,⁴⁸ and Wierzbicki *et al.*⁵⁶ where results from the first study were experimentally determined while the remaining three were calculative employing Monte Carlo methods using a Watt fission neutron energy spectrum as in Equation 7 where E has units MeV.

$$N(E) = \sinh(2.926 E)^{1/2} e^{-\frac{E}{1.025}} \quad (7)$$

Krishnaswamy used a Watt fission spectrum of slightly higher energy as that presented in Equation 7, with factors of 1.136 and 2 used instead of 1.025 and 2.926, respectively. Studies conducted by both Wierzbicki *et al.* and Yanch and Zamenhof used the Watt fission parameters as presented in Equation 7.

Further differences among the studies were due to choice of phantom material. The studies by Krishnaswamy and Colvett *et al.* determined absorbed dose from neutrons in TE material incorporating 10.5% and 10.3% mass hydrogen, respectively, with total mass densities of 1.00 and 1.06 g/cm³, respectively. The more recent studies by Wierzbicki *et al.* and Yanch and Zamenhof were both performed in water with a hydrogen mass of 11.2% and mass density of 1.00 g/cm³. When accounting for differences in kerma between the water and TE studies, an 8% effect, reasonable comparisons of results from these four studies with those obtained herein may be made.⁵³ Results of Krishnaswamy and Colvett *et al.* were multiplied by 1.08 to make comparisons with the dosimetry results in water by Wierzbicki *et al.* and Yanch and Zamenhof and those results calculated in this dissertation for an AT source in water. While the ratio of kerma coefficients is a function of the neutron energy spectrum which changes with increasing distance from the source, the change in spectrum at a distance of 5 cm reduces this factor to 1.05.⁵²

Those results obtained in this chapter employed a Maxwellian spectrum, the most probable neutron energy of the Maxwellian and Watt fission spectra are 0.7 and 0.9 MeV, respectively. While no correction factor was used to account for this difference in neutron source spectrum, an estimated 15% increase between neutron dose to water is expected when comparing the kerma coefficients at 0.7 MeV (2.04×10^{-9} cGy-cm²/neutron) and 0.9 MeV (2.35×10^{-9} cGy-cm²/neutron).⁵³

Additional factors are necessary to make a reasonable comparison among these five studies. Krishnaswamy and Colvett *et al.* used a specific ²⁵²Cf neutron source strength of 2.339×10^6 n/μg-s, while that used by Wierzbicki *et al.*, Yanch and Zamenhof, and in the current study was the currently accepted value of 2.314×10^6 n/μg-s. For

comparison with others' results, the calculated results of Krishnaswamy should be reduced by 1.1%. The efforts by Colvett *et al.* used a ^{252}Cf needle which had significantly decayed since the calibration date. As a 2.58 year half-life was used instead of the currently accepted value of 2.645 years, a factor of at least 2% was necessary to reduce results of Colvett *et al.* for comparison. Anderson³³ suggests an additional factor for relating results between that of Krishnaswamy and Colvett *et al.* A reduction of 4.4% is necessary to account for differences in neutron kerma between TE plastic and tissue.

The manner in which calculation of neutron absorbed dose was conducted differs substantially within the literature. Krishnaswamy determined the neutron dose rate using a multigroup Monte Carlo approach calculating energy deposition due to elastic scattering within spheres encompassing a point source inside a 30 cm diameter TE phantom. The studies by Wierzbicki *et al.* and Yanch and Zamenhof employed identical cylindrical water phanta 60 cm in diameter and 60 cm in height. Yanch and Zamenhof calculated the neutron energy spectra and convolved this with the kerma coefficients of Caswell *et al.*⁵³ Results of Wierzbicki *et al.* and those determined herein calculated neutron kerma, which closely approximated neutron dose, in each cell using the MCNP neutron heating tally.¹

Though all studies were for SRL-made ^{252}Cf sources, the actual physical differences between the SRL-made and ORNL-made ^{252}Cf AT sources are minimal. However, studies by Krishnaswamy and Colvett *et al.* employed SRL-made ^{252}Cf needle sources which were substantially different than the AT type near the source ends. Also, the sampling space of the calculative studies varied significantly. Krishnaswamy determined the neutron dose rate for a point source using spherical bins spaced 0.5 cm apart. While these bin sizes posed no concern due to volume averaging at distances of

greater than 3 cm, they clearly under-estimate the dose obtained at a fixed radius at the center of the bin. Anderson³³ determined a formula for estimating the errors, and determined that neutron dosimetry results of Krishnaswamy at 0.5 and 1.0 cm should be increased by 33.3 and 3.7%, respectively. Wierzbicki *et al.* and Yanch and Zamenhof both employed near-source bins 0.2 cm apart which had an estimated 1.003 volume averaging effect at 1.0 cm and maximum effect of 1.017 for bins of 0.34 to 0.54 cm. As previously noted, bins used herein were relatively small, and for the closest calculated distance of 0.150 cm, the spheres were spaced 0.010 cm apart, e.g. 0.145 and 0.155 cm, for a volume averaging effect of 1.0004% as determined using equations by Anderson.²⁶

In summary, the multiplicative factors used to relate the results of Colvett *et al.*²⁷ and Krishnaswamy²¹ to those of Yanch and Zamenhof,⁴⁸ Wierzbicki *et al.*,⁵⁶ and those determined herein are 1.012 and 1.108 respectively. Examination of the reference dose rate, that at r_0 and θ_0 , by the various studies in water is presented in Table 6 with the aforementioned corrections incorporated. From Table 6, the variation among the studies was 7.0%. As all these studies employed the same active source length of 15.0 mm, the geometry factor remained constant and a direct comparison of the radial dose functions is accomplished in Figure 8 without incorporating additional factors.

Table 6. Comparison of reference neutron dose rates at r_0 and θ_0 .

reference	reference neutron dose rate (cGy/h- μ g) with factors included for Krishnaswamy and Colvett et al.
Krishnaswamy	2.087
Colvett et al.	2.074
Yanch and Zamenhof	1.900
Wierzbicki et al.	1.880
This study	1.772

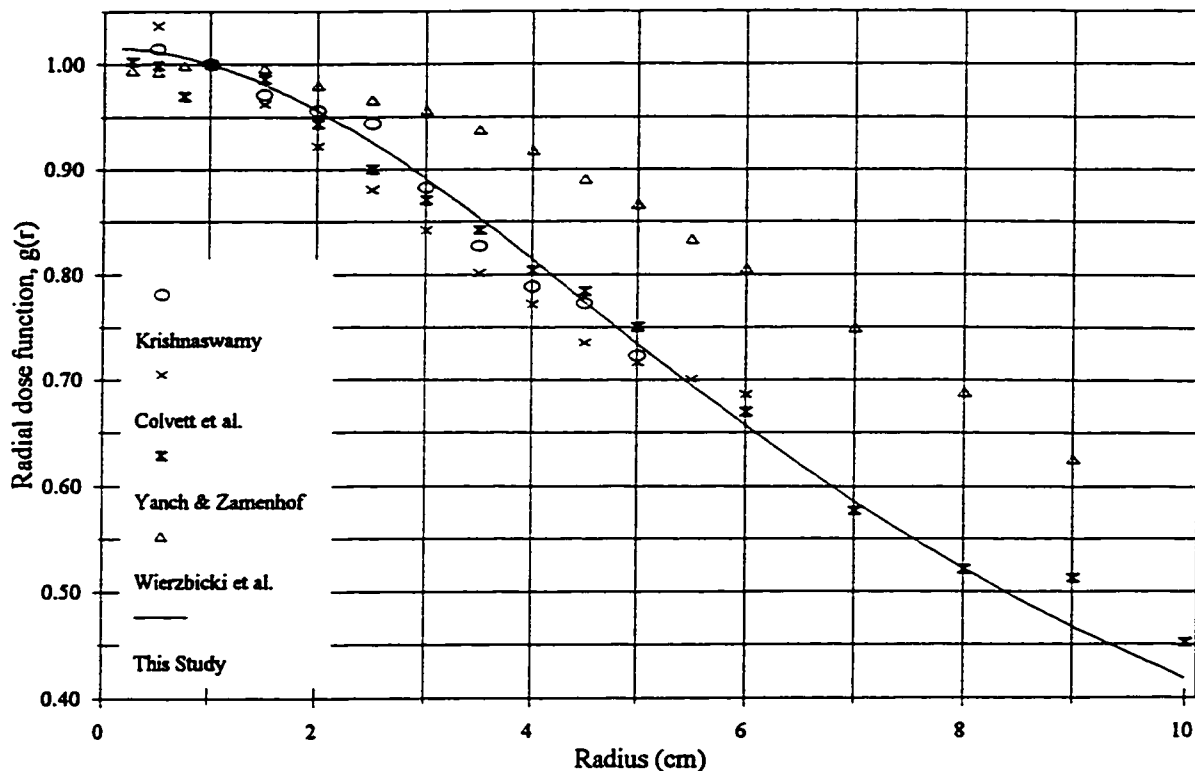


Figure 8. Comparison of neutron radial dose functions for ^{252}Cf sources.

V. CONCLUSIONS

The neutron dosimetry of four ^{252}Cf sources, AT, $\mu\text{Selectron}$, VariSource, and a point source, have been calculated using Monte Carlo methods in water, brain, muscle, and A-150 plastic. From these findings and application of TG-43 dosimetry formalism, a general equation describing fast neutron dosimetry has been formulated. This was possible as the active source and encapsulating materials did not significantly perturb the fast neutron dose distribution. Comparison of these ^{252}Cf neutron dosimetry results with those in the literature revealed significant differences. These differences in ^{252}Cf neutron dose distributions were attributed to ^{252}Cf source geometry, outdated nuclear data, choice of neutron energy spectrum, and dosimetry phantom material.

CHAPTER 4

CALCULATION AND MEASUREMENT OF THERMAL NEUTRONS RESULTING FROM MODERATION OF ^{252}Cf NEUTRONS

I. INTRODUCTION

Monte Carlo methods using the MCNP code were used in the calculation of the moderated ^{252}Cf neutron energy spectrum in a variety of materials and for a selection of distances from the ^{252}Cf source.¹ Additionally, thermoluminescent dosimeters (TLDs) and activated gold foils were used to obtain an experimental measure of the moderated ^{252}Cf thermal neutron yield. Relative measurements using TLDs obtained the overall shape of the thermal neutron distribution as a function of depth while gold foils were used to obtain an absolute measure of the moderated ^{252}Cf thermal neutron yield. Comparisons of experimental results were made with those calculated using MCNP and also with results presented in the literature.

II. MATERIALS AND METHODS

A. Calculative Techniques

Using MCNP, a distributed computing environment³⁵⁻³⁷ was used for swift computation of the neutron energy spectrum and calculation of nuclear capture reactions necessary to model the experimental setups described below. The calculative model employed a geometrical setup divided with surfaces into cells over which the calculated results were integrated. Calculations were performed for a ^{252}Cf point source and AT source.

The Monte Carlo calculations used in this study were divided into three sets. The first set of calculations employed a point source centrally positioned within a 15 cm diameter spherical phantom of a given composition. Four materials were studied. The

first was light water with 0.015% atomic abundance ^2H relative to ^1H , and a mass density of 0.998 g/cm^3 . Brain and muscle materials, with compositions described in ICRU 44,³⁸ were studied as these are clinical media in which ^{252}Cf neutron brachytherapy may be performed. A-150 plastic was also studied as it is a useful neutron dosimetry material for experimental measurements.^{32,38} To permit accurate thermal neutron transport, the MCNP solid-state $S(\alpha,\beta)$ neutron scattering library (lwtr.01t) was used to model low energy neutron scattering by hydrogen.³⁷ The entire volume was divided into radial bins using spheres of varying radii, from 1 mm to 7.5 cm, to permit spatial resolution. The energy flux at each radii was divided into energy bins for calculation of the moderated neutron energy spectra. Energy was sampled from 10 meV to 15.85 MeV with 10 energy bins per decade to permit regular bin spacing when examining results on a log-log plot.

The second set of Monte Carlo calculations was performed to confirm the experimental results of gold foil activation. The geometrical setup of the Monte Carlo model was made to match that of the experimental setup. A 120 liter, thin walled plastic cylindrical storage drum filled with water was modeled with a diameter and height of 48 and 63 cm, respectively. Two ^{252}Cf AT sources and two gold foils of diameter 3.21 mm (0.126"), nominal thickness of 0.001", and a density of $19,300 \text{ kg/m}^3$ were arranged on a plane 20 cm below the upper surface. The entire AT geometry (capsule welds, internal air, eyelet) of each source was modeled, as were their relative source strengths, 50.2% and 49.8%, of the total source strength. The AT sources were placed 6.0 cm apart and oriented with their long-axis parallel to that of the cylindrical water phantom. Two separate gold foils were placed at a distance of 5.0 cm from each AT source and 8.0 cm from each other. Thus, the center of the computational geometry, an AT source, and a

gold foil subtended a Pythagorean triangle of sides 3, 4, and 5 cm in length. One gold foil was placed in a closely fitting cadmium box with walls 1 mm thick and density of 8,650 kg/m³, and secured to another silk thread for positioning. The second gold foil was suspended at its position in the water phantom with a silk thread and secured with tape, but was not enclosed in a cadmium box. In no cases were the foils in contact with the adhesive portion of the tape used to facilitate foil positioning. A rigid styrofoam plate placed over the open water phantom supported the silk threads and minimized evaporation. The silk threads used to suspend the AT sources and gold foils within the water phantom were not modeled. The hydrogen lwtr.01t solid-state neutron scattering library was used with a water room temperature density of 1,000 kg/m³. Deuterium was present in the water at a concentration of 0.01% with ¹H, ¹⁶O, and ¹⁷O accounting for the remaining 66.66, 33.32, and 0.01% atomic concentration, respectively.

The third set of Monte Carlo calculations used the same water phantom and AT source setup as the second set of calculations. However, the gold foils and cadmium box were not present and were replaced with a water tally cell used to precisely determine the moderated neutron energy spectra over a range of 0.1 meV to 15.85 MeV with 50 energy bins per decade. All calculations herein were for transport of 10⁷ neutrons.

B. Experimental Techniques

Absolute Measurements with Gold Foils

Using the geometry described above, the American Society for Testing and Materials (ASTM) protocol E 262-86e, *Standard Test Method for Determining Thermal Neutron Reaction and Fluence Rates by Radioactivation Techniques*,⁶⁹ was strictly adhered to for the irradiation of the gold foils and subsequent measurements. To reach transient

equilibrium with the decaying ^{252}Cf AT sources, the gold foils were irradiated for a time, 66.64 days, much longer than the half-life of ^{198}Au , 2.696 days. The total source strength of the two AT ^{252}Cf sources at the time of experiment termination was 12.95 μg as calculated from the source calibration provided by ORNL. Following irradiation, the mass of each foil was determined at ORNL with an accuracy of $\pm 10 \mu\text{g}$; the masses of the plain gold foil and cadmium covered gold foil were 4.295 and 4.455 mg, respectively. Using a gold density of 19,300 kg/m^3 and a foil thicknesses of 0.028 mm, the corresponding foil diameters were 3.18 and 3.24 mm for an average diameter of 3.21 mm.

The energy spectra of the activated foils were measured with a coaxial, high purity germanium detector (Canberra, model GR1318 HPGe) operated at -3500 volts. A spectroscopy amplifier (Canberra, model 2022) was used with a shaping time of 4 μs . A Nuclear Data model ND 65 multichannel analyzer (MCA), with energy signals digitized into 4096 channels, was calibrated using ^{60}Co and ^{137}Cs test sources. In the measurement geometry, the efficiency of the HPGe detector was calibrated using a calibrated Amersham QCD.1 mixed radionuclide gamma-ray reference source. Of the many isotopes present in the circular QCD.1 calibration source, ^{113}Sn and ^{85}Sr were specifically examined as their principal photon energies, 391.7 and 514.0 keV, respectively, bounded the principal photon energy from ^{198}Au , 411.8 keV.⁷⁰ During measurements, the mixed radionuclide source and gold foils were separately placed at a reproducible distance from the HPGe while other sources were removed from the room to permit a low background.

Determination of Thermal Neutron Fluence Rate from Foil Activation

Measurements

The American Society for Testing Materials (ASTM) has published a protocol (ASTM E

262-86e) for the determination of thermal neutron fluence.⁶⁹ According to this protocol, the thermal neutron fluence rate, ϕ_{th} , is related to the measured gold saturation activity and other experimental parameters by:

$$\phi_{th} = \frac{1}{G_{th} g \sigma_0} [A_s - A_{s,Cd} (1 + \frac{g \sigma_0 f_0}{G_{res} I_0} + \frac{\sigma_0 w'}{G_{res} I_0})] \quad (1)$$

where:

ϕ_{th}	= 2200 m/s equivalent thermal fluence rate	[n/cm ² -s]
σ_0	= 2200 m/s total capture cross-section	[barns]
I_0	= gold resonance integral	[barns]
G_{res}	= gold resonance self-shielding factor at 4.9 eV	[dimensionless]
G_{th}	= thermal self-shielding factor for gold	[dimensionless]
A_s	= saturation activity of a plain gold foil	[Bq/atom]
$A_{s,Cd}$	= saturation activity of a cadmium covered gold foil	[Bq/atom]
g	= correction factor for non-1/v thermal cross-section	[dimensionless]
w'	= departure from 1/v cross-section from 0.127 to 0.55 eV	[dimensionless]
f_0	= epithermal neutron activation factor, 0.127 to 0.55 eV	[dimensionless]

While many parameters were dependent on the experimental setup, derivation of some parameters relied only on the use of 0.028 mm thick gold foils and a 1 mm thick cadmium box.⁶⁹ These intrinsic experimental parameters are given in Table 1.

Table 1. Intrinsic experimental parameters according to ASTM protocol.

experimental parameter	value
σ_0	98.8 barns
I_0	1559 barns
G_{res}	0.35
G_{th}	1.00
g	1.0052
w'	0.0600
f_0	0.468

The saturation activities were determined experimentally with and without the cadmium shield and are presented later.

Relative Measurements with TLDs

An entirely separate experiment was performed which employed two sets of LiF TLD cubes, types 600 and 700, with varying $^6\text{Li}/\text{Li}$ concentrations, 95.62% and 0.0007% respectively, so as to exploit the $^6\text{Li}(n,\alpha)^3\text{H}$ thermal neutron reaction. As there was no thermal neutron source available for TLD calibration, the relative photon sensitivity of each TLD was determined through calibration using a ^{60}Co photon source for doses of approximately 100 cGy. The 1 mm^3 TLD cubes were set in a $5 \times 30 \times 30\text{ cm}^3$ polystyrene jig at a depth of 5 mm for the calibration procedure. After a delay of at least 8 hours, a time-temperature profile consisting of a 10 second preheat at 100°C and a 50 second ramp from 100°C to 350°C was used to generate the thermoluminescent signal; for readout, a Harshaw 3500 device was used. TLDs were annealed in air for 2 hours at 100°C and 1 hour at 400°C . Four hours following annealing, the TLDs were available for further irradiations. An A-150 plastic jig contained the TLD during irradiation with a single ^{252}Cf AT source. As all experiments were performed within eleven days, there was no significant decay of the $7.4\text{ }\mu\text{g}$ ^{252}Cf source. Sets of TLD 600 and 700 were irradiated with ^{252}Cf for time periods of 5, 10, and 50 hours. A section of the A-150 plastic phantom used for the irradiations is shown in Figure 1 where the single AT source was surrounded by TLDs at various positions numbered 1 through 28. The AT source was offset at a depth of 6.5 mm from the TLD plane to minimize shielding among the TLDs.

III. RESULTS

A. Absolute Measurements of the ^{252}Cf Thermal Neutron Fluence Using Gold Foils

Determination of Germanium Detector Efficiency

Before results of the gold foil measurements could be examined, determination of the HPGe detector efficiency in the measurement geometry was necessary. The QCD.1

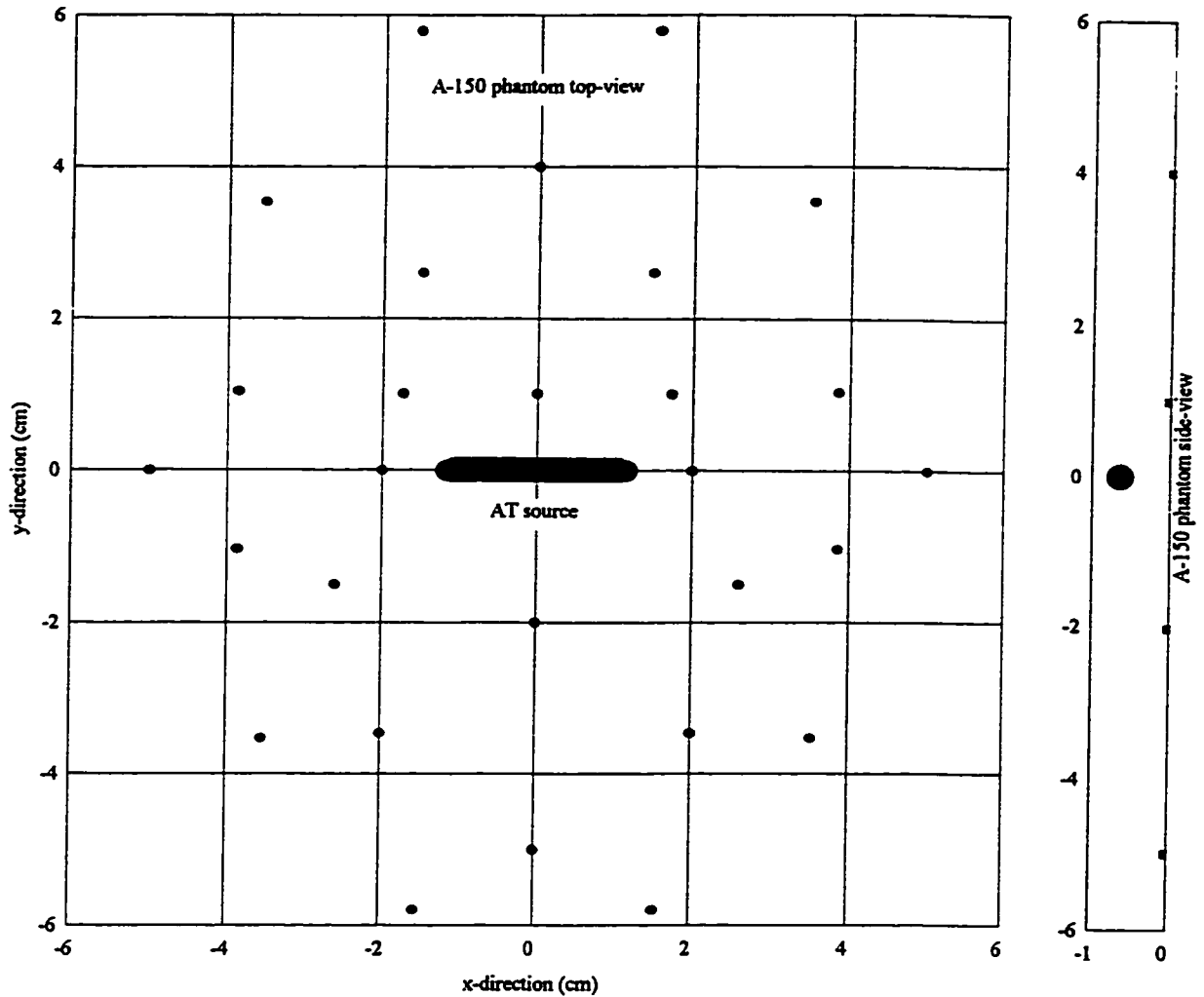


Figure 1. A-150 phantom for TLD irradiations.

calibration source was placed at a fixed distance of 4.4 mm from the HPGe detector beryllium window face. Calibration measurements of 391.7 keV ^{113}Sn and 514.0 keV ^{85}Sr photons were performed twice for 20.00 and 33.05 hours. The number of counts in 391.7 and 514.0 keV energy bins for the first and second set of measurements were 159,053 and 260,607, 42,828 and 68,239, respectively, upon subtraction of the measured background. The statistics associated with these number of photopeak counts ranged from 0.2 to 0.5%. The system sensitivity to 391.7 keV ^{113}Sn and 514.0 keV ^{85}Sr photons was 6.20 and 4.91%, respectively; system sensitivity to 411.8 keV ^{198}Au photons was 5.94% which was

determined using a log-log fit between the calibration points.

Measurement of ^{198}Au Production

From these measurements, and allowing for the exponential decay of ^{198}Au with a half-life of 2.696 days, the equilibrium number of photopeak counts at saturation for each foil was determined to be 19.06 and 2.609 counts per second (cps) for the plain gold and cadmium covered gold foil, respectively. The ratio of these foil count rates was 7.306. For calculation of ^{198}Au production, a 411.8 keV photon yield of 95.5% and the efficiency of 5.94% was employed. The ^{198}Au activities in the plain gold and cadmium covered gold foil were 336.0 and 46.0 Bq, respectively. To determine the 2200 m/s thermal neutron fluence rate, ϕ_{th} , from Equation 1, the above activities need to be expressed per unit atom. Here, A_x and $A_{x,Cd}$ are 2.559×10^{-17} and 3.377×10^{-18} Bq/atom, respectively, when dividing by the total atoms per foil, 1.313×10^{19} and 1.362×10^{19} , based on a gold mass density of $19,300 \text{ kg/m}^3$, Avogadro's constant, and the individual foil masses.⁶⁹ From Equation 1 at a distance of 5.0 cm, ϕ_{th} was $2.204 \times 10^5 \text{ n/cm}^2\text{-s}$ for $12.95 \text{ }\mu\text{g}$ of ^{252}Cf which is equivalent to $1.702 \times 10^4 \text{ n/cm}^2\text{-s-}\mu\text{g}$.

B. Relative Measurements with TLDs

TLD Linearity

As some TLDs of a given type, 600 or 700, were placed in the same A-150 jig position for irradiations of varying durations, the linearity of TLD response as a function of ^{252}Cf dose was available. Sixteen TLD-600s shared common A-150 positions for ^{252}Cf irradiations of 5 and 10 hours. The 10 hour irradiation gave a response 2.6% lower than that expected from the shorter (5 hour) measurement. ^{252}Cf irradiations lasted 5 and 50 hours for the 14 TLD-700s which shared common A-150 irradiation positions; the 50 hour irradiation had

a response 1.5% higher than the shorter (5 hour) irradiation.

²⁵²Cf Irradiation Results

The TLD-600s were more sensitive to thermal neutrons than the TLD-700s due to the 10^5 factor increase in ^6Li due to enrichment. However, due to the presence of photons and fast neutrons in addition to thermal neutrons, the TLD-600 response may not be fully attributed to thermal neutrons. Consequently, the TLD-700 response at a given position was subtracted from the TLD-600 response at the same position to determine the net TLD response which may be reasonably attributed to thermal neutrons. The photon and fast neutron response of both TLD types were comparable and much smaller than thermal neutron response.^{71,72} For 6 positions about the ²⁵²Cf source center, the average net TLD response was found. Results normalized to the 6.04 cm response are given in Table 2.

Table 2. Measured net TLD response for various radii from a ²⁵²Cf AT source.

A-150 position	radius (cm)	TLD-600 response exp. #1 (nC) exp. #2 (nC)	TLD-700 response exp. #1 (nC) exp. #3 (nC)	avg. net response (nC/h- $\mu\text{g}^{252}\text{Cf}$)	TLD net response normalized to 6.04 cm
6, 12 17, 23	6.04	(731.7, 702.9) (1539, 1473)	(8.000, 8.243) (55.41)	19.59	1.000
13	5.04	(973.2) (1941)	(-) (74.02)	25.96	1.325
16	4.05	(-) (2553)	(12.95) (55.22)	34.11	1.741
7, 18	4.05	(1197) (2422, 2893)	(13.72) (105.7, 108.6)	34.27	1.749
14	2.10	(1628) (3501)	(-) (306.1)	44.65	2.279
15	1.19	(-) (3843)	(87.27) (866.3)	49.38	2.520

Note: A dash (-) denotes that TLDs were not placed at that position in the A-150 jig

C. Monte Carlo Calculation of Thermal Neutron Fluence Experimental Setup

The experimental setup was modeled using MCNP, and the equilibrium ¹⁹⁸Au production for the plain gold and cadmium covered foils was determined using a Maxwellian ²⁵²Cf neutron energy spectrum and a neutron yield of 2.314×10^6 n/s- μg .⁵⁵ The calculated ¹⁹⁸Au

activities in the plain gold and cadmium covered gold foils were 314.6 ± 3.5 and 43.36 ± 3.3 Bq when using $12.95 \mu\text{g}$ of ^{252}Cf and foil masses of 4.295 and 4.455 mg, respectively. The ratio of these activities was 7.256 which was 0.7% less than that (7.306) determined experimentally. A plot of the total ^{198}Au relative yield segmented into energy bins is presented in Figure 2. The ^{198}Au relative yields of the plain gold and cadmium covered foils are shown, as well as the calculated $^{197}\text{Au}(n,\gamma)^{198}\text{Au}$ and $_{\text{nat}}\text{Cd}(n,\text{abs})$ cross-sections (XS). The ^{198}Au yields were identical between the plain and cadmium covered gold foils, except at energies beneath 1 eV. Differences between the plain and cadmium covered gold foil ^{198}Au yields were caused by cadmium absorption of neutrons with energies beneath approximately 1 eV. Figure 3 presents a high-resolution plot of the calculated neutron energy spectrum at a distance of 5.0 cm without gold present. It is evident that a significant fluence of thermal neutrons is present. On calculating the thermal neutron

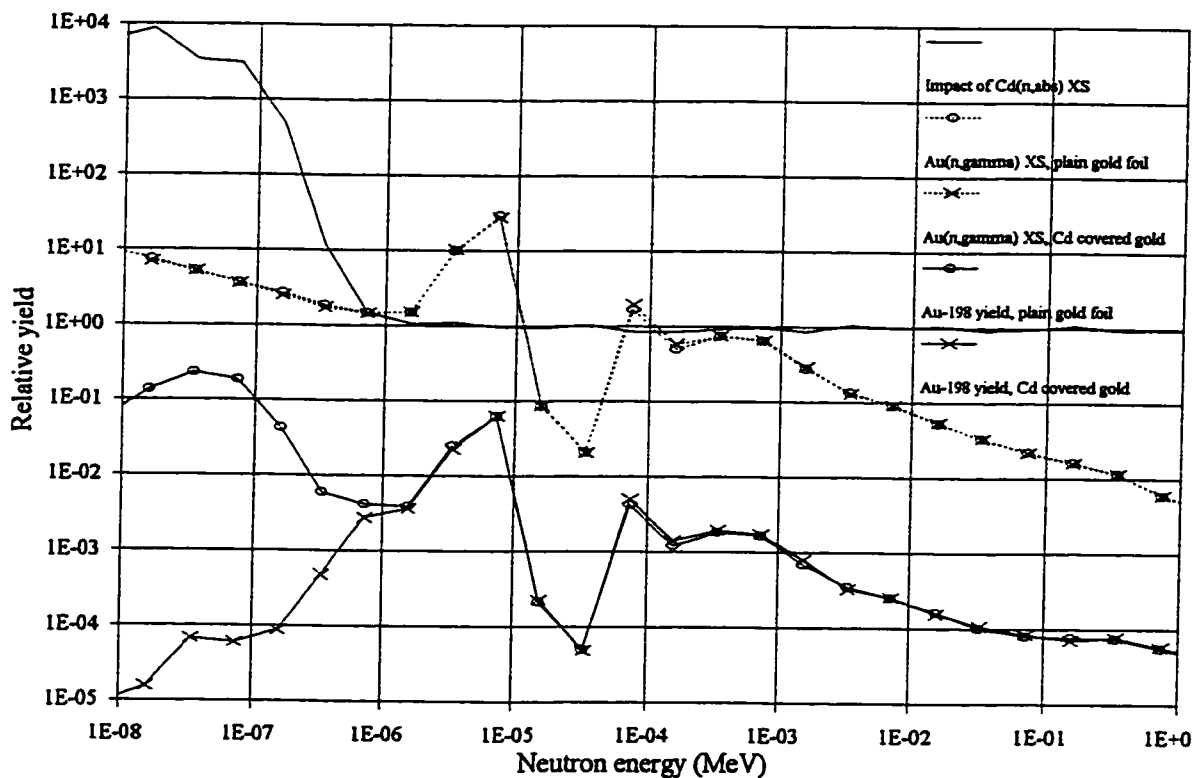


Figure 2. ^{198}Au relative yields, $\text{Au}(n,\gamma)^{198}\text{Au}$, and $\text{Cd}(n,\text{abs})$ cross-sections.

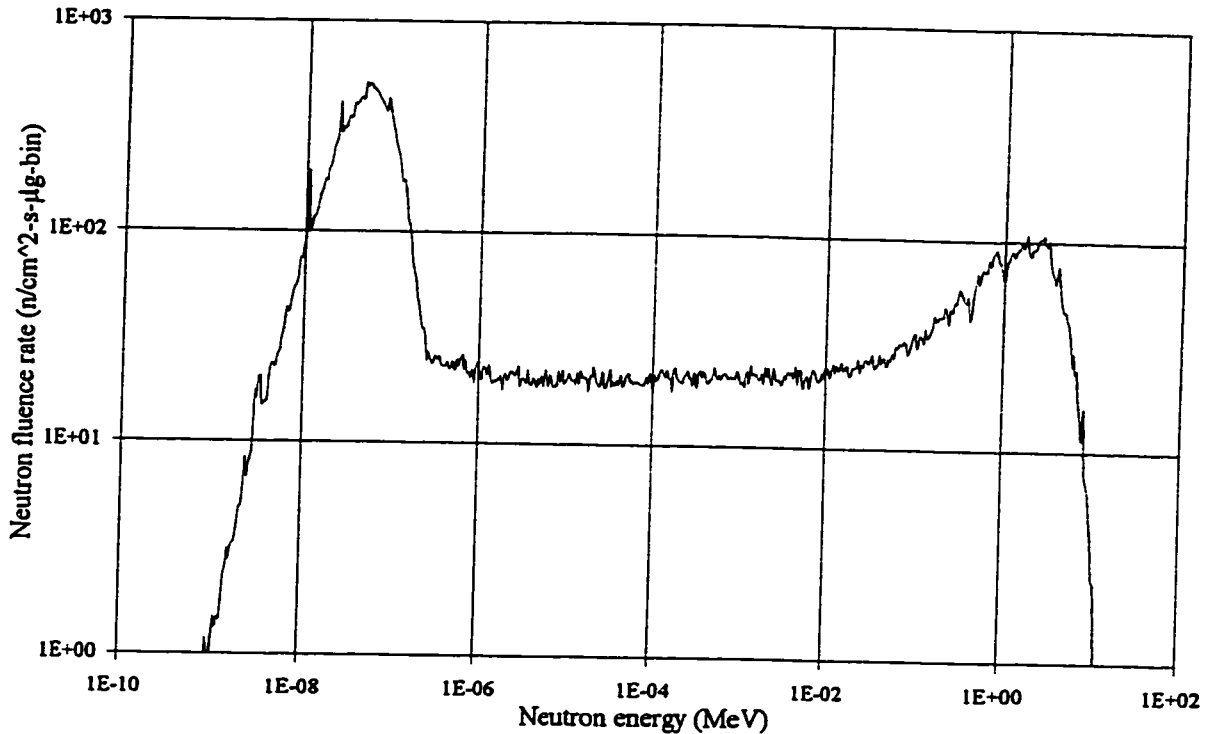


Figure 3. Neutron energy spectrum in water at a radius of 5.0 cm.

fluence rate at 5.0 cm in water from the flux integral beneath 0.55 eV,⁶⁹ a value of 1.998×10^4 n/cm²-s-μg was obtained.

D. Monte Carlo Calculation of Neutron Energy Spectra for a Variety of Media

Results of neutron energy spectra as a function of radii for water in a 15 cm diameter spherical phantom are given in Figure 4.⁵² It is evident from the 1 and 3 cm curves that the proportion of fast neutrons fall off rapidly (~ factor of 10) while the thermalized neutron fluence does not significantly change (~ factor of 10%) within radii of 3 cm.

These trends were also evident for the other three materials studied, brain, muscle, and A-150 plastic. For comparison, the neutron spectra at a radius of 5 cm is given in Figure 5 for all four materials. Due to the higher hydrogen mass density of A-150 plastic (114 kg/m³) as compared to brain (111 kg/m³), water (112 kg/m³), or muscle (107 kg/m³),

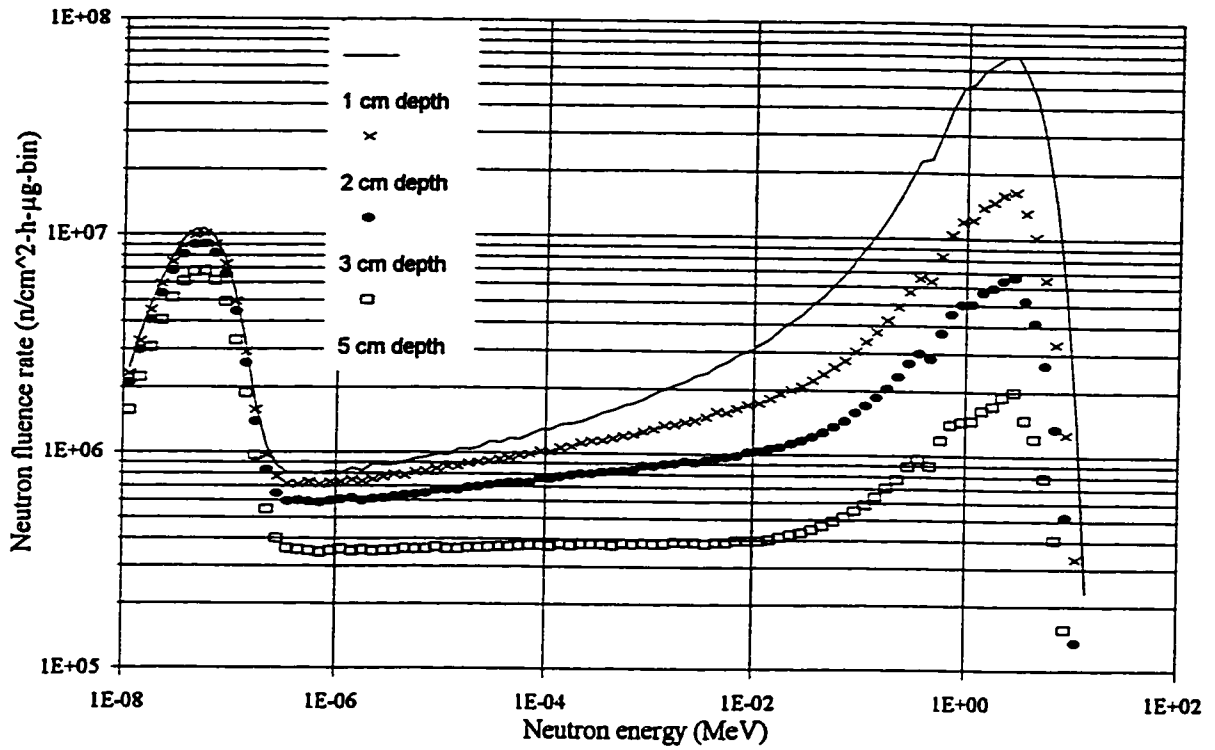


Figure 4. Neutron energy spectra in water for various radii.

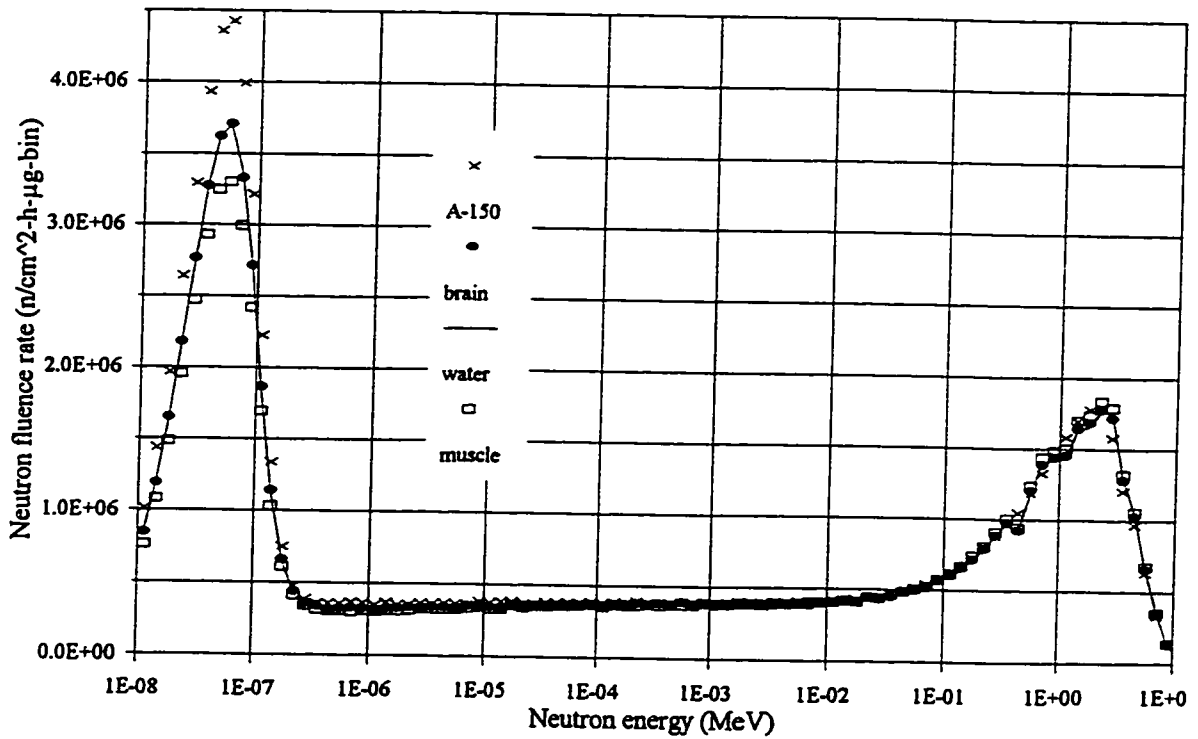


Figure 5. Neutron energy spectra of A-150 plastic, brain, water, and muscle.

there was consequently more neutron moderation and production of thermalized neutrons in A-150 than the other 3 materials. If one assumes an approximate $1/v$ cross-section dependence for the ${}^6\text{Li}(n,\alpha){}^3\text{H}$ reaction as measured using TLD type 600, then the TLD relative responses may be compared with Monte Carlo calculations of the neutron energy spectrum in A-150. The integral of the calculated A-150 neutron energy spectrum convolved with a theoretical $1/v$ cross-section (n_{th}) is presented in Table 3 at various radii.

Table 3. Comparison of MCNP relative thermal neutron fluence with net TLD results.

radius (cm)	MCNP n_{th} (normalized to 6.04 cm)	net TLD response (normalized to 6.04 cm)	MCNP / TLD ratio
6.04	1.000 \pm 0.003	1.000 \pm 0.040	1.000 \pm 0.040
5.04	1.324 \pm 0.004	1.325 \pm 0.053	0.999 \pm 0.040
5.00	1.355 \pm 0.004	---	---
4.05	1.692 \pm 0.005	1.745 \pm 0.070	0.970 \pm 0.040
2.10	2.277 \pm 0.007	2.279 \pm 0.091	0.999 \pm 0.040
2.00	2.310 \pm 0.007	---	---
1.19	2.486 \pm 0.007	2.520 \pm 0.101	0.987 \pm 0.040
1.00	2.513 \pm 0.008	---	---

IV. DISCUSSION

A. Error Analysis

Monte Carlo Calculations

The primary limitation of the Monte Carlo methodology here was the number of particles transported. Relative errors of $\pm 7.7\%$ and $\pm 1.1\%$ resulted for ${}^{198}\text{Au}$ production in the cadmium covered and plain gold foil volumes, respectively, following transport of 10^7 neutrons in the input geometry used to simulate the gold foil experimental setup.

Accuracy of the Maxwellian model for the ${}^{252}\text{Cf}$ neutron energy spectrum was estimated at $\pm 5\%$. Errors introduced through inaccurate Monte Carlo data libraries and incorrect

transport physics were ignored. Therefore, the total error in the gold foil calculations was approximately $\pm 9\%$. For the calculations of thermal neutron fluence used in the TLD study, Table 3, a relative error of $\pm 0.03\%$ was obtained after transport of 10^7 neutrons.

Gold Foil Measurements

Measurements may be divided into three sections for error analysis. First, the experimental setup employed gold foils, a cadmium box, two AT sources, a water phantom, and their relative positions. Dimensions of the water phantom were accurate to ± 2 mm which should not significantly influence results herein. Use of a rigid styrofoam jig and silk threads kept positioning errors within ± 0.5 mm, and due to the gradual fall-off of the thermal neutron fluence as a function of distance, the errors in the experimental setup were approximately $\pm 1\%$. Errors in the measurement setup may have been due to the stated calibration accuracy of the QCD.1 source ($\pm 4.5\%$). Use of a rigid jig to support both the QCD.1 source and both gold foils at identical positions minimized errors resulting from reproducibility of position. Errors were also incurred due to implementation of the ASTM methodology. Measurement of the cadmium box wall thickness was performed with multiple micrometers, and was accurate to ± 0.05 mm. AT source strengths were accurate to within $\pm 3\%$ as determined by ORNL. The masses of the gold foils were accurate to $\pm 0.2\%$ due to measurement at ORNL. The thickness of the gold foils was determined from the foil masses, density of gold, and foil diameter; the estimated accuracy here was $\pm 1\%$ which would not significantly perturb thickness-sensitive factors like G_{th} and G_{res} .⁶⁹ ϕ_{th} was dependent on parameters such as G_{th} , G_{res} , A_p , and $A_{x,Cd}$. In summary, the total systematic error associated with the gold foil measurements was roughly $\pm 6\%$. As the relative error in Monte Carlo calculations was \pm

9%, the total uncertainty in the ratios was approximately $\pm 11\%$ (1σ).

TLD Measurements

Variation of individual TLD response was approximately 20% as determined by uniform irradiation to 100 cGy using a ^{60}Co photon source. Consequently, individual TLD sensitivities were determined to correlate the results. The sensitivities for individual TLDs varied by approximately $\pm 4\%$ throughout the experiment. In determination of the relative thermal neutron fluence at the various positions, responses between TLD-700s were subtracted from TLD-600s to obtain the net response. Consequently, the errors for each TLD pair went as the root of the sum of the errors squared, or was approximately $\pm 5.66\%$ for each TLD pair. On average, there were 2 TLD pairs per position which brought the average error at each position down to $\pm 4\%$ (these errors are included in Table 3). Precision machining of the A-150 jig kept AT and TLD positioning errors at less than 0.1 mm, and relative measurements enabled no induction of errors through ^{252}Cf AT source strength uncertainty. Furthermore, when incorporating uncertainties introduced by Monte Carlo calculations, $\pm 0.3\%$, the total uncertainties were $\pm 4\%$ when comparing ratios of calculated to experimentally determined thermal neutron fluence.

B. Comparison of Calculated and Experimental Thermal Neutron Fluences

Using gold foils and ASTM protocol,⁶⁹ the absolute thermal neutron fluence at a distance of 5.0 cm from ^{252}Cf AT sources was measured. The behavior of the thermal neutron fluence as a function of distance was determined using TLDs in a relative manner. These experimental results are compared with those calculated using MCNP. From Figure 5, it is evident that the relative behavior of the thermal neutron fluence of water and A-150 plastic differ. Consequently, the results obtained using TLDs in A-150 and gold foils in

water must be analyzed separately.

C. Comparison of MCNP and TLD Results

It is evident from the data in Table 3 that there was good agreement between the calculated and experimental results considering the statistical errors involved with the few, 2 on average, TLDs at each point from Table 2. Both relative thermal neutron fluences were normalized to the 6.04 cm values as the proportion of thermal neutrons was greatest.

D. Comparison of MCNP and Gold Foil Results

Using MCNP, the following parameters were calculated: ratio of ^{198}Au activities for plain and cadmium covered gold foils, number of ^{198}Au atoms per $\mu\text{g } ^{252}\text{Cf}$ for plain and cadmium covered gold foils, and the thermal neutron fluence rate at 5.0 cm. The calculated and measured ratios of ^{198}Au activities were 7.256 and 7.306, respectively, yielding a 0.7% agreement. The calculated and experimentally determined ^{198}Au activity (Bq) for 12.95 $\mu\text{g } ^{252}\text{Cf}$ for the plain gold foil was 314.6 and 336.0, respectively, providing a 6.8% agreement. Calculated and experimentally determined ^{198}Au activity with 12.95 $\mu\text{g } ^{252}\text{Cf}$ for the cadmium covered gold foil was 43.36 and 46.0 Bq, respectively, generating a 6.1% agreement. Finally, thermal neutron fluence rates determined with MCNP and experimentally were $1.998 \times 10^4 \pm 1800$ and $1.702 \times 10^4 \pm 1020$ $\text{n/cm}^2\text{-s-}\mu\text{g}$, respectively, producing an agreement of 15% which was just outside the estimated uncertainties.

E. Comparison of Thermal Neutron Fluence Results with Others

Two separate experimental studies were chosen for comparison as they both employed ^{252}Cf sources and gold foils. The first study by Wierzbicki *et al.*⁷³ employed four 19 $\mu\text{g } ^{252}\text{Cf}$ AT source arranged in a cylindrical array 6 cm in diameter within a cylindrical water volume of 20 cm height and 15 cm diameter. A single gold foil was placed at the phantom

center, with 4 additional foils at radii of from 1 to 4 cm. Foil readout was performed at ORNL using a HPGe detector and an MCA. The irradiation time was not stated, nor was there any mention of use of a cadmium shielding foil in this article. However, in an additional article Wierzbicki *et al.*⁷⁴ stated that two sets of gold (0.03 mm thick) and cadmium (0.5 mm thick) foils were used. The total thermal neutron fluence at 3 cm was stated as 1.82×10^6 n/cm² where the thermal neutron flux yield was expressed as a fluence rather than as a fluence rate, n/cm²-s, or a function of source strength, n/cm²-h- μ g.

In a later study by Wierzbicki *et al.*,⁷⁵ the thermal neutron fluence rate was determined using a single ²⁵²Cf industrial source of 5812 μ g at ORNL. The source was centered within a water phantom of unstated dimensions. Paired gold and cadmium covered gold foils were arranged over a radial range of 1 to 10 cm. Raw data was not presented and only the difference in activated activities were used. Gold and cadmium foil thicknesses were not stated. The water temperature and precise irradiation time were also not stated; however, these experimental parameters were approximately room temperature and a couple of hours.⁷⁶ At a distance of 5 cm, the thermal neutron flux was approximately 0.1 n/cm²-s. This value does not compare well with the previous data of Wierzbicki *et al.*^{73,74} Results determined herein using Monte Carlo methods and gold foil experiments following the ASTM E 262-86e protocol obtained thermal neutron fluence rates which were incomparable with the data of Wierzbicki *et al.*⁷³⁻⁷⁵ because the data sets did not share common units, and key information was missing. As the magnitude of the thermal neutron fluence rate was expected to be dependent on phantom sizes, due to increased thermal neutron scattering by larger phantoms, a direct comparison between results of others would need to account for this.

V. CONCLUSIONS

Measurements of absolute thermal neutron fluence, according to the ASTM E 262-86e protocol, were in good agreement ($\pm 5\%$) with results determined by Monte Carlo calculation. At a distance of 5.0 cm along the ^{252}Cf AT source transverse axis, the calculated and measured thermal neutron fluence rates were $1.998 \times 10^4 \pm 1800$ and $1.702 \times 10^4 \pm 1020 \text{ n}_{\text{th}}/\text{cm}^2\text{-s-}\mu\text{g}$, respectively. Comparisons of the thermal neutron fluence rate as a function of distance between the calculated (MCNP) and measured (TLD) techniques demonstrated agreement within $\pm 3\%$, which was well the estimated uncertainties. Finally, comparisons of the thermal neutron fluence rate of water, brain, muscle, and A-150 plastic revealed similarities in the fall-off of as a function of increasing distance, yet revealed A-150 as the optimal neutron moderator due to its high hydrogen mass content.

CHAPTER 5

CALCULATED BORON NEUTRON CAPTURE DOSE AND MODERATED ^{252}Cf NEUTRON ENERGY SPECTRA IN BRAIN TISSUE

I. INTRODUCTION

As ^{252}Cf is a fast neutron emitter of relatively low average energy, there is potential to augment ^{252}Cf brachytherapy with boron neutron capture (BNC) dose enhancement for treatment of malignant disease. ^{252}Cf neutrons moderate within the human tissue and may be captured through the $^{10}\text{B}(n,\alpha)^7\text{Li}$ nuclear reaction, $Q = 2.79$ MeV. Following this nuclear capture, a 477.6 keV photon is emitted 93.7% of the time by relaxation of the excited ^7Li nucleus; however, the large majority of locally absorbed high linear energy transfer (LET) dose is deposited by the alpha particle and lithium ion. Consequently, it is possible that, with ^{10}B -loaded drugs which have affinity towards malignant tumor cells, ^{252}Cf brachytherapy may benefit from BNC dose enhancement. Calculations of the BNC dose enhancement are made for a variety of ^{10}B loadings and sizes of phantom material composed of, as an illustration, of brain tissue, as well for tumors of diameter ranging from 2 to 6 cm. Additionally, the moderated ^{252}Cf neutron energy spectrum is examined to demonstrate perturbation of the thermal neutron flux by increasing ^{10}B loadings.

II. MATERIALS AND METHODS

In this calculative study, MCNP¹ was used in a distributed computing environment³⁵⁻³⁷ for brisk computation of the neutron energy spectrum and of boron neutron capture reactions (BNCR). To permit accurate thermal neutron transport, the MCNP solid-state $S(\alpha,\beta)$ neutron scattering library (lwtr.01t) was used to model low energy neutron transport on hydrogen.³⁷ Spherical geometry was used throughout with a ^{252}Cf point source positioned

centrally. The entire volume was divided into radial bins using spheres of varying radii to permit spatial resolution. The phantom diameters ranged from 10 to 30 cm, and the ^{252}Cf neutron energy spectrum was modeled with an isotropic Maxwellian distribution.²⁶

Neutron transport was calculated with ICRU 44 brain material and a mass density of 1.04 g/cm^3 .³⁸ This material was loaded with uniform concentrations of ^{10}B ranging from 1 to $500 \mu\text{g } ^{10}\text{B}$ per gram of brain tissue. Unlike the approach of Zamenhof *et al.*⁷⁷ where neutron fluxes were convolved with kerma to dose conversion factors, the BNCR dose was calculated using a dose deposition formalism as presented in Equation 1 where only the high LET dose was determined.

$$D_{\text{BNCR}}(r,S,L) = 133.488 \frac{(2.34 \text{ NCR})}{\rho} \quad (1)$$

where:

$D_{\text{BNCR}}(r,S,L)$	= high LET BNCR dose rate	[cGy/h- μg]
r	= radius from phantom center	[cm]
S	= ^{252}Cf source strength	[μg]
L	= $\mu\text{g } ^{10}\text{B}$ loading per gram brain tissue	[dimensionless]
133.488	= conversion factor, MeV/g-neutron to cGy/h- μg	[dimensionless]
2.34	= high LET energy deposited by α and ^6Li nuclei	[MeV/NCR]
NCR	= calculated neutron capture reaction rate	[NCR/neutron- cm^3]
ρ	= mass density of ICRU 44 brain	[g/cm^3]

Two additional studies were performed; the first examined BNCR dose as a function of radius in which $10 \mu\text{g } ^{10}\text{B}$ per gram of brain tissue (10 ppm) was uniformly distributed throughout a 15 cm diameter head phantom. A centrally positioned tumor was modeled with a ^{10}B loading of 30 ppm with tumor diameter ranging from 2 to 6 cm. These loadings were used to model a clinical environment of appropriate sized tumors and ^{10}B tumor loadings with a tumor:healthy brain ^{10}B specificity ratio of 3:1.

The second additional study evaluated the impact of placing a 50 cm diameter sphere of D_2O around a 15 cm diameter sphere of brain tissue uniformly loaded with 30

ppm ^{10}B . As D_2O both scatters neutrons and has a thermal neutron capture cross-section less than that of water or brain tissue, it was considered as a useful scattering material to increase the BNCR dose rate. While additional material at the head phantom periphery would most certainly increase the BNCR dose rate, the purpose of this study was to determine if the D_2O altered the calculated high LET dose distribution in a beneficial manner as defined by improving the relative peripheral high LET dose rate. For all studies, the neutron energy spectrum at each radii was divided into energy bins from 1 meV to 15.85 MeV with 10 energy bins per decade of energy.

III. RESULTS

A. Calculated BNCR Dose Rate for a Variety of ^{10}B Loadings and Phantom Sizes

For a brain phantom with a diameter of 15 cm, the impact of ^{10}B loading and radial position on the calculated BNCR dose rate was determined. Figure 1 presents the calculated BNCR dose rate (cGy/h-ppm ^{10}B -mg ^{252}Cf) for radii of 0.5, 1, 2, 3, 4, and 5 cm where straight lines are provided to guide the eye between calculated values. When displayed in this manner, it is evident that for increasing ^{10}B loadings, the BNCR dose rate did not increase linearly. This effect was most apparent for the larger radii where the proportion of thermal neutrons was highest, yet the impact of thermal neutron burnup and ^{10}B self-shielding was greatest. For clinically relevant ^{10}B loadings of 10 and 30 ppm, the degree of non-linearity was -5% and -14%, respectively for all distances, 0.25 to 7.0 cm, examined. The impact of phantom size upon the calculated BNCR dose rate was examined at radii of 0.5, 1, 2, and 5 cm in Figure 2 with a ^{10}B concentration of 30 ppm. At a radius of 5 cm, the BNCR dose rate increased 47%, from 8.5 to 12.5 cGy/h-mg, when examining phanta with diameters of 15 and 30 cm,

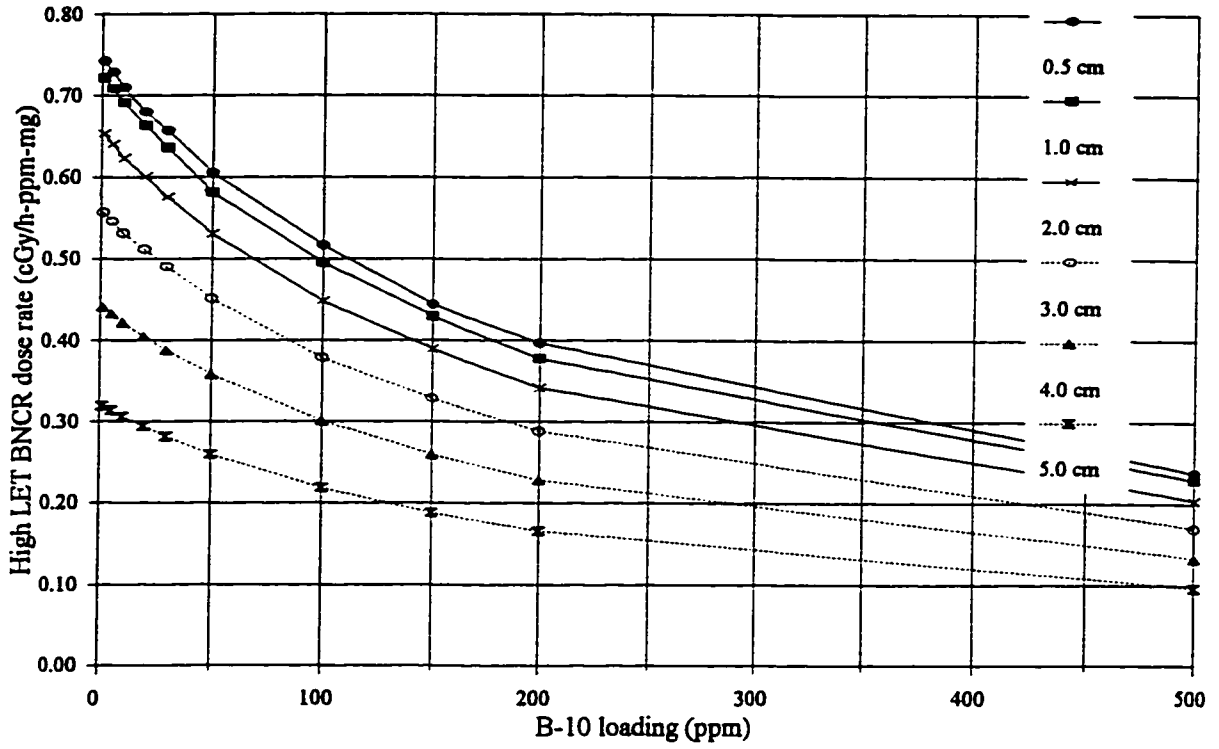


Figure 1. Impact of ^{10}B loading on the calculated BNCR dose rate in a 15 cm diameter brain phantom.

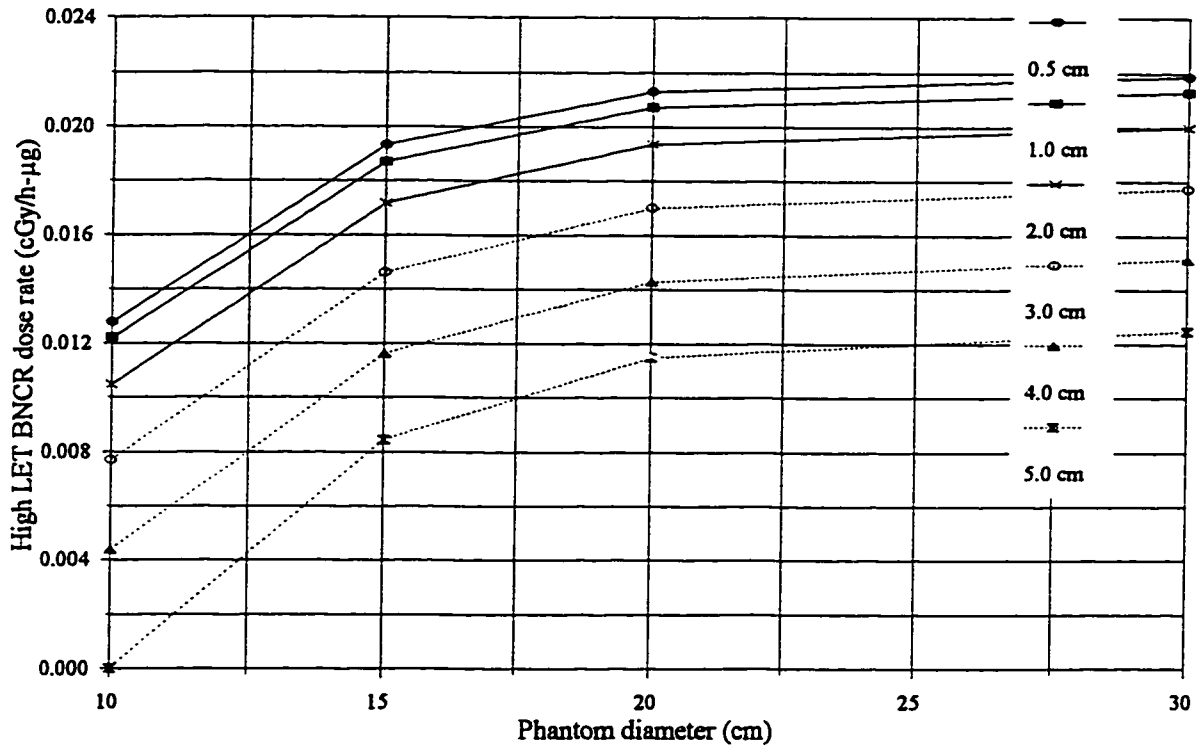


Figure 2. Impact of phantom size on the calculated BNCR dose rate in brain loaded with 30 ppm ^{10}B .

respectively. At a radius of 1 cm, there was a 74% increase in BNCR dose rate for diameters of 10 and 30 cm. Evidently, the presence of scattering material increased the BNCR dose rate due to inscatter of thermal neutrons which would have otherwise exited the phantom volume.

B. Calculated BNCR Dose Rate for a Clinical Tumor Model

High LET dose distributions for BNCR enhanced ^{252}Cf brachytherapy are presented for tumors with diameters ranging from 2 to 6 cm in Figure 3. For comparison, the ^{252}Cf fast neutron dose rate is also shown. For a small quantity of microscopic disease positioned at a radius of 5 cm with a ^{10}B loading of 30 ppm, there was a 9.4% high LET BNCR dose enhancement at this point.

C. Impact of D_2O on the Calculated BNCR Dose Distribution

The ^{252}Cf fast neutron and BNCR dose rates as a function of radius with and without the

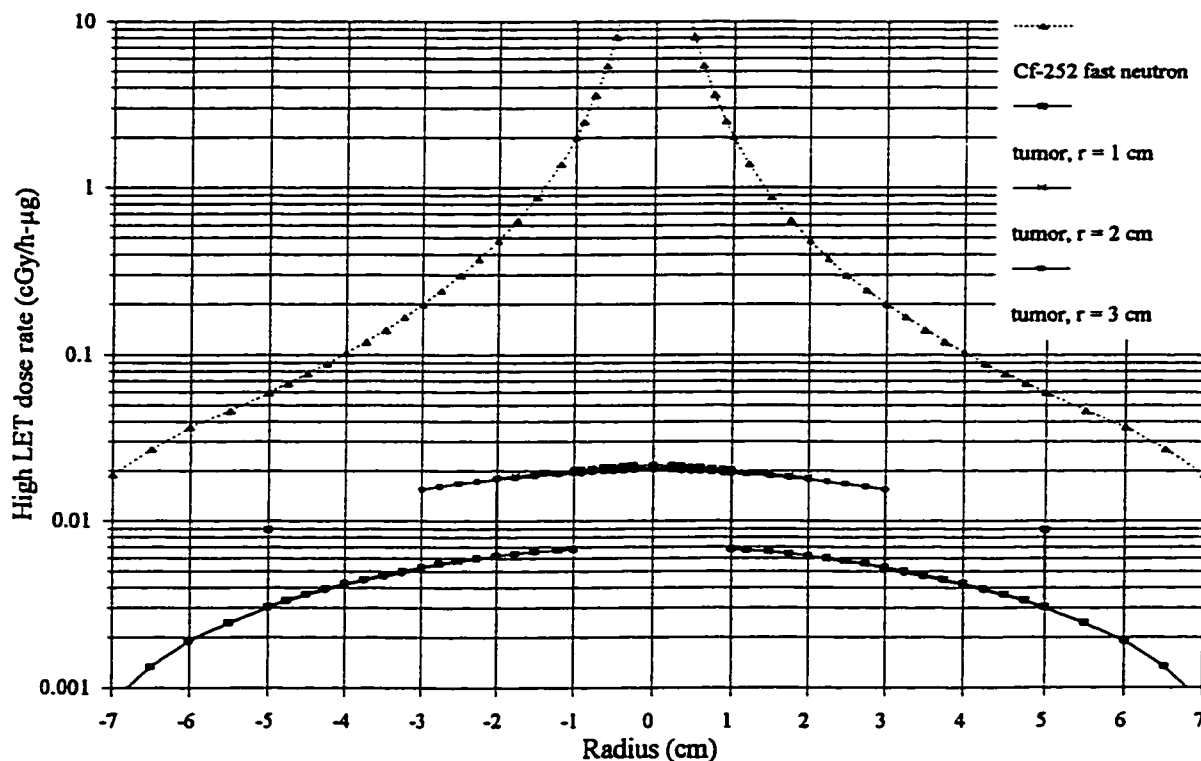


Figure 3. High LET dose distribution for a clinical tumor model of BNCR enhanced ^{252}Cf brachytherapy.

50 cm diameter D₂O sphere are presented in Figure 4. When normalizing fast neutron and BNCR dose rates with the 50 cm diameter D₂O sphere in place to those without the D₂O sphere, it is evident (Figure 5) that both peripheral dose rates are significantly enhanced.

D. Calculated ²⁵²Cf Neutron Energy Spectra

For a 15 cm diameter brain phantom with a 30 ppm ¹⁰B loading, Figure 6 illustrates the impact on the neutron energy spectrum for varying radii. The gradual decrease of neutrons with thermal energies, compared to the near r^{-2} fall-off of the fast component, is apparent. The neutron energy spectrum at 5 cm is displayed in Figure 7 for the same phantom; however, the ¹⁰B loading varies from 1 to 500 ppm. Finally, in Figure 8 are the neutron energy spectra at a radius of 3 cm with a 30 ppm ¹⁰B loading for phanta with diameters from 10 to 20 cm.

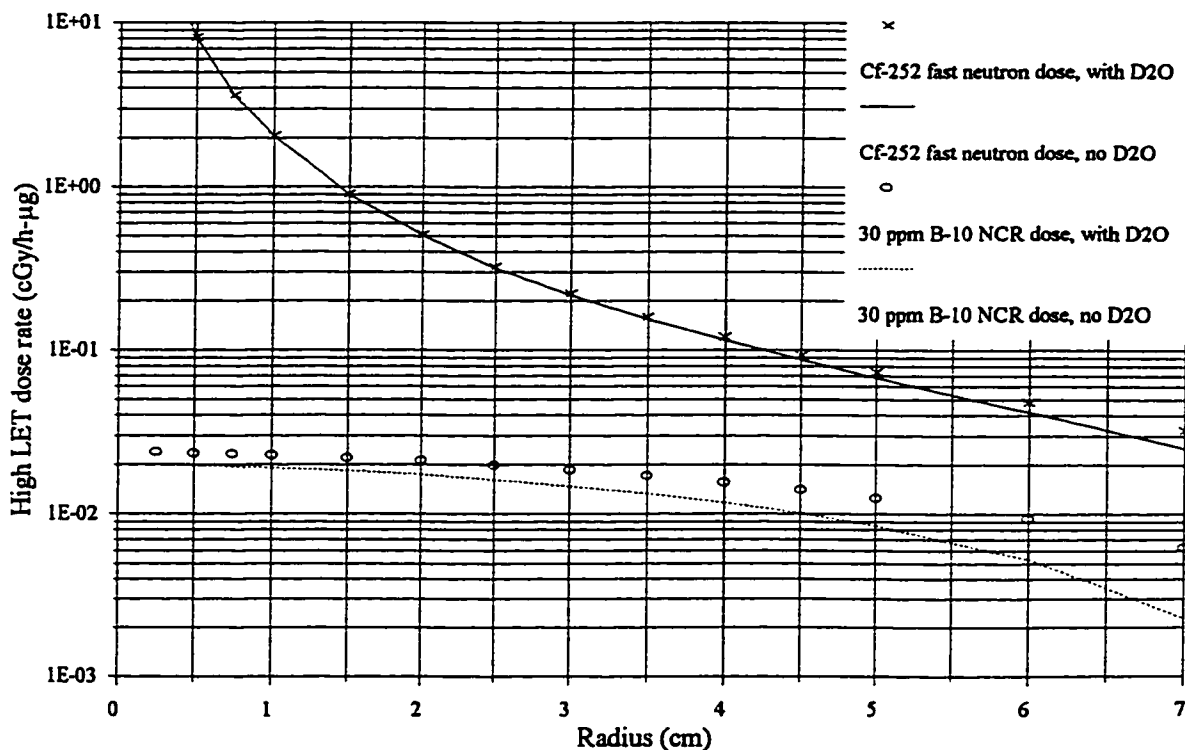


Figure 4. BNCR dose rate in a head phantom with / without a D₂O reflector.

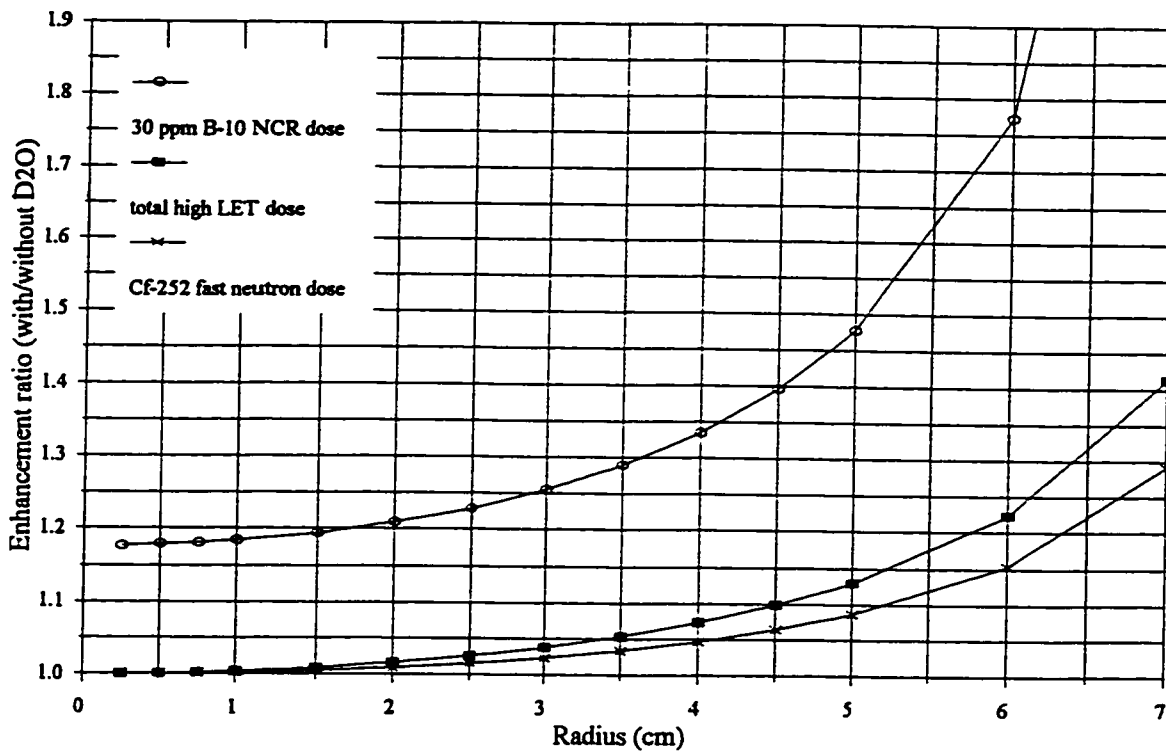


Figure 5. Normalized ^{252}Cf fast neutron and BNCR dose enhancements with a D_2O reflector.

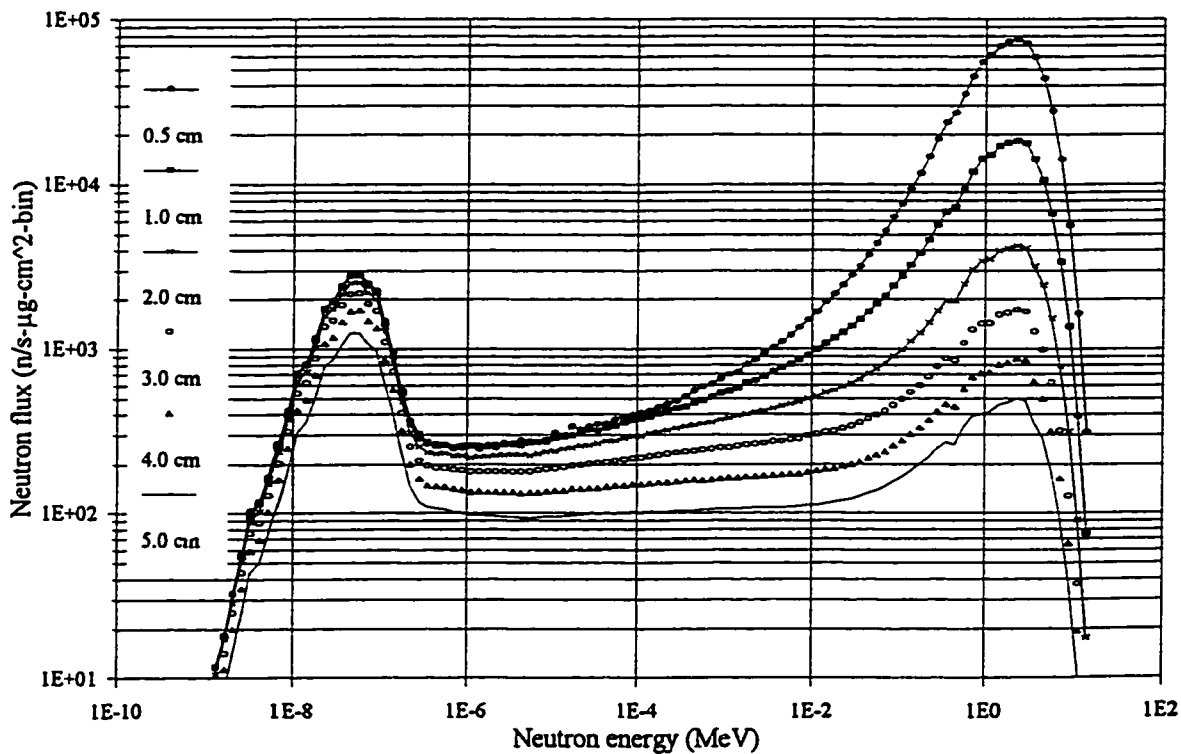


Figure 6. Moderated ^{252}Cf neutron energy spectrum at 0.5, 1.0, 2.0, 3.0, 4.0, and 5.0 cm with 30 ppm ^{10}B .

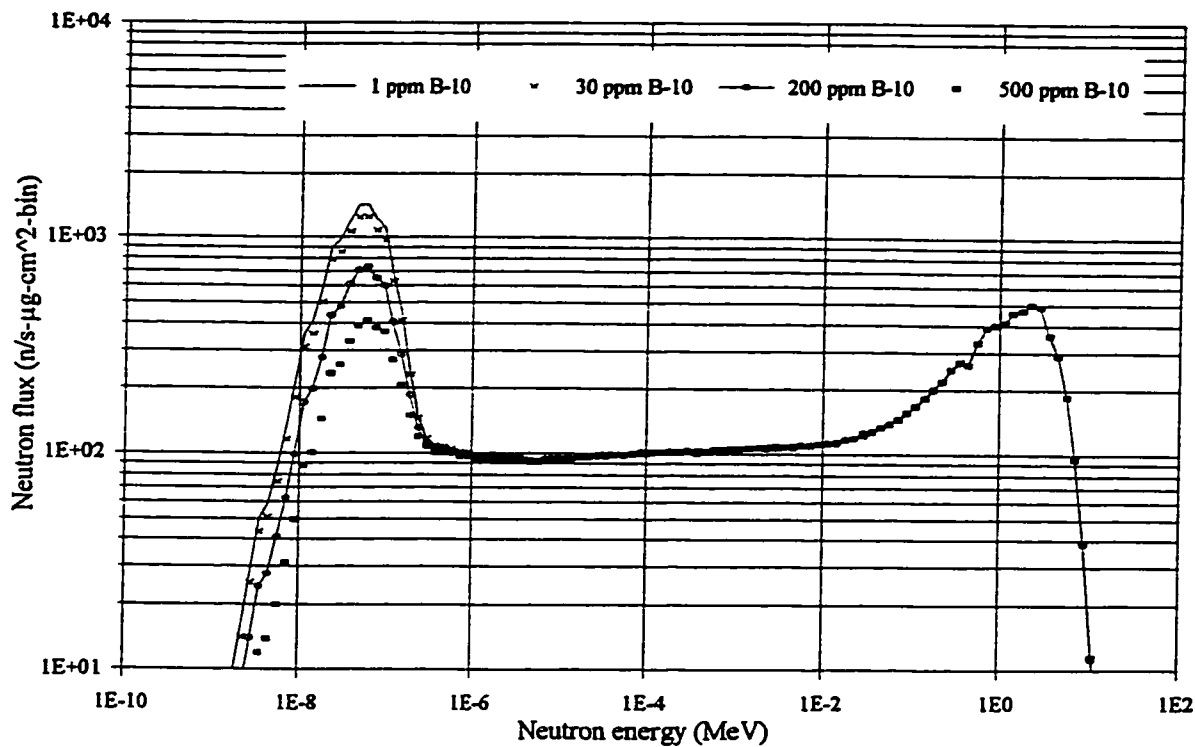


Figure 7. Moderated ^{252}Cf neutron energy spectrum for ^{10}B loadings of 1 to 500 ppm at 5 cm.

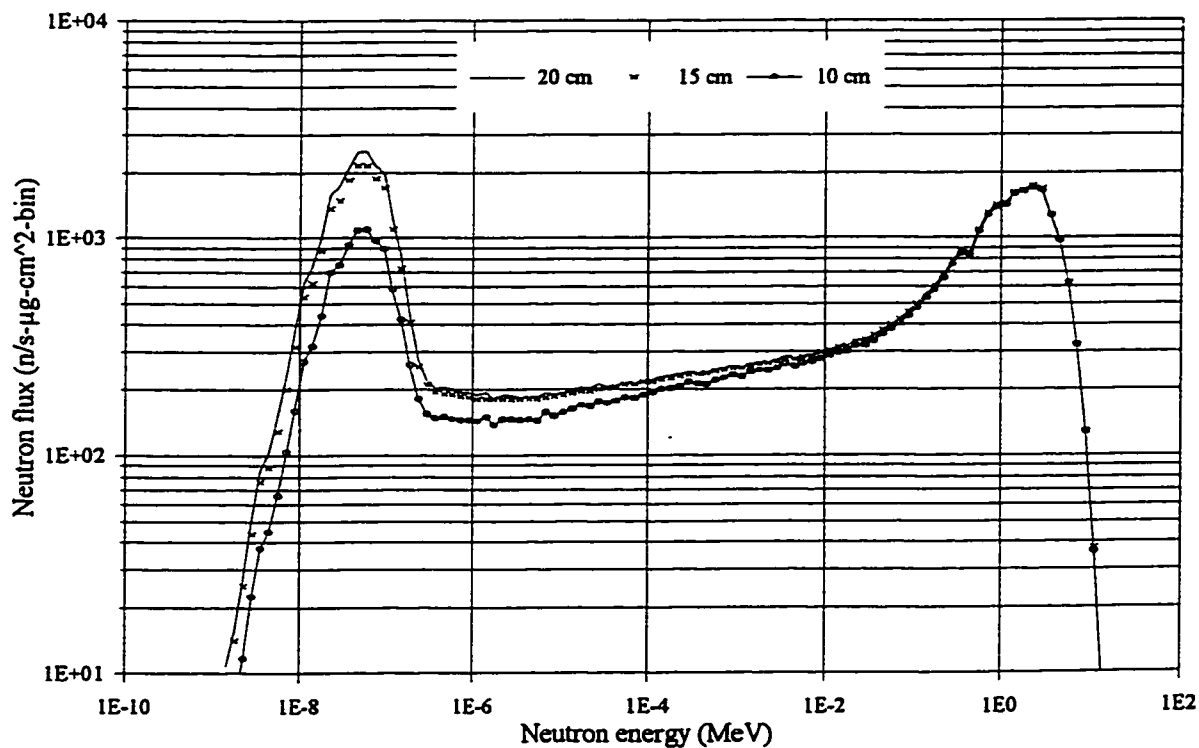


Figure 8. Moderated ^{252}Cf neutron energy spectrum for a variety of phantom sizes at 3 cm.

IV. DISCUSSION

A. Clinical Impact of BNCR Dose Enhancement on ^{252}Cf Brachytherapy

To assay the clinical utility of BNCR dose enhancement at 5 cm from the ^{252}Cf source, one must incorporate relative biological effectiveness (RBE) values for each type of high LET radiation. Using a ^{252}Cf fast neutron RBE of 3.5 for the both healthy brain and microscopic tumor cells,⁶¹⁻⁶³ and a BNCR RBE of 1.3 and 3.8 for healthy brain and microscopic tumor cells, respectively,^{78,79} the total healthy and microscopic tumor high LET dose-eq rates are derived as 0.210 and 0.240 cGy-eq/h- μg , respectively. If one assumes the low LET ^{252}Cf photon and $^1\text{H}(n,\gamma)$, dose distributions are approximately similar to that of the fast neutron dose rate, and that their intensities relative to the ^{252}Cf fast neutron dose rate are about 40% and 1%, respectively,⁵⁶ then the ^{252}Cf low LET photon dose to healthy brain and microscopic tumor cells at 5 cm is 0.0242 cGy/h- μg . The final low LET dose component is from the 478 keV photons. If the $^{10}\text{B}(n,\gamma)$ dose distribution is approximately similar to that of the $^{10}\text{B}(n,\alpha)^7\text{Li}$ dose rate, and a relative intensity of 13% is taken by estimating the mean chord length and energy deposition by 0.48 MeV photons,⁸⁰ then the $^{10}\text{B}(n,\gamma)$ dose rate to healthy brain and microscopic tumor cells at 5 cm is 0.0004 cGy/h- μg . The sum of the low LET dose rates to both healthy brain and microscopic tumor cells is 0.025 cGy/h- μg . Summing the low LET photon doses with the high LET doses yields a total BNCR dose-eq of 0.235 and 0.265 cGy-eq/h- μg for the healthy brain and microscopic tumor cells, respectively. Thus, the dose-eq enhancement is 12.7% at 5 cm in a 15 cm brain phantom with a ^{10}B loading of 30 ppm and a drug specificity in tumor:healthy tissue of 3:1. Using this methodology, dose-eq enhancements of 0.6% and 6.5% were obtained at distances of 1 and 3 cm, respectively.

The clinical significance of the ^{10}B enhancement for ^{252}Cf brachytherapy was minimal considering the ^{10}B loadings and RBE factors used in this analysis. If drugs are developed which could deliver an order of magnitude greater ^{10}B loading with improved tissue specificity, then ^{10}B enhanced ^{252}Cf brachytherapy may be clinically feasible.

B. Impact of D_2O on the Calculated BNCR Dose Distribution

While it was evident that the BNCR dose distribution was enhanced through addition of a large D_2O reflector, the merit of such efforts are questionable. At a 6 cm radius, there is a 15.4% enhancement in the ^{252}Cf fast neutron dose rate and 77.3% enhancement in the BNCR dose rate as shown in Figure 5. If one conservatively excludes all BNCR dose enhancement from the healthy tissue dose, as would be the case for a perfect tumor seeking drug, then estimates of the total high LET dose enhancement may be performed. From Table 1, the healthy tissue and microscopic disease dose enhancements upon use of the D_2O reflector are 8.6% and 13.0%, respectively, with a therapeutic ratio of 4.0%.

Table 1. ^{252}Cf brachytherapy and BNCR enhancement at 6.0 cm with a D_2O reflector.

radiation component	without D_2O reflector		with D_2O reflector	
	healthy tissue (cGy/ $\mu\text{g}\cdot\text{h}$)	tumor (cGy/ $\mu\text{g}\cdot\text{h}$)	healthy tissue (cGy/ $\mu\text{g}\cdot\text{h}$)	tumor (cGy/ $\mu\text{g}\cdot\text{h}$)
^{252}Cf fast neutron	0.06789	0.06789	0.07374	0.07374
30 ppm BNCR	0.00000	0.00845	0.00000	0.01249
total high LET	0.06789	0.07634	0.07374	0.08623

As the fast neutron dose rate in brain tissue from a point source at a distance of 5.0 is approximately 30 times less than that at the typical prescription distance of 1.0 cm, this 4.0% enhancement of a 3% prescription dose rate is considered clinically insignificant. Should drugs be developed which can attain significantly higher loadings and maintain tumor specificity, then BNCR dose enhanced ^{252}Cf brachytherapy with use of neutron

reflecting materials may be reevaluated for clinical use.

C. Comparison of BNCT Dosimetry Results with Others

There are two useful studies in the literature which ascertain the BNCR dose enhancement to ^{252}Cf brachytherapy.^{48,75} Wierzbicki *et al.* measured the thermal neutron flux around a 6 mg ^{252}Cf source in water using gold foils.⁷⁵ Yanch and Zamenhof calculated (MCNP3A) the thermal neutron flux in water around a ^{252}Cf medical source.⁴⁸ A comparison of these results for 50 ppm ^{10}B are made in Table 2. Calculations by Yanch and Zamenhof were

Table 2. BNCR dose enhancement for ^{252}Cf brachytherapy and 50 ppm ^{10}B .

radius (cm)	Wierzbicki <i>et al.</i> (cGy/h- μg)	Yanch and Zamenhof (cGy/h- μg)	this study (cGy/h- μg)
1	0.029 \pm 5%	0.1 \pm 0.1	0.0291 \pm 0.26%
2	0.032 \pm 5%	0.04 \pm 0.01	0.0265 \pm 0.15%
3	0.026 \pm 5%	0.031 \pm 0.01	0.0226 \pm 0.11%
4	0.022 \pm 5%	0.015 \pm 0.01	0.0179 \pm 0.10%
5	0.020 \pm 5%	0.01 \pm 0.01	0.0130 \pm 0.09%
6	0.015 \pm 5%	0.019 \pm 0.001	0.0082 \pm 0.09%
7	0.012 \pm 5%	0.014 \pm 0.001	0.0035 \pm 0.10%
8	0.011 \pm 5%	0.011 \pm 0.001	---
9	0.009 \pm 5%	0.009 \pm 0.001	---
10	0.007 \pm 5%	0.006 \pm 0.001	---

performed at room temperature in water employing the $S(\alpha,\beta)$ thermal neutron treatment.

As for the neutron and photon dosimetry determined above, a macroscopic approach was also used to derive the high LET dose from boron neutron capture reactions. A locally deposited high LET energy of 2.3 MeV was attributed to the $^{10}\text{B}(n,\alpha)$ reaction. No perturbation of thermal neutron flux by ^{10}B was assumed, and a linear response of ^{10}B neutron capture dose versus loading up to 100 $\mu\text{g/g}$ was presented (Table V). In Table VI of Yanch and Zamenhof,⁴⁸ results by Wierzbicki *et al.*⁷⁴ were misrepresented as the

$^{10}\text{B}(n,\alpha)$ dose rate for 50 $\mu\text{g/g}$ ^{10}B at 3.0 cm by Yanch *et al.*⁸¹ Furthermore, differences in $^{10}\text{B}(n,\alpha)$ dose rates between the various groups in Table VI may be expected due to differences in phantom size (inscattering) and composition (^1H content).

Results from Table VI appeared inconsistent with those of Tables III and IV.⁴⁸ The cited $^{10}\text{B}(n,\alpha)$ dose rate at 3.0 cm and 50 $\mu\text{g/g}$ ^{10}B in Table VI was 0.031 cGy/h- μg , while the total (neutron plus photon) dose rate at 3.0 cm from Table III was cited as 0.3500 cGy/h- μg . Though these two values did correctly sum to 0.38 cGy/h- μg as presented in Table IV, the percentage increase upon using these numbers is not consistent with those presented in Table V. If one simply takes the ratio of 0.3800 and 0.3500, a $^{10}\text{B}(n,\alpha)$ dose enhancement of 8.57% is obtained. If the sum of 0.031 and 0.3500 (0.3810) is divided by 0.3500, a $^{10}\text{B}(n,\alpha)$ dose enhancement of 8.86% is obtained. Both these values are greater than 7.7%, the cited 50 $\mu\text{g/g}$ 5.0 cm value, implying that the $^{10}\text{B}(n,\alpha)$ dose enhancement did not increase monotonically from 1 to 15.0 cm as presented in Table V. However, this inconsistency might be attributed to rounding errors in Table III and IV. Also, it was not clear why the 1 $\mu\text{g/g}$ data in Table V at distances of 1, 5, and 10 cm were not properly rounded from their 100 $\mu\text{g/g}$ values since the $^{10}\text{B}(n,\alpha)$ dose was assumed linear as a function of loading.

Finally, the section addressing clinical tumor control probabilities and clinical dose enhancement is flawed.⁴⁸ An 18% $^{10}\text{B}(n,\alpha)$ dose enhancement with 50 $\mu\text{g/g}$ ^{10}B at 10.0 cm was cited within the text, but contradicts that presented in Table V (23.1%) for 50 $\mu\text{g/g}$ ^{10}B at 10.0 cm.⁴⁸ Furthermore, these postulations of dose enhancement were meaningless as estimates of dose-equivalents were ignored. Thus, the relation between absorbed dose from $^{10}\text{B}(n,\alpha)$ + total ^{252}Cf dose and Figure 6 of this article were not warranted.⁴⁸

Differences between results of others and those determined herein are attributed to differences in phantom sizes and methodology. From Figure 2, it is evident that future comparisons of calculated BNCR dose enhancement for ^{252}Cf brachytherapy should state phantom size used, and possibly present results for a variety of sizes. Regardless, the dosimetric impact of 50 ppm ^{10}B on ^{252}Cf brachytherapy is minimal.

V. CONCLUSIONS

Calculations of the ^{10}B enhanced ^{252}Cf brachytherapy were performed using MCNP. Though there was significant moderation of the ^{252}Cf fast neutrons, as evidenced by the neutron energy spectra, the magnitude of the BNCR dose enhancements were small compared to the ^{252}Cf fast neutron dose. As expected, ^{10}B loadings up to 500 ppm did not significantly alter the ^{252}Cf fast neutron energy spectrum. Attempts at improving the thermal neutron flux through addition of a D_2O moderator caused minimal enhancement. Though the neutrons emitted by ^{252}Cf are of relatively low energy compared with other fast neutron sources, the fast neutron dose dominated over the BNCR dose enhancement for ^{10}B loadings less than 50 ppm. Consequently, ^{252}Cf does not appear to be a useful source for BNCR enhanced radiotherapy using the aforementioned ^{10}B loadings and RBE factors used in the derivation of this conclusion.

CHAPTER 6

CALCULATION AND MEASUREMENT OF PHOTON DOSE

FROM THE ^{157}Gd NEUTRON CAPTURE REACTION

I. INTRODUCTION

Though the efficacy of the $^{157}\text{Gd}(n,\gamma)^{158}\text{Gd}$ neutron capture reaction (NCR) has yet to be demonstrated in humans, there is merit to studying the potential benefits of this modality. In this study, the photon dosimetry of GdNCR enhanced ^{252}Cf fast neutron brachytherapy is examined. Calculations were performed using Monte Carlo methods while experimental measurements were made of the ^{158}Gd photon dose using ^{252}Cf AT sources. These were performed to determine the GdNCR photon dose enhancement in a variety of conditions.

II. MATERIALS AND METHODS

A. Calculative Methodology

MCNP¹ was used for the calculative portions of this study in a distributed computing environment using 6 UNIX-based computers.³⁵⁻³⁷ Spheres 15 cm in diameter composed of water and ICRU brain³⁸ were modeled with uniform ^{157}Gd loadings ranging from 0 to 5000 $\mu\text{g } ^{157}\text{Gd}$ per gram (ppm) of material. The entire volume was divided into radial bins using spheres of varying radii to permit spatial resolution. An unencapsulated ^{252}Cf point source was positioned at the center of each sphere to mimic a ^{252}Cf HDR source. As recommended by Anderson,²⁶ the neutron energy spectrum was modeled as an isotropic Maxwellian distribution with an energy fitting parameter of 1.42 MeV. To permit accurate thermal neutron transport, the MCNP solid-state $S(\alpha,\beta)$ neutron scattering library (lwtr.01t) was used to model low energy neutron transport on hydrogen within ^{157}Gd -loaded media.³⁷ The only ^{157}Gd library which permitted MCNP to generate prompt

photons following the $^{157}\text{Gd}(n,\gamma)^{158*}\text{Gd}$ NCR was the NJOY processed data set (64157.55c).¹ This library was developed at Los Alamos National Laboratory (LANL), and is a modified version of the ENDF/B-V data library.⁸² MCNP cannot generate prompt electrons following neutron capture. However, this was not considered detrimental as there are no data libraries describing energies or yields of these electrons and there are no drug agents which can deliver ^{157}Gd to the cell nuclei of neoplastic tissue to take advantage of high LET electrons resulting from the capture reaction

To calculate energy deposition, and subsequently absorbed dose, from electrons set into motion by photons following $^{158*}\text{Gd}$ relaxation, Monte Carlo coupled neutron-photon-electron (n-p-e) transport was necessary. Calculations typically required transport of 10^6 particles. However, an extended Monte Carlo run was made where 7×10^7 particles were transported. As the average photon energy following $^{158*}\text{Gd}$ relaxation is approximately 1.5 MeV, over 75% of the photon energy was not deposited within the phantom.⁸² This was determined for a μ_{en} value of 0.0282 cm^{-1} with an average chord length of 10 cm for a 15 cm diameter sphere of water since photon production was considered uniform throughout the sphere instead of originating at the sphere center.⁸³ Consequently, calculation of energy deposition through (n-p-e) transport was inefficient per emitted neutron for the aforementioned reason. The likelihood of interaction was also modest due to low ^{157}Gd loadings and a thermal neutron $^{157}\text{Gd}(n,\gamma)^{158*}\text{Gd}$ cross-section, σ_0 , of $2.55 \times 10^{-19} \text{ cm}^{-2}$.⁸⁴

As a means to calculate absorbed photon dose from the GdNCR directly, a single-event photon dosimetry kernel was produced for the $^{158*}\text{Gd}$ photons in water and brain. The merit of this approach is that convolution of the GdNCR distribution with the photon

dosimetry kernel, or future electron dosimetry kernels, may provide accurate dose distributions in regions distant from boundaries or tissue inhomogeneities.

In addition to calculation of absorbed dose from the ^{158}Gd photons, the neutron and photon energy spectra were also evaluated for each ^{157}Gd loading and radial position. The neutron energy spectrum was divided into energy bins from 1 meV to 15.85 MeV with 10 energy bins per decade of energy while the photon energy spectrum was examined from zero to 9 MeV with 0.1 MeV increments.

B. Experimental Techniques

Inside a 54 liter (28.6 x 30.8 x 61.1 cm³) thin-walled plastic water phantom, four ^{252}Cf AT sources were circumferentially arranged around a 50 cm³ gadolinium solution contained in a thin-walled cylinder used to model a human brain tumor.⁸⁵ The ^{157}Gd solution loadings ranged from 12.3 $\mu\text{g/g}$ to 12.3 mg/g as determined using natural abundance gadolinium and prepared through dilutions of Magnevist[®], a clinical brain contrast agent. Within the solution was placed a miniature, energy compensated GM counter, used to determine the gamma ray dose in the mixed-field as previously described in Chapter 2. The only difference in this section was a different photon sensitivity of $5.12 \pm 0.11 \times 10^{-7}$ cGy/ct. Dose to brain, instead of to muscle, was desired with a brain to air μ_{EN}/ρ ratio of 1.11.

III. RESULTS

A. Calculated GdNCR Photon Dose Rate

The GdNCR photon dose rate enhancement was calculated in brain material with ^{157}Gd loadings of 100 and 1000 ppm. These results are presented (Figure 1) in addition to the background induced photon dose from $^1\text{H}(n,\gamma)^2\text{H}$, and other photon emitting neutron capture reactions. The relative error was approximately 10.7 and 2.5% at 1 and 5 cm for

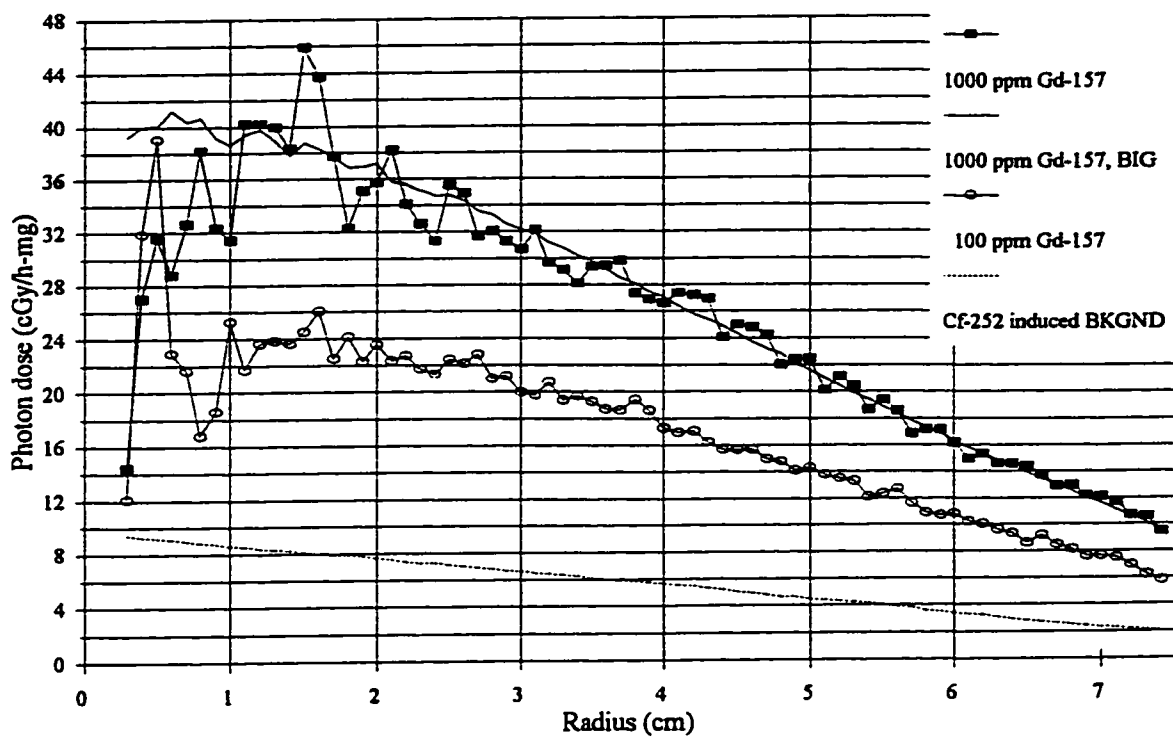


Figure 1. GdNCR photon dose enhancement in brain for 100 and 1000 ppm ^{157}Gd .

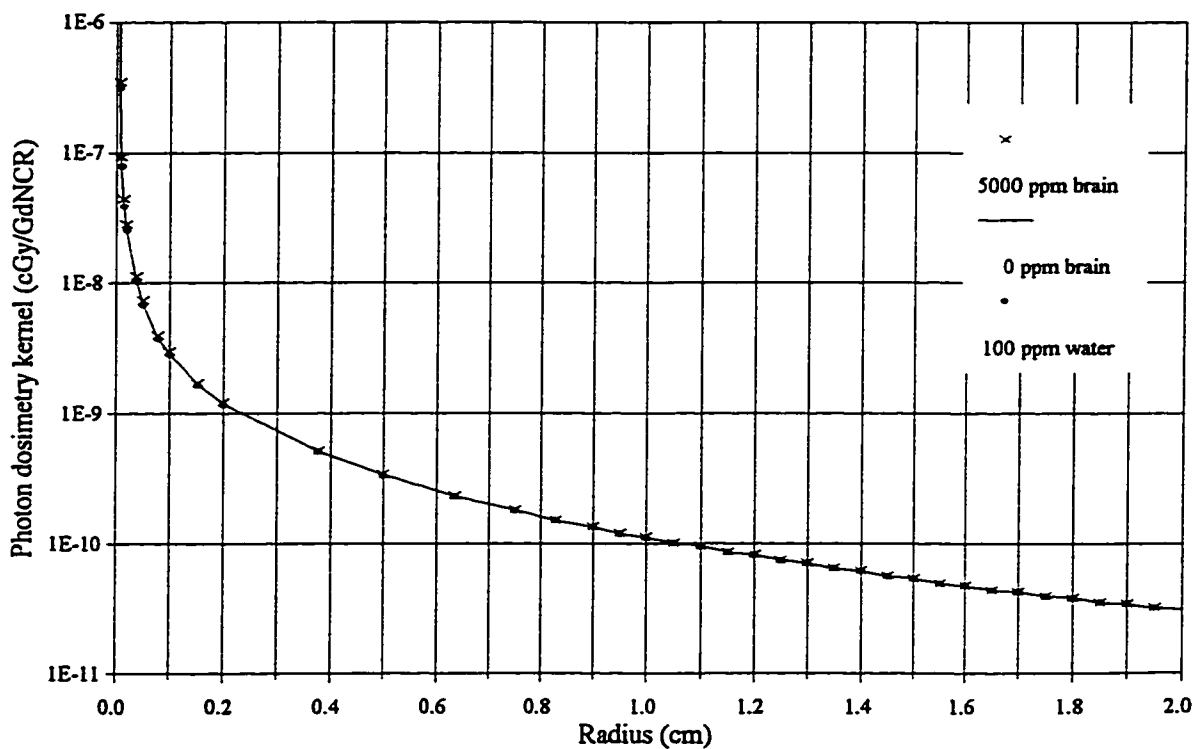


Figure 2. GdNCR photon dose kernel in water and brain.

both loadings. An additional calculation was performed for the 1000 ppm loading where the computer simulation was run for 8 continuous weeks to obtain the data set labeled: *1000 ppm Gd-157, BIG*. At distances of 1 and 5 cm, the relative errors were 1.3 and 0.3%, respectively. Evidently, it was impractical to perform direct GdNCR photon dose enhancement calculations using the aforementioned computer environment.

B. GdNCR Photon Dose Kernel

Single-event dosimetry kernels were produced for the ^{158}Gd photons in 15 cm diameter 15 cm diameter spheres of water and brain material. The calculated data are presented in Figure 2, and then fit to Equation 1, $r > 0.999$, with parameters listed in Table 1. Use of an offset, δ , produced finite dosimetry results at the origin while still providing an accurate curve fit to the calculated data. A conversion efficiency of 2.207 was used for M ,⁸⁶ and the attenuation length, μ_1 , was similar to the 0.0282 cm^{-1} value cited in the Materials and Methods section to justify the chord length estimate.

$$D(r)_{\text{Gd-158}^* \text{ photons}} = \frac{M \alpha e^{-\mu_1 r} (1 - \beta e^{-\mu_2 r})}{(r - \delta)^2} \left[\frac{\text{MeV}}{\text{g}\cdot\gamma} \right] \quad (1)$$

where:

$D(r)$	= absorbed dose in water or brain from GdNCR photons	[cGy/NCR]
M	= conversion efficiency, number of photons per $^{157}\text{GdNCR}$	[γ/NCR]
α	= specific photon dose rate	[cGy/ γ]
β	= scattering intensity	[dimensionless]
δ	= radial offset	[cm]
μ_1	= attenuation length	[cm^{-1}]
μ_2	= scattering length	[cm^{-1}]
r	= the radial distance from source center to point of interest	[cm]

In Table 1, it appears that the μ_1 ratio (1.044) between water and brain were approximately proportional to the ratio of mass densities, 1.00 and 1.04 g/cm^3 , respectively, while the α ratios (0.989) were approximately proportional to the hydrogen

mass density of water (0.112 g/cm³) and brain (0.111 g/cm³).

Table 1. GdNCR photon dosimetry kernel parameters for ²⁵²Cf brachytherapy.

material / ¹⁵⁷ Gd loading	α (cGy/ γ)	β	δ (cm)	μ_1 (cm ⁻¹)	μ_2 (cm ⁻¹)
water / 100 ppm	2.686×10^{-11}	0.967	0.0001	0.0235	2.15
brain / 0 ppm	2.715×10^{-11}	0.967	0.0001	0.0225	2.15
brain / 5000 ppm	2.715×10^{-11}	0.967	0.0001	0.0225	2.15

Using an identical formalism to the radial dose function, $g(r)$, as defined in TG-43, a r^{-2} factor was removed from the GdNCR photon dose kernel due to the decrease expected because of diminishing solid angle with increasing distance.³⁴ In Figure 3, the radial dose function of common brachytherapy sources in water are presented alongside that for the GdNCR photon dose kernel.^{34,67} There were no significant differences between the radial dose functions in water and brain, and between the two brain materials with different loadings.

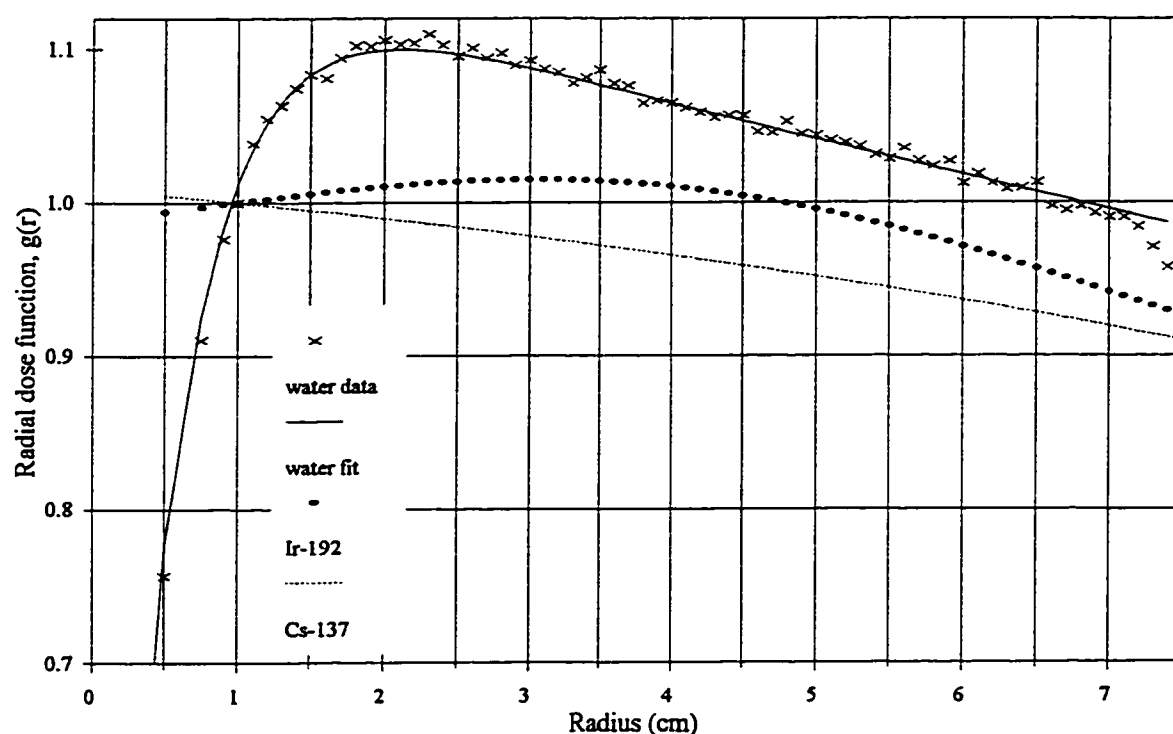


Figure 3. Radial dose functions for GdNCR photons and brachytherapy sources.

The radial dose function values are significantly larger and fall-off significantly slower for increasing depths in comparison to that from the common brachytherapy sources. This was expected as the GdNCR photons are of higher energy than those of the brachytherapy sources, and the radial dose function exhibits a buildup region due to increasing scatter and attenuation with increasing distance from the point source.

C. Neutron Energy Spectra in ^{157}Gd -loaded Brain Material

The moderated ^{252}Cf neutron energy spectrum in brain is presented Figure 4 at 0.5, 1, 2, and 5 cm with a ^{157}Gd loading of 1000 ppm. It is evident that only the thermalized neutrons, those less than 1 eV, were significantly affected by the presence of ^{157}Gd , and that the fast neutrons were unaffected. Figure 5 shows the spatial distribution of ^{157}Gd neutron capture reactions for ^{157}Gd loadings of 100 and 1000 ppm in brain material.

Clearly there was a large degree of non-linearity in the GdNCR density for this factor of

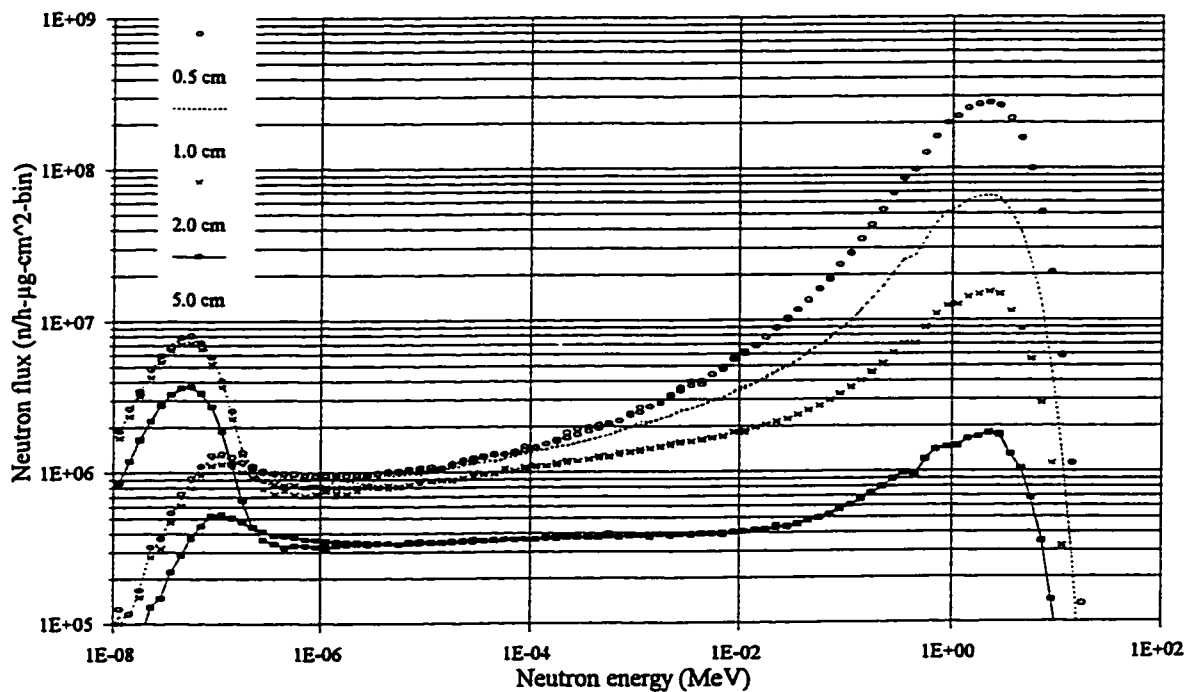


Figure 4. Moderated ^{252}Cf neutron energy spectrum in brain, with / without 1000 ppm ^{157}Gd .

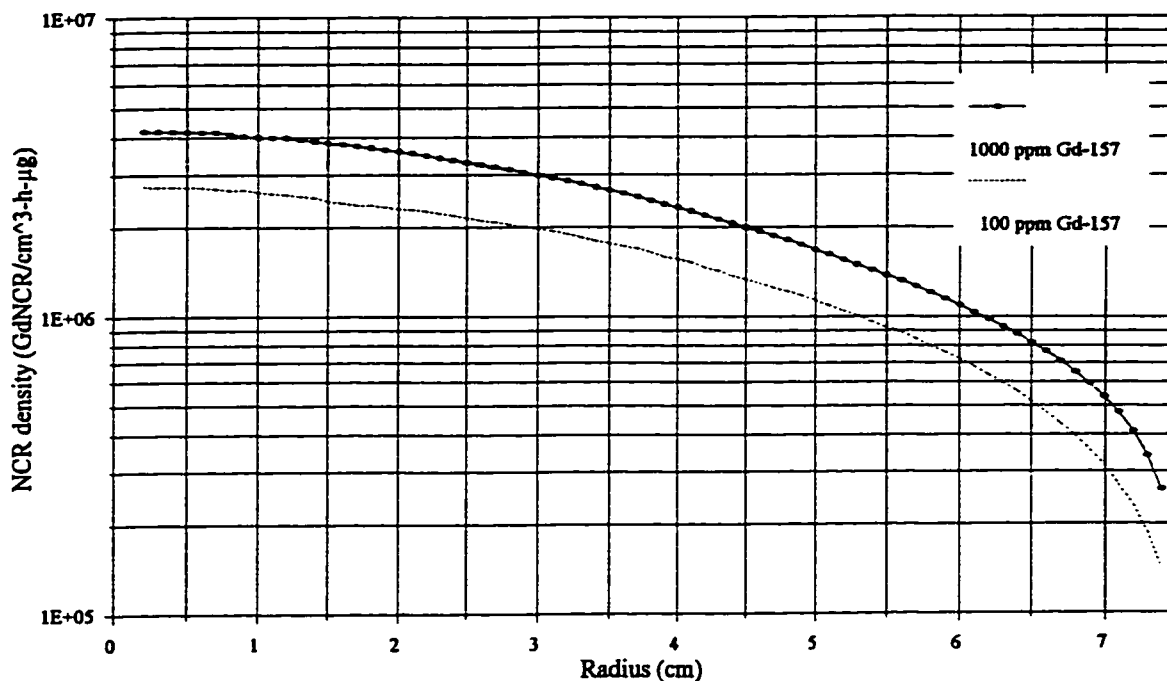


Figure 5. Spatial distribution of GdNCR in brain for ^{157}Gd loadings of 100 and 1000 ppm.

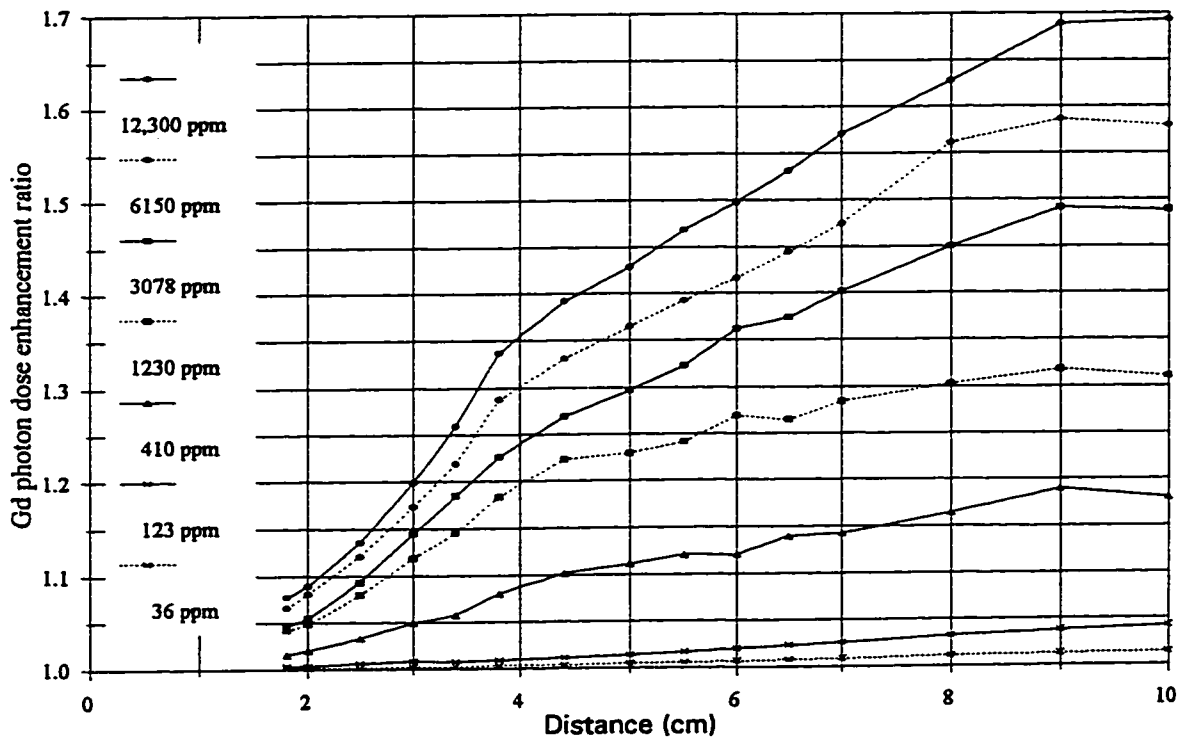
ten increase in ^{157}Gd loading. On average, the 1000 ppm GdNCR density was only a factor of 1.5 ± 0.1 greater than the 100 ppm GdNCR density over all radii examined.

D. Measured GdNCR Photon Dose Enhancement

The measured values of GdNCR photon dose enhancement for various ^{157}Gd loadings are listed in Table 2. Errors associated with all values were estimated at 10% based on reproducibility of GM counter readings upon repositioning the ^{252}Cf sources at a given distance. The ratio of photon dose with / without gadolinium is shown in Figure 6.

Table 2. Photon dose enhancement (cGy/h-mg) for various ^{157}Gd loadings.

distance (cm)	^{157}Gd loading (ppm)						
	12,300	6150	3078	1230	410	123	36
1.8	21.2	18.1	12.8	11.5	4.31	0.974	0.286
2.0	21.7	19.8	13.3	11.6	4.96	0.825	0.275
2.5	21.6	19.2	14.9	12.7	5.30	0.979	0.245
3.0	22.0	19.2	16.0	13.1	5.49	0.912	0.228
3.4	23.9	20.3	17.1	13.4	5.34	0.666	0.222
3.8	24.3	20.7	16.3	13.2	5.83	0.645	0.215
4.4	22.0	18.5	15.1	12.5	5.69	0.630	0.210
5.0	18.6	15.8	12.9	9.95	4.83	0.617	0.206
6.0	15.1	12.6	11.0	8.15	3.64	0.605	0.202
7.0	13.3	11.1	9.36	6.61	3.32	0.598	0.199
8.0	11.4	10.2	8.16	5.48	2.97	0.593	0.198
9.0	10.7	9.12	7.64	4.94	2.96	0.591	0.197
10.0	9.70	8.10	6.83	4.33	2.52	0.589	0.196

**Figure 6.** Measured gadolinium photon dose enhancement ratio.

IV. DISCUSSION

A. Experimental Results

From Table 2 it is evident for all loadings examined that the GdNCR photon dose decreases for both decreasing loadings and for decreasing distances past 3.8 cm. While it is intuitive that with less ^{157}Gd present there should be fewer photons created, it is not obvious why this effect was maximized at approximately 3.5 cm. However, it is likely that at this distance the ^{252}Cf photon dose fall-off was lowest in comparison to the GdNCR photon dose fall-off due to increasing moderation of the ^{252}Cf neutrons.

B. Comparison of GdNCR Photon Dose Enhancement Results with Others

There are only two studies in the literature which assess GdNCR dose enhancement for ^{252}Cf brachytherapy. Results herein differed from Rivard *et al.*⁸⁵ in that a k_U value of 0.025 was used and application of the non-paralyzable model was not properly performed.⁸⁵

Dead-time corrections ($\tau = 35 \mu\text{s}$) were applied to the net GM count rate instead of each measurement.⁸⁵ These discrepancies resulted in GdNCR photon dose enhancement differences of approximately 50% at 1.8 cm and 16% at 3.8 cm for all loadings.

Wierzbicki *et al.*⁷⁵ calculated, based on Brugger and Shih,⁸⁷ the photon dose enhancement of 160 ppm ^{157}Gd based on experimental measurements of the thermal neutron flux around a 6 mg ^{252}Cf source using gold foils in a water phantom.⁷⁵ A comparison of these results for 160 ppm ^{157}Gd are made in Table 3. Results for ^{157}Gd loading of 160 ppm for this study and Rivard *et al.*⁸⁵ were determined through linear interpolation between results with ^{157}Gd loadings of 410 and 123 ppm. Also presented for comparison in Table 3 are Monte Carlo results from Figure 1, for a 15 cm diameter sphere of water, linearly interpolated for 160 ppm between 100 and 1000 ppm ^{157}Gd .

Table 3. Photon dose enhancement for 160 ppm ^{157}Gd .

radii (cm)	Wierzbicki <i>et al.</i> (cGy/h-mg)	this study, calculation (cGy/h-mg)	this study, measurement (cGy/h-mg)	Rivard <i>et al.</i> (cGy/h-mg)
1	71 ± 5%	26 ± 8%	---	---
2	84 ± 5%	24 ± 5%	1.36 ± 10%	0.91 ± 10%
3	68 ± 5%	21 ± 4%	1.50 ± 10%	1.22 ± 10%
4	54 ± 5%	18 ± 4%	1.30 ± 10%	1.27 ± 10%
5	52 ± 5%	15 ± 3%	1.16 ± 10%	1.04 ± 10%
6	39 ± 5%	11 ± 3%	1.00 ± 10%	0.91 ± 10%
7	29 ± 5%	8 ± 4%	0.95 ± 10%	0.88 ± 10%
8	27 ± 5%	---	0.90 ± 10%	0.84 ± 10%
9	19 ± 5%	---	0.90 ± 10%	0.84 ± 10%
10	18 ± 5%	---	0.84 ± 10%	0.79 ± 10%

The differences between results of Wierzbicki *et al.*⁷⁵ and those obtained in this study and by Rivard *et al.*⁸⁵ were attributed to differences in experimental setup. In the experiment by Wierzbicki *et al.*,⁷⁵ no gadolinium was actually present and derivation of the GdNCR photon dose enhancement was based largely on calculative extrapolation of thermal neutron flux measurements. In the latter two studies, the detector was placed within the imitation tumor immediately surrounded by a Gd solution with ^{252}Cf sources extending beyond the tumor periphery. Consequently, the study by Wierzbicki *et al.*⁷⁵ may have overestimated the GdNCR photon dose enhancement due to exclusion of thermal neutron burnup and ^{157}Gd self-shielding, as well as attributing all the energy from the GdNCR to photon production.

GdNCR Photon Dose Estimation and Results of Stepanek

It was determined in the Materials and Methods section that the over 75% (0.754) of the energy from a 1.5 MeV photon would be deposited outside of a sphere of water with a 7.5 cm radius. If a photon μ_{en} value of 0.0280 cm^{-1} at 1.5 MeV for muscle is used with a 10

cm radius sphere, one determines that 68.8% of the energy is deposited outside the sphere. Stepanek determined a similar result (68.0%) after performing Monte Carlo calculations using the GEANT transport code.⁴⁶ Therefore, the assumption that the GdNCR photon average energy may be approximated as 1.5 MeV is well founded.

V. CONCLUSIONS

Calculations of the ^{157}Gd NCR photon dose enhancement for ^{252}Cf brachytherapy were performed, and determined to be infeasible due to time constraints inherent to the computer system available to the author. However, results from a limited number of calculations revealed the majority, about 75%, of the energy released by ^{158}Gd photons was not deposited in a 15 cm diameter sphere of either water or brain material. The negligible clinical impact of low LET, non-tumor specific photon dose as might be observed in $^{157}\text{GdNCT}$ was presented. Analysis of the ^{157}Gd NCR photon dosimetry kernel revealed only slight differences in water brain materials due to the similar average atomic numbers of water and brain material. Spatial resolution of the ^{157}Gd NCR with 100 and 1000 ppm ^{157}Gd in brain was similar in shape to the $^1\text{H}(n,\gamma)^2\text{H}$ NCR spatial distribution. There was significant non-linearity of the ^{157}Gd NCR for increasing ^{157}Gd loadings due to burnup of thermal neutrons. Neutron burnup and perturbation of the moderated ^{252}Cf neutron energy spectrum was evident for neutrons with kinetic energy less than 1 eV due to the presence of 1000 ppm ^{157}Gd . Comparisons of ^{157}Gd NCR photon dose enhancement results with others revealed similar trends in spatial distribution, but markedly different values due to differences in experimental setup. As this study only examined the impact of high energy photons following the ^{157}Gd NCR, no statement can be made as to the predicted efficacy of ^{157}Gd NCR enhanced ^{252}Cf brachytherapy.

CHAPTER 7

HEALTH PHYSICS AND ^{252}Cf

I. SUMMARY OF ^{252}Cf CARCINOGENESIS

Though ^{252}Cf has shown promise in recent years for use as a neutron source for the treatment of cancer,^{58,59} there have been concerns over the increased relative biological effectiveness (RBE) of neutrons to induce carcinogenesis. While the probability of carcinogenesis is a function of radiation quality, total dose, dose rate, and irradiated site, general principles and trends may still be depicted. Based on recommendations from an incontrovertible source, BEIR V,⁸⁸ a quality factor of 20 for neutrons should be used as based on a review of various experiments in the literature. Using revised dosimetry and neutron transport presented in BEIR V,⁸⁹ dosimetry recalculations of the Hiroshima blast revealed a 70% increase and factor of 7 decrease in the free field in air kerma factors of photons and neutrons, respectively.⁹⁴ Consequently, no significant information regarding neutron RBE for carcinogenesis could be obtained from survivors of both cities due to the low proportion of neutron dose to photon dose and poor statistics available.⁸⁹

Additional studies⁹⁰⁻⁹³ reported in BEIR V⁸⁸ examined the low dose or low dose rate carcinogenic potential of neutrons, and specifically the carcinogenic potential of ^{252}Cf . While many *in vitro* studies⁹⁰⁻⁹² determined the neutron RBE exceeded 100 at a dose of just 1 cGy, proper identification of many of the lesions may have been in error.⁹⁴ Using ^{252}Cf , leukemogenesis experiments^{93,95} of mice irradiated to total doses of 2 Gy were performed. Consequently, there were no studies in the literature which addressed the carcinogenic potential of ^{252}Cf at low doses as would be obtained by hospital personnel using ^{252}Cf . Thus the need for conservative shielding of radiation workers using ^{252}Cf .

II. CLEAR-Pb[®] PROPOSED AS A SHIELDING MATERIAL FOR ²⁵²Cf

A. Background

As a means to diminish personnel exposure within our clinic, 30 cm of polymethyl methacrylate (acrylic) is used as a radiation shielding material for protecting both physicists and physicians while engaging in manually afterloaded ²⁵²Cf brachytherapy implants. It was postulated that a lead doped alternative to acrylic, Clear-Pb[®], might provide enhanced utility as a radiation shielding material for ²⁵²Cf. Clear-Pb[®] has many advantages over other shielding materials such as lead bricks or leaded glass due to optical transparency, machinability, and low cost.⁹⁶ Utilizing Monte Carlo methods (MCNP4B),¹ a calculative study was performed to determine whether or not Clear-Pb[®] was superior to acrylic as a radiation shielding material for ²⁵²Cf emissions. The mass attenuation coefficient, μ/ρ , was determined and used to evaluate radiation shielding effectiveness. The mass attenuation coefficients were calculated over a wide range of energies for photons and neutrons, and also for the ²⁵²Cf photon and neutron source spectra.

B. Materials and Methods

Clear-Pb[®] is a commercially available leaded acrylic material designed for radiation protection and shielding.⁹⁶ The elemental mass density of Clear-Pb[®] as provided by the manufacturer is presented in Table 1; for comparison, plain acrylic is also tabulated.^{42,96} These elements and mass densities were used in subsequent Monte Carlo calculations with natural abundance used for neutron transport. It is apparent from Table 1 that the mass densities of hydrogen, carbon, and oxygen did not vary substantially upon introduction of lead into the base acrylic polymer as for Clear-Pb[®]. The majority of neutron kerma is released through elastic scattering on hydrogen. As the hydrogen mass density of Clear-

Pb[®] was 3% less than that of plain acrylic, and the ratio of total mass densities between these same materials was 1.34, an estimate of 1.38 for the ratio of μ/ρ between Clear-Pb[®] and plain acrylic was made.

As Clear-Pb[®] has 30% mass lead incorporated into an acrylic polymer, its utility as compared with plain acrylic as a radiation shielding material was expected to be greatest for photon energies near the lead K-edge, 88 keV, and only for relatively thin samples where the poly-energetic ²⁵²Cf photon spectrum had not yet significantly hardened.

Table 1. Mass densities of Clear-Pb[®] and acrylic.

element	Clear-Pb [®] (g/cm ³)	acrylic (g/cm ³)
hydrogen	0.093	0.096
carbon	0.701	0.714
oxygen	0.326	0.380
lead	0.480	0.000
total	1.600	1.190

Calculational Methodology

Monte Carlo analysis of both Clear-Pb[®] and acrylic as radiation shielding materials was performed using MCNP4B code¹ with a parallel virtual machine³⁵ distributed computational environment as described by Rivard *et al.*³⁷ MCNP4B Monte Carlo code available from ORNL was used. An MCNP input file was written to model the geometrical setup including the ²⁵²Cf source.¹ The geometry was comprised of a 10 meter long right-cylinder with a 1 cm radius and a sample region comprised either of Clear-Pb[®] or plain acrylic of varying thickness placed centrally along its length. A mono-directional, point source was centrally placed at one end of the cylinder and a flux tally cell at the opposite end which employed energy discrimination for the mono-energetic source to demonstrate that the MCNP input geometry was “good geometry”.⁴³ This geometry is

presented (not to scale) in Figure 1.



Figure 1. MCNP calculation geometry.

Equations 1 and 2 were used to manipulate elemental mass attenuation coefficients which were compiled for photons by Hubbell and Seltzer.⁹⁷ Through Monte Carlo calculation of the transmission of a given photon energy and a given sample thickness, the mass attenuation coefficient was derived.⁸³

$$\frac{N}{N_0} = e^{-\rho \left(\frac{\mu}{\rho}\right) L} \quad (1)$$

$$\frac{\mu}{\rho} = \frac{1}{L \rho} \ln \frac{N_0}{N} \quad (2)$$

where:	N =	number of transmitted particles	
	N ₀ =	number of incident particles	
	ρ =	mass density of attenuating material	[g/cm ³]
	μ/ρ =	mass attenuation coefficient	[cm ² /g]
	L =	material thickness	[cm]

Radiation Sources

Calculations of the mass attenuation coefficients, μ/ρ, for Clear-Pb[®] using Monte Carlo methods were performed for mono-energetic photons with energies ranging from 10 keV to 10 MeV. Clear-Pb[®] mass attenuation coefficients for neutrons were also determined for an energy range of 10 μeV to 10 MeV. Finally, μ/ρ was determined for ²⁵²Cf photon and neutron spectra. Prompt and delayed ²⁵²Cf photons were input as a multi-group source, while the neutron energy spectrum was modeled as a Maxwellian spectrum.

Statistics

The total number of particles transported for each calculative run of mono-energetic photons, neutrons, ²⁵²Cf photons or neutrons, sample material, or sample thicknesses were

determined such that the difference in the number of incident particles versus transmitted particles (net flux) was always greater than 10^5 , and was typically greater than 10^7 . The total number of particles ranged from 10^6 to 10^{12} for each run depending on the thickness of the sample and source emission energy, this was necessary so as to have statistically significant results.^{98,99} The MCNP relative error (1σ) was related to the inverse square root of the net flux.¹

C. Results and Discussion

In Figures 2 and 3 are presented the calculated photon and neutron μ/ρ as determined from Monte Carlo calculations of transmission through Clear-Pb[®] and plain acrylic. As the incident particles were mono-energetic, these results were not a function of material thickness. From Figure 3, the constant ratio of neutron μ/ρ between Clear-Pb[®] and plain acrylic is 1.36, similar to the 1.38 predicted value. This value and independence of the ratio on neutron energy was expected as the majority of kerma was released through elastic scattering on hydrogen where the elastic scattering process at these energies may be ascribed through non-relativistic kinematics. In contrast, the μ/ρ ratio for photon emissions varied as a function of energy as the impact of the photoelectric effect by lead in the Clear-Pb[®] was energy dependent. This was more obvious upon examination of the Clear-Pb[®] and plain acrylic μ/ρ at photon energies near the lead K-edge. Unlike the mono-energetic radiation sources, that from ²⁵²Cf is poly-energetic and energy discrimination as used in the mono-energetic sources was not possible. Illustrations of ²⁵²Cf photon and neutron μ/ρ are presented in Figure 4. Where the suffixes N and G after acrylic and Clear-Pb[®] are used to denoted radiation from ²⁵²Cf neutron and photon sources, respectively. From these two figures, it is clear that μ/ρ decreased for increasing

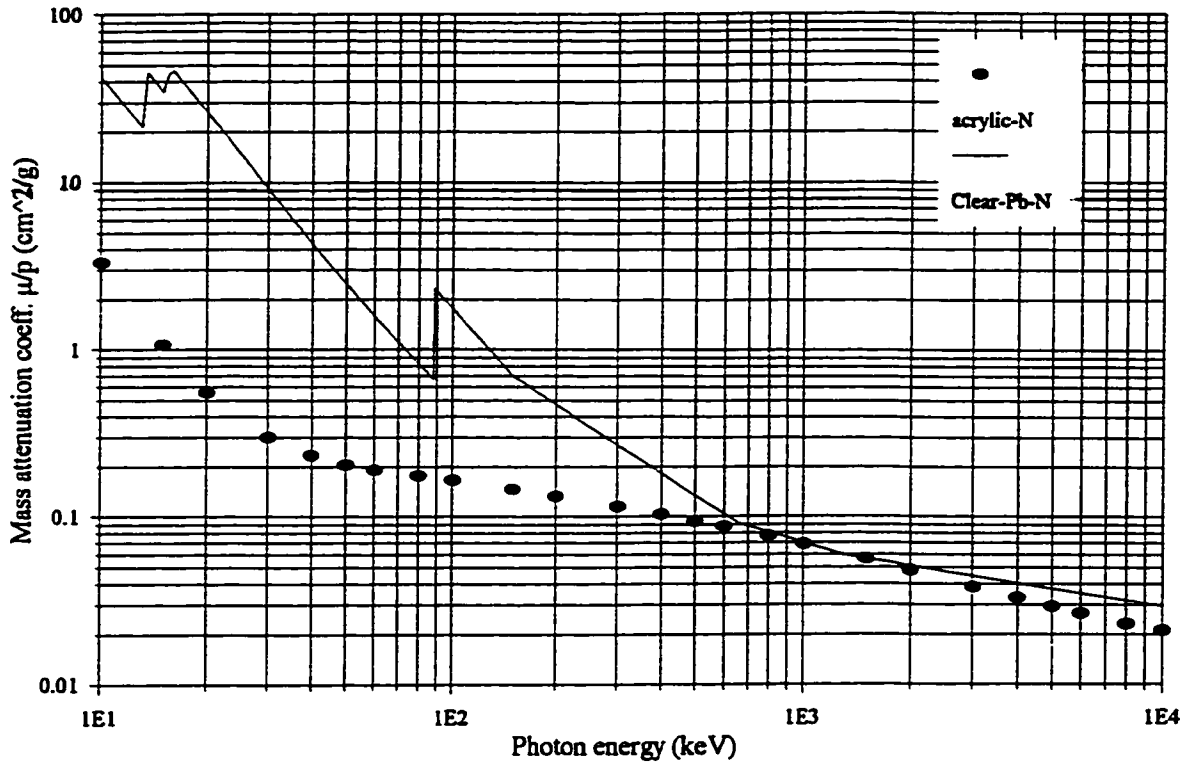


Figure 2. Calculated Clear-Pb[®] and plain acrylic photon μ/ρ .

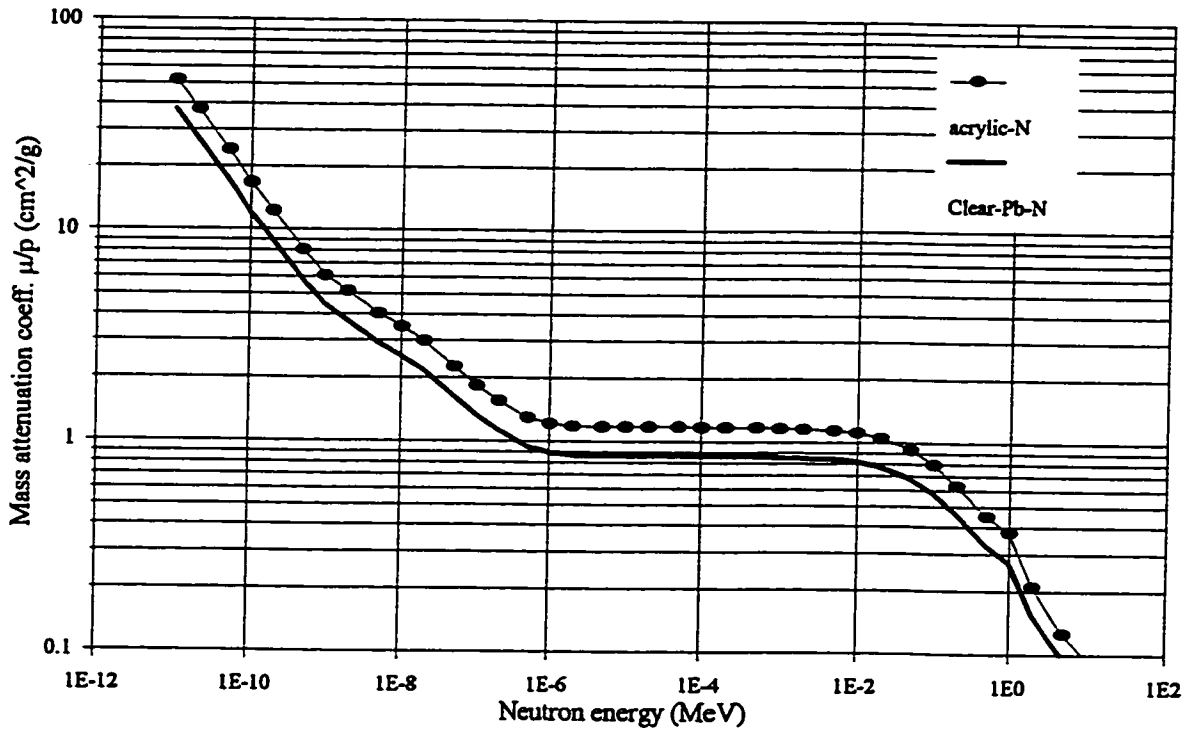


Figure 3. Calculated Clear-Pb[®] and plain acrylic neutron μ/ρ .

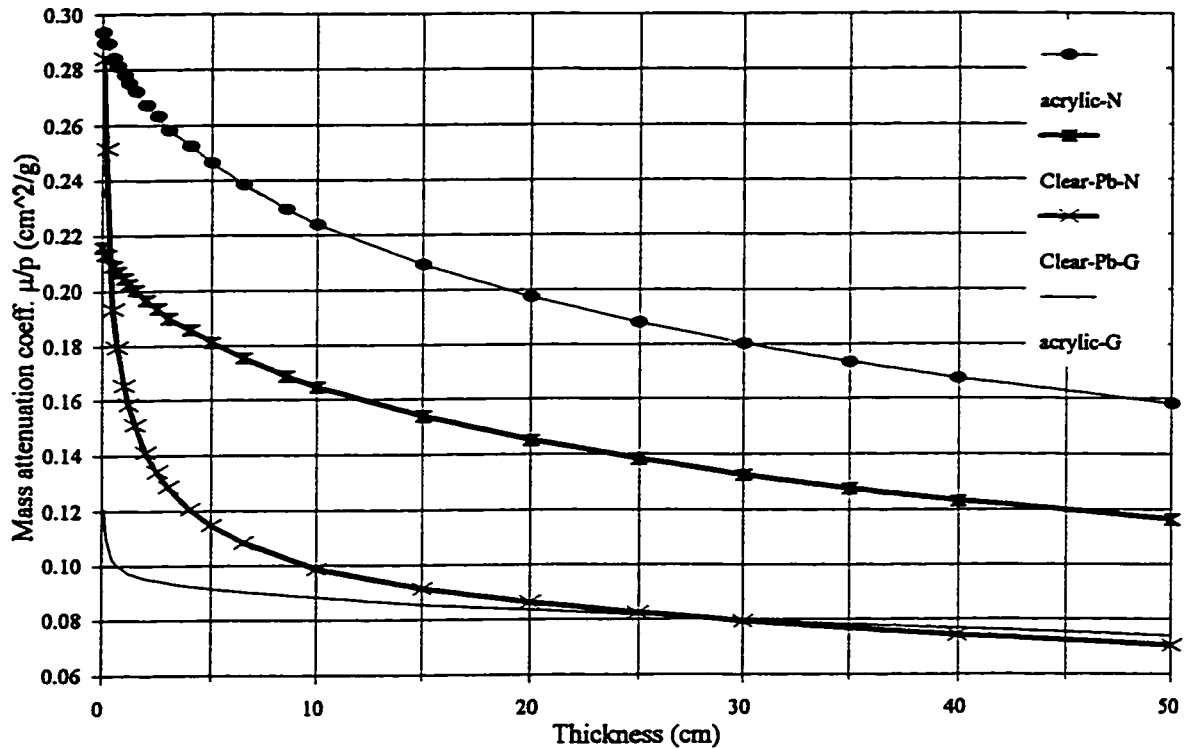


Figure 4. Calculated μ/ρ for ^{252}Cf photons and neutrons.

material thicknesses. It is apparent from Figure 4 that the ^{252}Cf photons are more penetrating than their neutron counterpart. Here, marked beam hardening is observed within the first 10 cm for both Clear-Pb[®] and plain acrylic.

Comparison with Nuclear Associates

A comparison of results for photon μ/ρ for Clear-Pb[®] was made between those determined calculatively herein and those determined experimentally by Nuclear Associates.⁹⁶ These photon sources were ^{137}Cs , ^{60}Co , 43.0 keV, and 68.8 keV and the results are presented in Table 2. For ^{137}Cs and ^{60}Co , their results were 0.0948 cm^2/g and 0.0646 cm^2/g , respectively, while μ/ρ determined using MCNP was 0.0907 cm^2/g for ^{137}Cs and 0.0629 cm^2/g and 0.0583 cm^2/g for 1173 and 1332 keV from ^{60}Co , respectively. The ratio of calculative to experimental μ/ρ for ^{137}Cs was 0.96. For ^{60}Co , the calculated

photon abundance weighted μ/ρ was $0.0606 \text{ cm}^2/\text{g}$ which gave a ratio of calculative to experimental μ/ρ for ^{60}Co of 0.94.

The Nuclear Associates¹⁴ μ/ρ results were determined experimentally at 43.0 keV and 68.8 keV which were the average photon energies for diagnostic photon beams. The ratio of the Monte Carlo calculative results for mono-energetic photons to those measured μ/ρ results yield ratios of 1.13 and 0.96 at photon energies of 43.0 keV and 68.8 keV, respectively. As discussed later in the error analysis, this level of agreement (9%) between the calculative model and experimental measurements, was not surprising.

Table 2. Comparison of mass attenuation coefficients for Clear-Pb[®].

photon source	MCNP μ/ρ (cm^2/g)	Nuclear Associates μ/ρ (cm^2/g)
^{137}Cs	0.0907	0.0948
^{60}Co	0.0606	0.0646
43.0 keV	3.62	3.19
68.8 keV	1.151	1.20

Comparison with Hubbell and Seltzer

As an independent check of the methodology employed herein, comparisons of μ/ρ results were made for mono-energetic photons obtained using MCNP with coefficients derived from a combination of elemental mass attenuation coefficients based on measured data tabulated by Hubbell and Seltzer.⁹⁷ Here, the mass attenuation coefficients for Clear-Pb[®] and acrylic were derived by using the mass weighted sum of each individual element as listed in Table 1 and the elemental mass attenuation coefficients as tabulated by Hubbell and Seltzer.⁹⁷ The ratio of MCNP calculated results for Clear-Pb[®] to those determined by Hubbell and Seltzer⁹⁷ are presented in Figure 5 where H & S is used to denoted results from the these authors. Validity of Monte Carlo results was supported by agreement, an average of 0.032% and 0.016% for Clear-Pb[®] and acrylic, respectively, with $1 \sigma = 0.26\%$,

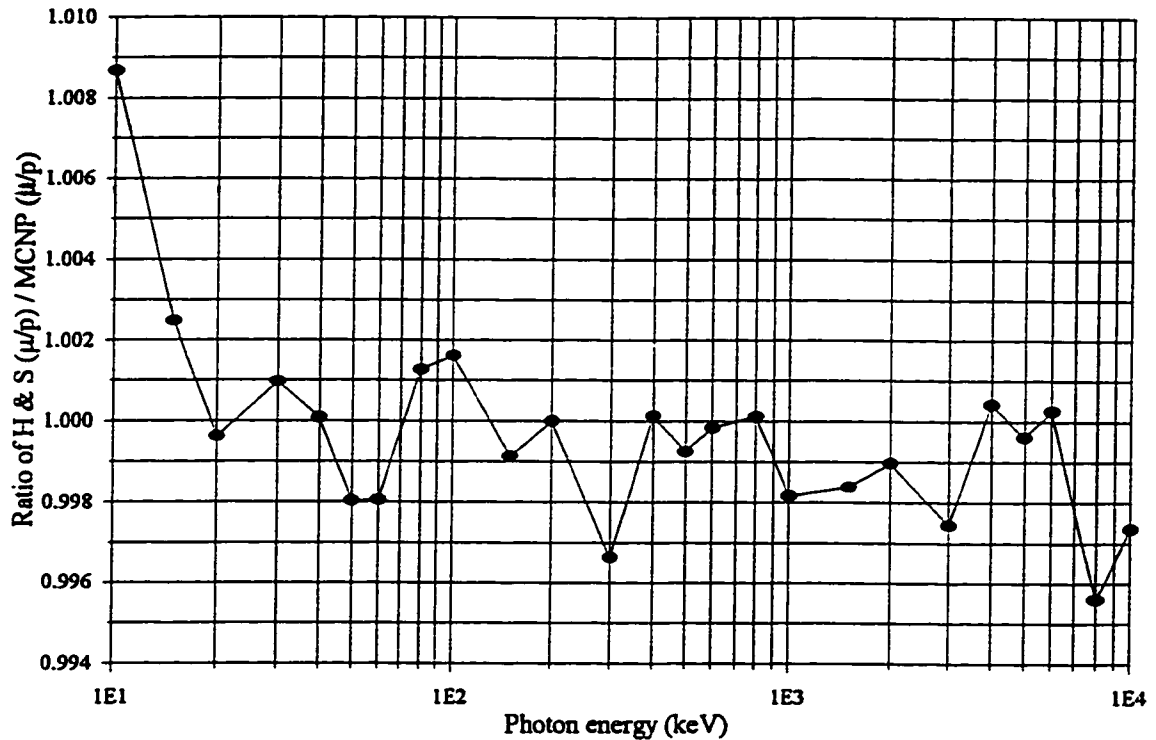


Figure 5. Comparison of Hubbell and Seltzer data with MCNP results.

for μ/p common to MCNP and those of Hubbell and Seltzer.⁹⁷ This level of agreement was not surprising as the photon cross-section data for the materials studied (H, C, O, Pb) are well established and have not varied significantly in recent years.¹⁰⁰

Error Analysis

As with all calculative models, there were inherent limitations in the approach. An analysis of relevant statistical and systematic errors produced through the calculative methodology used for this study follow:

1. The relative errors (1σ) as determined from Monte Carlo calculations obtained through net particle flux were kept at less than 0.1%. Consequently, the accuracy of the calculative μ/p results were not statistically limited.
2. Uncertainties, including impurities, in the elemental and mass composition of

Clear-Pb[®] were not given, but are assumed to be 0.003 g/cm³ or approximately 0.1% of the total mass density. While estimation of the change in μ/ρ for Clear-Pb[®] for a lead loading of 0.480 ± 0.003 g/cm³ was energy dependent, this variation in material composition gave an average variation of μ/ρ of less than 1%.

3. Results of diagnostic energy μ/ρ for Clear-Pb[®] were obtained by Nuclear Associates with a poly-energetic photon source, results obtained herein employed mono-energetic photons. Consequently, accuracy of the diagnostic effective energies stated by Clear-Pb[®] would limit the comparison. Assuming μ/ρ values obtained by Nuclear Associates⁹⁶ were accurate, the correct effective energies, as determined from MCNP, were 40 and 50 keV, not the stated 43.0 and 68.8 keV
4. If the good geometry was improperly accepting scattered photons, then the resulting transmission ratio (N_o/N) would be greater and would provide an artificially low value for μ/ρ . This was not the case as comparison of mono-energetic μ/ρ results obtained with MCNP and those of Hubbell and Seltzer⁹⁷ were in agreement within 0.2% from 10 keV to 10 MeV, and accurately depicted the lead K- and L-edges, thus confirming the accuracy of calculated results.

Results obtained herein were derived only for good geometry without room scatter.

Therefore, these values may not be directly employed for shielding calculations. However, results of this study and comparisons of μ/ρ with Clear-Pb[®] and acrylic provide a relative assessment of the utility of Clear-Pb[®] as a radiation shielding material as compared to plain acrylic and other characterized materials.

C. Practical Comparison and Experimental Measurements

For the clinical application at hand within the ²⁵²Cf neutron therapy suite, a direct

comparison of the Clear-Pb[®] and plain acrylic μ/ρ for photons and neutrons through 30 cm is of interest to determine radiation transmission and attenuation through these two materials. In this case, only the linear attenuation coefficients, μ , for each material and radiation type are of interest. Here, the μ for ²⁵²Cf photons through 30 cm of Clear-Pb[®] and plain acrylic was 0.1268 cm⁻¹ and 0.09496 cm⁻¹, respectively. For ²⁵²Cf neutrons, the μ through 30 cm of Clear-Pb[®] and plain acrylic was 0.2122 cm⁻¹ and 0.2145 cm⁻¹, respectively. With Equation 1, the transmission of ²⁵²Cf photon emissions through 30 cm of Clear-Pb[®] and plain acrylic was calculated to be 5.79% and 2.23%, respectively, while the transmission for the neutron emissions was calculated to be 0.160% and 0.172%, respectively. Thus, the ratio of the transmissions for ²⁵²Cf photons and neutrons between Clear-Pb[®] and plain acrylic was 2.60 and 0.932, respectively. As expected due to the presence of lead, the Clear-Pb[®] was a superior radiation shielding material for ²⁵²Cf photons, but was inferior for ²⁵²Cf neutrons due to its lower hydrogen mass loading.

Calculations for narrow-beam geometry mass attenuation coefficients, μ/ρ , were determined instead of broad-beam geometry mass attenuation coefficients, μ'/ρ , the direct applicability of these results are in question. However, it may be expected that the ratios of values obtained herein, such as for comparisons between Clear-Pb[®] and plain acrylic, may be applicable in practical shielding analyses where room scatter is negligible.

D. Alternative Shielding Materials

Plain acrylic was a superior radiation shielding material compared to Clear-Pb[®] for ²⁵²Cf as determined using Monte Carlo methods. This was due primarily to the increased mass density of hydrogen, as the majority of absorbed dose emitted by ²⁵²Cf is by neutrons, and considering the increased relative biological effectiveness of these neutrons in comparison

to photon radiation. However, other materials with higher hydrogen loadings may be developed. Polyethylene has an even larger hydrogen mass density, 0.135 g/cm^3 , than acrylic, 0.096 g/cm^3 . A lead-doped polyethylene material would provide enhanced photon shielding, and addition of materials with high thermal neutron cross-sections such as ^{10}B or ^{157}Gd would attenuate the thermal neutron component. While these alternatives were not explored herein, any meaningful radiological studies should be accompanied by a cost effectiveness analysis as well as consideration of other important factors such as optical transparency and longevity.

E. Conclusion

It was determined that the utility of Clear-Pb[®] as a photon radiation shielding material, in comparison to plain acrylic was greatest for all photon energies, especially those less than 150 keV such as for shielding applications for diagnostic radiology. These results were determined through calculations of the mass attenuation coefficients for both materials over an energy range from 10 keV to 10 MeV. In comparison with the μ/ρ results obtained experimentally for ^{137}Cs and ^{60}Co by Nuclear Associates,⁹⁶ those determined calculatively herein were in good agreement, and were -4% less. Comparison of μ/ρ results over photon energies ranging from 10 keV to 10 MeV as tabulated by Hubbell and Seltzer⁹⁷ with those determined calculatively herein were in good agreement, and were on average -0.2% less. Furthermore, the enhanced utility of Clear-Pb[®] as a radiation shielding material for ^{252}Cf photons was demonstrated. Here, a decrease in transmission by a factor of 2.6 was determined for a 30 cm thick shield. As the majority of absorbed dose emitted by ^{252}Cf is by neutrons, and considering the increased relative biological effectiveness of these neutrons in comparison to photon radiation, it was found that Clear-

Pb[®] was not an adequate substitute for plain acrylic as a radiation shielding material for ²⁵²Cf manually afterloaded brachytherapy implants. Here, the transmission of ²⁵²Cf neutrons was calculated to be 7% greater for Clear-Pb[®] than for plain acrylic using a shield thickness of 30 cm. This elevation of transmission was due to the decrease in hydrogen content of the Clear-Pb[®] in comparison to plain acrylic.

III. PERSONNEL EXPOSURE FROM ²⁵²Cf

A. Introduction

²⁵²Cf sources have been used for clinical and scientific purposes at WSU for over three years. In that time, 27 patients and 162 implants were performed primarily by two physicists and physicians. No accurate conclusions may be drawn between the personnel exposure records and the number of implants performed. This was the case as those that regularly donned their badges received additional exposure from other activities. As a means to determine an approximate personnel exposure rate for personnel involved with clinical implants using ²⁵²Cf sources, health physics experiments using personnel badges and superheated bubble detectors were performed.

B. Materials and Methods

The purpose of these endeavors is to determine the dose-equivalent (H or Deq) per clinical source handling per unit source strength to two personnel sites. These sites are the whole body and an extremity, typically the right hand. To ascertain the exposure one would receive at each site, personnel badges specific to each site were used.

Personnel Badges

For the whole body Deq, two types of badges, Landauer types I and Y, are commonly employed for personnel monitoring. The I type has a cadmium box which contains two

thermoluminescent dosimeters (TLDs) and a polycarbonate track-etch dosimeter film to detect fast neutrons over the 0.144 to 10 MeV energy range. The TLDs in the I type are TLD-100 and TLD-700. Consequently, the I type is sensitive to photons and fast neutrons. Like the I type, the Y type is also worn at the waist for monitoring of whole body radiation. The film detector in a Y type badge is primarily used to detect low LET radiation, but also has a partial cadmium shield to discern between fast and albedo thermal neutrons. The type G whole body badge is identical to the Y type, except that no partial cadmium shield is present, thus it is sensitive to only low LET radiation. For extremity monitoring, Landauer type C badges are used. These badges fit upon the wrist and are used in place of ring badges (type U) as the recorded extremity exposure from the type C badge would be additive to that of the ring badge and would misrepresent the actual extremity Deq. The type C is comprised of a single polycarbonate track-etch dosimeter film used to detect fast neutrons.

Bubble Detectors

Superheated bubble detectors (Neutrometer™) were used to validate the neutron Deq determined by the personnel monitor badges. Their active volume was approximately 1.0 cm³ (0.5 cm diameter, 5.0 cm long). A unique merit of the bubble detector is that exposure results may be determined immediately following the irradiation, it has a relatively high sensitivity of 0.46 bubbles per μSv , up to a maximum of 200 μSv , and is reusable for additional studies.

Methodology

Inside the ²⁵²Cf Suite, the I, C, and Y type badges and a single bubble detector were separately irradiated on the large surface of a 15 x 62 x 125 cm³ acrylic block to mimic a

human phantom. Twelve ^{252}Cf AT sources of 11.35 μg each (136.2 μg total) were placed in a catheter at a distance of 50 cm for a fixed amount of time. The TLDs were irradiated for 5 hours. TLDs were set in a low-radiation environment, and sent to Landauer to be readout instead of being readout locally as this best duplicated the actual personnel monitoring procedure. A single bubble detector was irradiated for 30 seconds three times the same day to test reproducibility. Following the irradiation, the number of bubbles in each bubble detector were recorded. Two additional bubble detectors were irradiated in the same geometry and for the same time to check batch uniformity. The bubble detector was irradiated for a shorter time than the TLDs due to its lower maximum exposure level and higher sensitivity. A time-motion study was performed to determine the time, distance, and shielding parameters that a ^{252}Cf radiation worker would experience upon loading or unloading a catheter from a patient. The time to transfer a loaded catheter from the patient to the ^{252}Cf Safe, or visa versa, was determined, as was the source to personnel distance and shielding employed was also noted. These parameters, e.g., time, distance, and shielding, were used in the derivation of Deq per clinical source handling per unit source strength to the two personnel sites, whole body and extremity.

C. Results and Discussion

Bubble readings after 30 seconds at 50 cm using 136.2 μg of ^{252}Cf were: 68, 71, 74, 77, 81; the average bubble production was 74.2 ± 5.1 bubbles. The average Deq rate for the five measurements was 1.42 ± 0.1 $\mu\text{Sv}/\mu\text{g}\cdot\text{h}$ at a distance of 50 cm.

Results from personnel badges were obtained from Landauer a month following the irradiation. These are presented in Table 3 where it is evident that there was good (4%) uniformity among the responses from the three paired badges. Furthermore, the

ratio of neutron to photon Deq was 16.0 ± 0.2 as calculated from the C type badges and taking the ratio of types I and G badges. However, the variance of the neutron and photon doses among the first nine badges was 11% and 9%, respectively. Here the ring TLD (type U) was excluded as its TLD-100 chip over-responded by a factor of 4 (1390/342) to backscattered thermal neutrons as shown in Table 3. Consequently, the TLD ring should not be worn while working with ^{252}Cf . Additionally, the TLD ring should not be worn accompanying the C type wrist badge as Landauer will add their exposures yielding an excessive extremity dose.

Table 3. Personnel badge results after a 5 hour exposure to $136.2 \mu\text{g } ^{252}\text{Cf}$.

badge	neutron (mSv)	photon (mSv)	total (mSv)
Y WAIST	0	35.0	35.0
G WAIST 1	0	31.0	31.0
G WAIST 2	0	32.0	32.0
AVG. G	0	31.5	31.5
I WAIST 1	497	0	497
I WAIST 2	499	0	499
AVG. I	498	0	498
C WRIST 1	569	34.0	603
C WRIST 2	620	39.0	659
AVG. C	595	36.5	632
U RING	0	139	139

From these measured Deq, the neutron and photon Deq rate was 0.80 and 0.05 $\mu\text{Sv}/\mu\text{g-h}$, respectively. Landauer uses a neutron quality factor (Q) of 10 to relate rad to rem. Accounting for Q, the ratio of neutron dose to total dose is 61%. While there do not appear to be any references in the literature regarding albedo dosimetry of ^{252}Cf , the measured ratio of neutron dose to total (61%) as determined by using TLDs, and dividing out Q, was in good agreement (5%) with that published by Yanch and Zamenhof⁶⁸ where

the a ratio of 66% was observed at a distance of 1 cm in a water phantom. At this close distance, the contribution of scatter to total (primary plus scatter) is minimal and may approximate that of the albedo system studied with TLDs. This is good agreement seen as further justification of the relative responses produced by the personnel badges.

The bubble detectors were used as a separate means to determine the neutron Deq component. A comparison of the absolute neutron Deq rate at 50 cm as determined using the bubble detectors (1.42 $\mu\text{Sv}/\mu\text{g-h}$) versus that obtained using the personnel badges (0.80 $\mu\text{Sv}/\mu\text{g-h}$) gave results which differed by a factor of 1.78. However, this discrepancy became clear after contacting both companies. Landauer uses a neutron quality factor of 10 as recommended by 10 CFR 20, while the radiation weighting factor for the Victoreen bubble detector closely follows that as recommended by ICRP 60.¹⁰¹ When convolving the ^{252}Cf spectrum, using a Maxwellian model, with the radiation weighting factors of ICRP 60,¹⁰¹ one obtains an average radiation weighting factor of approximately 15.4. When accounting for the differences in quality and radiation weighting factors between both companies, the neutron Deq rates were in relatively good, 13%, agreement. In summary, the total Deq rate as measured using personnel badges at 50 cm was 0.85 $\mu\text{Sv}/\mu\text{g-h}$ with 94% attributed to neutron Deq. However, this estimate may be low by a factor of approximately 1.5 due to the outdated 10 CFR 20 quality factor for neutrons as used by Landauer.

Time-Motion Study for ^{252}Cf Personnel Exposure

Due to variation in the speed of individuals to perform manually afterloading, estimates were made to determine the time spent per implant. Here, an estimate of 30 seconds for whole body and extremity exposure for source transfer and patient loading was

determined. Average torso and extremity distances of 70 and 20 cm from the sources were derived. In this case, no shielding was assumed. For the implant preparation phase (source tube loading, labeling, etc.) an additional 30 seconds was assumed with a source extremity distance of 15 cm and an average torso distance of 80 cm. Here, a 50% shielding factor was also included. Using the inverse square law, the estimated total extremity Deq for source transfer and implant preparation was $0.044 \mu\text{Sv}/\mu\text{g}$ and $0.080 \mu\text{Sv}/\mu\text{g}$, respectively. For the whole body Deq, values of $0.0036 \mu\text{Sv}/\mu\text{g}$ and $0.0014 \mu\text{Sv}/\mu\text{g}$ were calculated for source transfer and implant preparation, respectively. For convenience, values of $0.0485 \mu\text{Sv}/\mu\text{g}$ and $0.0033 \mu\text{Sv}/\mu\text{g}$ for total Deq for the extremities and whole body, respectively, may be estimated from weighting the source transfer and implant preparation Deq rates by 7 to 1.

The maximum number of loadings one may perform a month may be determined for a busy institution where there may be 20 ^{252}Cf AT sources of $30 \mu\text{g}$ each where patients receive from 6 to 8 fractions per treatment but do not always need all 20 sources. As both implants and explants must be performed, the average number of source transfers may be set at 14 with one implant preparation per patient. If one sets the average number of sources at 10, then $300 \mu\text{g}$ is the operative ^{252}Cf source strength. If one person had to perform all the implants and explants with no assistance, then the total whole body and extremity Deq would be 15.5 and $209 \mu\text{Sv}$, respectively. If an ALARA level (III) of 30% of the federally mandated Deq limits was established with 0.5 mSv to the whole body and 5 mSv to extremities, then the annual whole body limit would be surpassed before the 10th patient while the extremity limit would be surpassed before the 8th patient and would constrain the limit of ^{252}Cf implant activity by the radiation worker.

Though a retrospective analysis of personnel exposure was not possible due to badges either not being worn or inclusion of exposure from other sources, in no case did any of the personnel working with ^{252}Cf register quarterly or annual Deq greater than the ALARA levels of the department. For all involved with ^{252}Cf , the maximum monthly whole body and extremity Deq were $27\ \mu\text{Sv}$ and $145\ \mu\text{Sv}$, respectively.

D. Radiation Safety Survey

In addition to monitoring those personnel that regularly handled ^{252}Cf sources, the Deq rate outside the ^{252}Cf Suite had to be determined immediately following receipt of 13 ORNL-made ^{252}Cf AT sources. Here, six locations were determined to be of radiological interest. These were immediately outside the ^{252}Cf Suite door, at the ^{252}Cf Suite desk area, within the ^{60}Co total body irradiation (TBI) Suite, in the main departmental corridor, at the foot of the emergency exit stairwell, and above the ^{252}Cf Suite on the grassy lawn where the last three locations are not radiologically controlled areas. Two surveys were performed to determine the Deq rates at the six locations. The first survey was for the case where all 25 AT sources, $430\ \mu\text{g}\ ^{252}\text{Cf}$, were inserted into the paraffin ^{252}Cf Safe. Here, a RAD-REM Snoopy NP-2 meter was used to survey neutron Deq rates while a Victoreen model #498 ion chamber was used to survey photon Deq rates. In the first survey, both photon and neutron Deq rates were less than $0.01\ \mu\text{Sv/h}$ at all six locations. In the second survey with the sources placed atop a styrofoam stand in the middle of the ^{252}Cf Suite, both the neutron and photon Deq rates were significantly larger, and are presented in Table 4. The total, neutron plus photon, Deq rate in the main corridor exceeded the maximum permissible uncontrolled Deq hourly rate. The total Deq rates for all other locations were within the maximum permissible rates. To satisfy NRC

Table 4. Dose-equivalent rates ($\mu\text{Sv/h}$) outside the ^{252}Cf Suite.

radiation	door	desk	TBI	main corridor	stairwell	lawn
neutron	1.4	0.37	<0.01	0.24	0.12	<0.01
photon	0.18	0.09	<0.01	0.13	0.035	<0.01
total	1.58	0.46	<0.02	0.37	0.155	<0.02

regulations regarding the main corridor hourly Deq rate, actions were decided upon with the WSU ROC Physics Coordinator. Here, additional shielding shall be used for experiments when all ^{252}Cf sources are removed from the safe. When performing clinical implants, room surveys including the main corridor are to be performed to demonstrate that the uncontrolled maximum Deq hourly rate is not exceeded; shielding by the patient may significantly diminish the main corridor Deq rate. As the ^{252}Cf sources decay, the maximum hourly rate will diminish to the point where the uncontrolled maximum Deq hourly rate is not exceeded when all ^{252}Cf AT sources are in the center of the ^{252}Cf Suite. Using a 2.645 year half-life, this should occur in October 2002.

E. Conclusion

A rigorous retrospective analysis of personnel exposure was not possible due to lack of diligence in donning badges or inclusion of exposure from other sources. However, approximate factors of $0.050 \mu\text{Sv}/\mu\text{g}$ -handling and $0.0037 \mu\text{Sv}/\mu\text{g}$ -handling for the extremities and whole body, respectively, were determined to calculate personnel Deq rates when performing manual afterloading of ^{252}Cf AT sources. Based on a total source strength of $300 \mu\text{g}$ and 7 fractions, it was concluded that one person could not perform 8 ^{252}Cf implants per year. If four individuals were involved with ^{252}Cf manual implants, the maximum number of patients that could be treated is 28 per year. These results were based on the maximum ALARA level (III) commonly used within our department.

Therefore, development of an HDR remote afterloading device to facilitate ^{252}Cf implants is necessary to permit treatment of a significant number of patients. Additionally, a radiation survey of the ^{252}Cf Suite revealed excessive hourly Deq rates in the departmental main corridor. Actions were taken to satisfy the radiation safety regulations.

Consequently, the ^{252}Cf Suite with the 25 AT sources present is considered to be a radiologically safe environment. However, extensive clinical use of ^{252}Cf will be limited until development of an HDR remote afterloading device.

CHAPTER 8

FEASIBILITY OF A HIGH DOSE RATE ^{252}Cf SOURCE

I. INTRODUCTION

In this chapter, the feasibility of construction of an HDR neutron emitting ^{252}Cf source for clinical applications is examined along with potential improvements of individual processes along the ^{252}Cf source production pathway. At the Radiochemical Engineering Development Center (REDC) and the Californium Facility (CF) at ORNL, ^{252}Cf radiochemical yields were optimized through experiments involving chemical precipitations as a means to increase the ^{252}Cf specific source strength. Since the cost of a typical 5 mg ^{252}Cf precipitation is \$0.28 M, there is motivation to use chemical substitutes or stand-ins for ^{252}Cf , such as Tb, when performing these studies. Radioactive ^{249}Cf was used to chemically simulate ^{252}Cf and radiologically determine precipitation yields.

Mechanical tests using rolling and swaging techniques were performed which stressed test subjects with Cf stand-ins to their fatigue limits. As opposed to using actual californium, test subjects could be handled and tested in a radiologically uncontaminated environment. In addition to precipitates using Tb as a Cf stand-in, test pellets fabricated at the Transuranium Research Laboratory (TRL) at ORNL were also structurally tested. These pellets employed Gd as a stand-in for Cf for emulation of mechanical properties. Following analysis of radiochemistry and source metallurgy processes, source capsule integrity after ^{252}Cf alpha decay and subsequent helium buildup was modeled for a variety of proposed HDR sources. In this study, the ^{252}Cf source strength necessary for a clinical application of a ^{252}Cf HDR device may be assumed as 1 to 4 mg, with approximately 250 μg ^{252}Cf for an HDR prototype.

II. RADIOCHEMISTRY EXPERIMENTS

A. Background

In examining how to produce a ^{252}Cf source with a high specific source strength, one must first understand the current radiochemical techniques used in their fabrication.^{102,103} ^{252}Cf is created in nuclear reactors with extremely high thermal neutron fluxes. There are two such reactors in the world, one being the High Flux Isotope Reactor (HFIR) at ORNL. This reactor was built with the primary objective of producing ^{252}Cf and other transuranic radioisotopes, has a thermal neutron flux exceeding 10^{15} n/cm²-s, and has produced over 10 grams of ^{252}Cf as of press with annual production of approximately 300 mg. ^{252}Cf is generally made through successive neutron capture reactions upon a 120 gram CmO_2 target; the Cm was initially produced from ^{239}Pu and other materials as a result of nuclear recycling efforts.⁵⁵ Targets spend approximately 6 to 8 months in the HFIR core to optimize the ^{252}Cf yields and production of other radioisotopes such as ^{254}Es and ^{257}Fm . Upon removal from the reactor, Cf is chemically separated from the other elements using a combination of solvent extraction and ion exchange processes. Following initial partitioning, the ^{252}Cf is shipped via a pneumatic tube to the CF where additional stages of purification are accomplished with alpha-hydroxyisobutyric acid (AHIB) on a resin column.¹⁰⁴ Following final purification of the ^{252}Cf , the efforts described below were performed to demonstrate the potential for increased ^{252}Cf source specific activity for fabrication of an HDR source.¹⁰²

B. ^{252}Cf Radiochemistry Optimization Utilizing Chemical Stand-ins

The purpose of this study was to determine if the chemical procedures currently used at CF for source fabrication could be scaled-up to produce relatively high ^{252}Cf loadings in

preparation of HDR source fabrication.

Materials and Methods

Chemical precipitations were performed in the CF cold lab using solutions of 0.1 M stock oxalic acid ($\text{H}_2\text{C}_2\text{O}_4$), stock hydrazine hydrate (85% $\text{N}_2\text{H}_4 \cdot \text{H}_2\text{O}$), stock (100 mg Pd/ml) palladium tetrammine dinitrate ($\text{Pd}(\text{NH}_3)_4(\text{NO}_3)_2$), and AHIB ($\text{C}_4\text{H}_8\text{O}_3$). The parameters examined were the Tb ion concentration present in the AHIB solution, and the volumes of oxalic acid and hydrazine necessary for performing the precipitation. In this study, precipitations using Tb ranged from 2 to 150 mg ^{252}Cf -eq, and were performed to demonstrate the potential for increased specific ^{252}Cf source strengths necessary for fabrication of an HDR source. The oxalic acid volumes used ranged from 0.7 to 5.0 ml while the hydrazine volume ranged from 0.5 to 5.0 ml. Typical ^{252}Cf precipitations in the CF hot cells utilize 3 ml each of these solutions, 6.5 ml of 100 mg Pd/ml solution, and 10 ml of 500 μg ^{252}Cf /ml in 0.5 M AHIB solution. Specific ^{252}Cf source loadings performed at ORNL for routine source fabrication are typically less than 0.07 mg ^{252}Cf per /mm³ of a ceramic-metal (cermet) wire.^{102,105} The manner in which the ^{252}Cf -eq mass was determined from the known mass of Tb is presented in Equation 1 where an 80% ^{252}Cf isotopic fraction (f) was assumed. A factor of 1.26, i.e. $251 \times 80\% / 158.9$, was used to relate the Tb mass to the ^{252}Cf -eq mass.

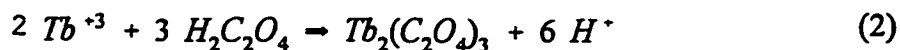
$$M_{\text{Cf-252-eq}} = M_{\text{Tb}} \left(\frac{A_{\text{Cf}}}{A_{\text{Tb}}} \right) f_{\text{Cf-252}} \quad (1)$$

where:

$M_{\text{Cf-252-eq}}$	= ^{252}Cf -eq mass used for hot-cell comparisons	[mg]
M_{Tb}	= Tb mass used in cold lab study	[mg]
A_{Cf}	= average Cf atomic mass	[amu/atom]
A_{Tb}	= Tb atomic mass	[amu/atom]
$f_{\text{Cf-252}}$	= ^{252}Cf isotopic fraction of total Cf present	[dimensionless]

AHIB was placed in a 50 ml test tube, kept in a 60°C water bath, and sparged with Ar gas at 0.2 ft³/h. The oxalic acid was added dropwise to precipitate the terbium as terbium oxalate, Tb₂(C₂O₄)₃. Ultra-pure H₂O was used throughout each step to rinse the added liquids down the sides of the test tube. After sparging for 10 minutes, the hydrazine was added dropwise and the Pd solution added immediately afterwards. In general, precipitations with 650 mg of Pd were performed. The Ar was allowed to bubble through the solution for ten minutes, forcing intimate contact between the terbium oxalate and the palladium precipitate. Upon washing of the precipitate and extraction of the liquid supernate, the precipitate is dried in an oven to produce a ²⁵²Cf-equivalent (²⁵²Cf-eq) product in solid form and the radiochemistry efforts are complete, after which machining techniques such as rolling and swaging are used to form the ²⁵²Cf-eq product into an encapsulable wire and are discussed in the next section.

The maximum ²⁵²Cf-eq precipitate yield for a given ²⁵²Cf-eq loading was obtained after determination of the optimum oxalic acid and hydrazine necessary for precipitation of Cf oxalate coated with palladium metal. It is not known if this method was previously performed in the early 1970's as documentation regarding the specific optimization of these parameters was not available.^{104,106} The concentration of Tb stand-in ranged from 0.5 to 5 mg ²⁵²Cf-eq/ml in a solution of 0.35 M HNO₃ in 0.5 M AHIB. Therefore, a 20 mg ²⁵²Cf-eq precipitation with 2 mg ²⁵²Cf-eq/ml would require 10 ml of solution. The number of moles of oxalic acid necessary to produce terbium oxalate may be determined (Equation 2) from stoichiometry.¹⁰⁷



For a 100 μ-mole sample of terbium, one would expect a minimum of 150 μ-moles of

oxalic acid necessary for precipitation of terbium oxalate. At 0.1 M oxalic acid, a volume of 1.5 ml would precipitate the terbium. However, not all the oxalate ions will separate and couple with the terbium. Similar to the oxalic acid, the precise amount of hydrazine for optimal precipitation of Pd under laboratory conditions was also determined experimentally.

Results and Discussion

Following many precipitations, four semi-quantitative trends were observed which bounded the optimal oxalic acid and hydrazine volumes at 2 ml each.

- hydrazine \leq 1.5 ml made a temporary metallic Pd coating on the test tube
- hydrazine \geq 3.0 ml was increasingly effervescent and disturbed precipitation
- oxalic acid \leq 1.0 ml produced an oil surface which inhibited precipitation
- oxalic acid \geq 2.5 ml produced increasingly larger precipitation particulate size

These trends were determined visually for a variety of Tb precipitations; however the amount of oxalic acid necessary for adequate precipitation of the 50 and 150 mg ^{252}Cf -eq studies was approximately 5 ml. In these two precipitations, the Tb concentration ranged was 5 mg ^{252}Cf -eq/ml in a solution of 0.35 M HNO_3 in 0.5 M AHIB. In this study the AHIB concentration was fixed at 0.5 M, while Cf hot cell concentrations may range from 0.1 to 0.5 M. Consequently, the optimal hot cell volumes of oxalic acid and hydrazine may vary from the previously stated values. For existing hot cell practices, the total solution volume should be less than 40 ml. Either the AHIB ^{252}Cf concentration (mg/ml) must be increased or the relative volumes of each precipitation constituent must be decreased to not overflow the quartz tube during precipitation and sparging.

During calcining at 500°C followed by melting at 1600°C, the Tb oxalate was converted into Tb_2O_3 within the Pd metal matrix to form the cermet. With an active

source density of 12 g/cm³ due to the high proportion of Pd metal, the specific ²⁵²Cf-eq source strength was obtainable, and ranged from approximately 0.04 to 2.25 mg/mm³ for the 150 mg ²⁵²Cf-eq precipitation. Since some uncertainty exists in the actual precipitation yield, especially for highest ²⁵²Cf-eq loadings, further experiments are warranted.

C. Evaluation of Precipitation Yields Using ²⁴⁹Cf

The purpose of this next section was to measure the precipitation yield efficiency by placing small amounts of ²⁴⁹Cf in addition to the terbium in the HNO₃ and AHIB solutions.¹⁰⁸ The goal here was to demonstrate minimal ²⁴⁹Cf losses using the new proportions of oxalic acid and hydrazine. Three separate precipitations using ²⁴⁹Cf were performed in an REDC hot lab. The purpose of the third precipitation was to act as the standard for optimal precipitation while the first two precipitations were used to determine the impact of certain chemical components on the precipitation yield.

Materials and Methods

In the same manner as performed in the previous section, precipitations were conducted using Tb-loaded HNO₃, and stock solutions of Pd, 2 ml oxalic acid, and 2 ml hydrazine. Table 1 lists the chemicals and the amounts used for each precipitation. Accuracy of the ²⁴⁹Cf concentration was about 5% due to volumetric uncertainties.¹⁰⁹ The 0.20 and 0.60 μCi of ²⁴⁹Cf represented 0.049 and 0.147 μg of ²⁵²Cf-eq, and thus did not directly relate to heavily-loaded precipitations; however, the high Tb loading (10 mg ²⁵²Cf-eq in 17 mg Pd) was significant for HDR source chemistry. Though 100% conversion of ²⁴⁹Cf to the precipitate is desired, some ²⁴⁹Cf will be present in the supernate in a recoverable form. For zero losses, the sum of ²⁴⁹Cf in the precipitate and supernate should equate to that initially added.

Table 1. Precipitation of ^{249}Cf and chemical volumes.

chemical	precipitation #1 (ml)	precipitation #2 (ml)	precipitation #3 (ml)
$\text{Pd}(\text{NH}_3)_4(\text{NO}_3)_2$	0.17	0.17	0.17
$\text{N}_2\text{H}_4 \cdot \text{H}_2\text{O}$	2.00	2.00	2.00
$\text{H}_2\text{C}_2\text{O}_4$ (0.1 M)	2.00	2.00	2.00
HNO_3 (0.35 M)	20.0	0.00	0.00
HNO_3 (0.35 M) + AHIB (0.5 M)	0.00	20.0	20.0
^{249}Cf (10 $\mu\text{Ci/ml}$)	0.020	0.020	0.060

Results and Discussion

After completion of the chemistry procedures, the precipitates and supernates were dried using a heat lamp and dissolved in a 0.1 M solution of HNO_3 . Ten ml aliquots of the precipitates and supernates were taken to the CF Counting Lab to assay the ^{249}Cf with a high purity germanium detector; accuracy of the assays are $\pm 2\%$.^{108,109} The resulting yields are presented in Table 2. Differences between the total final activities and the initial activities were within the experimental uncertainties. Here, the initial activities were known to $\pm 5\%$ while the precipitate and supernate activities were both determined to $\pm 2\%$. However, it was reported that supernates #1 and #2 may have had small amounts of precipitate particulate entrained in solution, consequently increasing their activities.^{108,109} Whether or not this was the case was unclear due to propagation of uncertainties in ^{249}Cf activity assay. The yields of $\sim 95\%$ for precipitations #2 and #3 employing 0.35 M HNO_3 and 0.35 M HNO_3 in 0.5 M AHIB solutions were similar to those expected from previous radiochemical procedures.¹¹⁰ The lower precipitation yield of 83% for the 0.35 M HNO_3 solution was explained by the lack of AHIB which is used in cell in the ^{252}Cf solutions.

Table 2. Precipitation yields using a ^{249}Cf radiotracer.

precipitation #	initial activity (μCi)	precipitation activity / yield ($\mu\text{Ci} / \%$)	supernate activity / yield ($\mu\text{Ci} / \%$)	total final activity / yield ($\mu\text{Ci} / \%$)
1	0.20 ± 0.01	0.169 / 83.4	0.0226 / 11.3	0.1916 / 95.8
2	0.20 ± 0.01	0.192 / 95.0	0.0102 / 5.1	0.2022 / 101.1
3	0.60 ± 0.03	0.573 / 95.5	0.0377 / 6.3	0.6107 / 101.8

D. Conclusion

Studies of ORNL radiochemical procedures were performed. Oxalic acid and hydrazine solution volumes were varied in conjunction with high ^{252}Cf -eq loadings using Tb as a chemical stand-in to determine appropriate quantities in preparation for in-cell work using ^{252}Cf . Using Tb as a chemical stand-in for ^{252}Cf , the maximum specific source strength outside of the hot cell was increased a factor of 10 from 0.22 to 2.25 mg/mm^3 .¹⁰² Chemical yields were confirmed with a ^{249}Cf radiotracer, the optimal precipitation recipe demonstrated a precipitation yield of $95.5 \pm 5.4 \%$ with no significant losses for a relatively high ^{252}Cf -eq specific loading of 4.4 mg/mm^3 as would be necessary for fabrication of an HDR source. This experiment should be repeated with an order-of-magnitude greater total ^{252}Cf -eq mass to reproduce in-cell conditions.

III. EXPERIMENTS FOR TESTING ^{252}Cf SOURCE METALLURGY

A. Introduction

After radiochemical production of ^{252}Cf source material, source wires must be physically constructed through metallurgical techniques. In the present work, mechanical testing was performed on precipitates formed from ^{252}Cf stand-ins and on arc melted products to better understand the processes and limitations of the current metallurgical techniques. Here, precipitates were tested as they best emulated the products obtained with ^{252}Cf in the radioactive hot-cells; arc melted products were also tested as their stoichiometry and

chemical state were better defined than the precipitate products, reducing variability relative to the precipitation process. A short background is provided on the current mechanical and fabrication techniques for ORNL ^{252}Cf medical source production.

B. ^{252}Cf Medical Source Background Information

Following chemical precipitation, the practice for industrial source fabrication starts by heating the precipitate to convert the californium oxalate to californium oxide (Cf_2O_3), after compressing the dried cermet precipitate into a stainless steel die. A small cylindrical pellet is formed, and this pellet is then heated in inert gases for an extended period so as to melt into a bead product. This spherical bead is then inserted into a jeweler's rolling mill to conform the bead to a wire geometry. There are a total of fifteen grooves in the jeweler's mill used at the CF, and these grooves produce a wire with a square cross-section. The wire's cross-sectional area ranges from 28.3 to 1.80 mm². The wire is passed multiple times through an individual groove setting. As the product is rolled from a larger groove to a smaller one, the product undergoes structural stress. Consequently, annealing is necessary in a 450°F oven for less than one hour under inert gas between every groove change. When the desired wire cross-section is obtained, the wire is divided into multiple lengths and is then assayed for source strength. After the initial ^{252}Cf wire assay, source wires are then inserted into an inner source capsule comprised of a Pt/Ir-10% mass alloy. Following tungsten inert gas (TIG) welding, the capsule is inserted into a weak bath of nitric acid for a period of days to leach any possible radionuclides from the outside surface as detected through leach solution assays. At this stage, the capsules are transferred to the intermediate clean cell environment for helium leak testing and visual inspection of hairline cracks. Next, the inner capsules are inserted into the outer capsules

and additional tests, e.g. TIG welding, smear testing, etc., are performed. Finally, a second, more accurate ^{252}Cf source strength assay is performed using a fission detector. To illustrate the arduousness of practical source fabricating techniques, one is reminded that manual operation of remote manipulators is necessary for all procedures within the hot cell. These efforts are performed at a distance of 3 meters through 1 meter of yellow zinc bromide and leaded-glass; consequently, a near-focus Maskutov telescope is necessary to visualize objects smaller than 1 cm.

C. Mechanical Testing of Sheathed and Unsheathed Precipitate Products

An assortment of sheathed and unsheathed precipitate products were rolled and swaged to determine the minimum wire size which could be fabricated. In the same manner as performed in the previous section, precipitation products were formed using Tb-loaded AHIB, and stock solutions of Pd, oxalic acid, and hydrazine. Wires were formed by drying, calcining, green pressing, and rolling the precipitate products. While wire products sheathed with stainless steel tubing were able to be rolled to smaller dimensions than the unsheathed samples, inherently smaller values for specific source strength and splintering of the sheaths after swaging discouraged study of sheathed precipitate products. It is desirable to use sheathed wires for added protection against radiation contamination; however, the sheath will subtend some of the capsule void volume which is later shown to limit the maximum ^{252}Cf loading. Both the jewelry mill and swaging tool were used to reduce the dimensions of unsheathed wires. For ^{252}Cf -equivalent specific source strengths of 0.18, 0.44, 0.86 and 2.25 mg/mm^3 , the minimum unsheathed wire size was 0.34, 0.39, 0.46, and 0.74 mm, respectively. Upon reduction of these wires, flaking of the wire surface and fracture occurred. For a proposed $\mu\text{Selectron } ^{252}\text{Cf}$ HDR source

with an inner capsule diameter of 0.6 mm, it appears that ^{252}Cf -equivalent specific source strengths of 0.86 mg/mm^3 are feasible.⁶⁵ For a proposed VariSource ^{252}Cf HDR source with an inner capsule diameter of 0.39 mm, a source wire diameter of 0.34 mm may be inserted.⁶⁶ Therefore, specific source strengths of $0.18 \text{ mg } ^{252}\text{Cf-eq/mm}^3$ may be feasible for the VariSource design.

D. Mechanical Testing of Arc Melted Tb and Gd Products

In these studies, Gd was used as a Cf substitute as Gd(III) has a similar bond length and ionic radius as that of Cf(III) .¹⁰⁷ Four samples, each with a volume of about 30 mm^3 , were obtained from TRL. These samples were: GdNi_5 , GdPd_3 , 50% molar $\text{GdPd}_3\text{:Pd}$, and 10% molar $\text{GdPd}_3\text{:Pd}$. These samples were fabricated through arc melting Gd powder with other powders with the correct stoichiometry. The alloy form of each sample, as compared with an oxide or other form, was confirmed using mass spectroscopy and x-ray crystallography.¹⁰⁷ Following initial annealing at 750°C in a carbon boat for four hours in an inert ($\text{He} + 5\% \text{ H}_2$) cover gas, rolling of these samples was performed to determine their relative machinability. The GdNi_5 and GdPd_3 samples were brittle and shattered when first placed in the jewelry roller in the CF cold lab. Though the nickel alloy was brittle, it should not be excluded based on this study as lower molar loadings (10 and 50%) of $\text{GdPd}_3\text{:Pd}$ demonstrated favorable ductility. Since Pd is regularly reworked at the CF, there is motivation to keep as many variables fixed as possible.

The other two samples were markedly more ductile. Using the jewelry mill and annealing stages between each jewelry mill groove, the 10% and 50% molar $\text{GdPd}_3\text{:Pd}$ samples were rolled down to diameters of 0.28 and 0.35 mm, respectively. Though only a few samples were examined in this study, results were promising for fabrication of ^{252}Cf

sources with high specific source strengths. Using Gd as a Cf stand-in, the equivalent specific source strengths of the 10% and 50% molar GdPd₃:Pd samples were 2.0 and 4.5 mg/mm³. For a proposed HDR μ Selectron source with an internal diameter of 0.6 mm, it appears that ²⁵²Cf specific source strengths exceeding 5 mg/mm³ are feasible.⁶⁵ However, arc melting for ²⁵²Cf source fabrication is not an established technique as Cf readily vaporizes during this process.¹⁰⁷ Also, Cf metal is not produced in cell because of its reactivity. Therefore, additional work to develop this fabrication technique is necessary.

E. Conclusion

Sheathed and unsheathed wire samples of varying Tb loadings were both rolled and swaged to determine the minimum wire diameter achievable. Due to an inherently smaller value for specific source strength using sheaths, and splintering of the sheaths after swaging, the unsheathed, singly-encapsulated source geometry was chosen. For this geometry, a Cf-equivalent specific source strength of 0.86 mg/mm³ was fabricated with a wire diameter of 0.46 mm. While an arc melted sample of 4.5 mg ²⁵²Cf-eq/mm³ was rolled to a wire diameter of less than 0.6 mm, the impact of the results from samples obtained from actual precipitations may be considered more promising as ²⁵²Cf fabrication techniques employing arc melting are currently not available, and may be problematic due to Cf vaporization. Though preliminary chemistry results with a Cf stand-in indicated upto 2.25 mg ²⁵²Cf-eq per mm³ may be achieved, the maximum loading was limited by the mechanical swaging techniques. Since the inner volumes of both proposed HDR sources are 0.3 mm³, only 260 and 50 μ g of ²⁵²Cf could be encapsulated for the proposed μ Selectron and VariSource HDR sources, respectively. Thus, a prototype HDR source with a minimum of 250 μ g ²⁵²Cf may be possible.

IV. ²⁵²Cf ALPHA DECAY AND ENCAPSULATION BURST CALCULATIONS

A. Introduction and Methodology

As ²⁵²Cf sources decay primarily via alpha decay (96.91%) with only a small spontaneous fission branching ratio (3.09%) producing neutrons, calculations are necessary for encapsulation burst pressures to demonstrate structural integrity at elevated temperatures for source registration with the U.S. Department of Transportation and the IAEA.^{55,103} Radioactive sources must exhibit structural integrity for a minimum of ten minutes at a temperature of 800°C for radiological safety during a fire.^{111,112} In applying the ideal gas law,¹¹³ it is evident from Equation 3 that an elevation in temperature, 298K to 1073K, would increase the internal pressure by a factor of 3.6 if one conservatively assumes the capsule exhibits negligible expansion or change in internal volume upon elevation to a temperature of 1073K and no increase in gas-phase components.

$$P_2 = P_1 \frac{n_2 T_2}{n_1 T_1} \quad (3)$$

where:

P	= gas pressure	[MPa]
n	= atoms in the gas volume	[moles]
T	= gas temperature	[K]

Through use of a thick-walled mechanical engineering approximation in calculating shear stress in Equation 4, burst conditions for the current ORNL-made ²⁵²Cf AT source and three proposed HDR sources are presented.¹¹⁴ The values of maximum shear stress for Pt/Ir-10% mass at 298K and 1073K are 55 ksi (379.2 MPa) and 35 ksi (241.3 MPa), respectively.¹¹⁵

$$(P_2 - P_1)_{MAX} = \left[\frac{(r_{outer}^2 - r_{inner}^2)}{2 r_{outer}^2} \right] \sigma_{MAX}(T) \quad (4)$$

where:

$$\begin{aligned}
 \Delta P_{MAX} &= \text{maximum permissible change in gas pressure} && [\text{MPa}] \\
 r_{outer} &= \text{outer tube radius} && [\text{mm}] \\
 r_{inner} &= \text{inner tube radius} && [\text{mm}] \\
 \sigma_{MAX}(T) &= \text{maximum shear stress at a given temperature} && [\text{MPa}]
 \end{aligned}$$

Using the aforementioned temperature change, these equations may be combined in Equation 5 to constrain the change in maximum pressure less than the maximum shear stress to prevent the encapsulation from bursting.

$$P_{298K} \left(\frac{3.6 n_{1073K}}{n_{298K}} - 1 \right)_{MAX} \left[\frac{2 r_{outer}^2}{(r_{outer}^2 - r_{inner}^2)} \right] \leq \sigma_{MAX}(1073K) \quad (5)$$

While this calculation is straightforward for a fixed number of gas atoms within the capsule, ^{252}Cf alpha decay increases the number of atoms and consequently the pressure over time. Thus, the corrected number of gas atoms, including helium production from ^{252}Cf decay, at a temperature of 1073K compared with the initial number of gas atoms at the source fabrication temperature of 298K may be related to the ^{252}Cf source strength in Equation 5. Here, conservative assumptions are made such as complete decay of the ^{252}Cf sources, a helium production branching ratio of 100%, and a 10% increase in the source strength to include alpha decay of all californium radionuclides in addition to that from ^{252}Cf .

$$n'_{1073K} = n_{298K} + \left[\frac{1.1 R S_0}{A} \right] \quad (6)$$

where:

$$\begin{aligned}
 S_0 &= \text{initial } ^{252}\text{Cf} \text{ source strength} && [\text{grams}] \\
 A &= ^{252}\text{Cf} \text{ mass number} && [\text{dimensionless}] \\
 R &= \text{helium branching ratio} && [\text{He atom/decay}] \\
 n &= \text{moles of gas in the contained volume} && [\text{moles}]
 \end{aligned}$$

Consequently, Equations 5 and 6 may be combined into Equation 7.

$$P_{298K} \left[3.6 \left(1 + \frac{1.2 R S_o}{A n_{298K}} \right) - 1 \right]_{MAX} \left[\frac{2 r_{outer}^2}{(r_{outer}^2 - r_{inner}^2)} \right] \leq \sigma_{MAX}(1073K) \quad (7)$$

B. ²⁵²Cf Burst Calculations for the ORNL-made AT Source

Currently available ORNL-made ²⁵²Cf AT medical sources have been conservatively approved for a source loading of 30 µg. These sources are doubly encapsulated with Pt/Ir-10% mass tubing which is welded at the ends. Following are calculations of burst conditions for both the AT inner and outer capsules.

AT Inner Capsule

The inner and outer diameters of the AT inner capsule are 1.35 and 1.75 mm, respectively, while the length of the inner void space housing the active source element is 15 mm.

Though this internal void space subtends 21.5 mm³, the 1.1 mm diameter active element displaces almost two-thirds (14.3 mm³) of the void volume leaving an inner capsule void space of approximately 7.2 mm³. Using Equation 7 and the above parameters, the maximum source strength before AT inner capsule burst was calculated at 9.9 mg ²⁵²Cf.

AT Outer Capsule

Should the AT inner capsule have a hairline crack or be subject to rupture, the AT outer capsule may offer structural integrity against ²⁵²Cf and fission product contamination. The inner and outer diameters of the AT outer capsule are 1.80 and 2.80 mm, respectively.

The length of the void space within the AT outer capsule is 19 mm, leaving 48.3 mm³.

However, the AT inner capsule subtends the majority of this volume, 41.3 mm³, leaving 7.0 mm³ of available void space in the AT outer capsule. Using Equation 7, the maximum source strength containable before the AT outer capsule would burst is approximately 14.0 mg. On comparison of the maximum containable ²⁵²Cf source strengths of the AT

inner (9.9 mg) and outer capsules (14.0 mg), it is evident that the outer capsule offers a additional protection. However, the current registered source strength limit (30 μg) for the AT sources is over a factor of 300 less than that achievable using the above formalism.

C. Burst Calculations for a Proposed $\mu\text{Selectron}$ ^{252}Cf HDR Source

The $\mu\text{Selectron}$ ^{192}Ir HDR source is singly-encapsulated with a 0.25 mm wall thickness comprised of type 316 stainless steel (316 SS).⁶⁵ The inner and outer diameters of the source are 0.6 and 1.1 mm, respectively. At 1073K, the maximum shear stress for 316 SS is approximately 47 MPa or 6.82 ksi.¹¹⁶ The inner void, length 3.7 mm, is filled with a 0.50 mm diameter active source with length 3.5 mm. Using Equation 7, the maximum calculated ^{252}Cf loading for a 0.30 mm³ void and the aforementioned geometry and materials was 138 μg .

D. ^{252}Cf Burst Calculations for a Proposed Pt/Ir-10% HDR VariSource Capsule

Data at elevated temperatures for nitinol were not readily available. Consequently, calculations for direct loading of ^{252}Cf into a VariSource HDR source wire were not possible. However, burst calculations using the VariSource geometry and Pt/Ir-10% as the capsule material were possible.⁶⁵ Here, a wire with 0.39 and 0.60 mm inner and outer diameters, respectively, housed a 10 mm long active source of 0.34 mm outer diameter.⁶⁶ Where the void volume was 0.29 mm³, a maximum ^{252}Cf source loading of 572 μg at 800°C was calculated using Equation 7. Though the void volume of the VariSource and $\mu\text{Selectron}$ sources were similar, the different wall thicknesses and capsule materials markedly varied the maximum calculated ^{252}Cf source loading before capsule burst.^{65,66}

E. ^{252}Cf Burst Calculations for a Proposed Pt/Ir-10% $\mu\text{Selectron}$ ^{252}Cf HDR Source

Here, the goal was to quantitatively realize the impact of using Pt/Ir-10% as compared to

316 SS for ^{252}Cf burst calculations. The identical geometry as used for the stainless steel $\mu\text{Selectron}$ calculations,⁶⁵ and the $\sigma(1073\text{K})_{\text{MAX}}$ value (241.3 MPa) for Pt/Ir-10% was employed. Using Equation 7, a maximum source strength of 720 μg was determined before the encapsulation would burst. This source strength using Pt/Ir-10% was a factor of 5.2 times greater than that obtained using 316 SS. Maximum ^{252}Cf loading results based on the aforementioned burst calculations for all sources are summarized in Table 3.

Table 3. Maximum ^{252}Cf source strength for a variety of medical sources.

source type	capsule material	$\sigma(1073\text{K})_{\text{MAX}}$ (MPa)	active source length (mm)	void space (mm^3)	max. ^{252}Cf (mg)
AT inner capsule	Pt/Ir-10%	241.3	15	7.2	9.9
AT outer capsule	Pt/Ir-10%	241.3	15	7.0	14.0
$\mu\text{Selectron}$ HDR	type 316 SS	47	3.5	0.30	0.138
$\mu\text{Selectron}$ HDR	Pt/Ir-10%	241.3	3.5	0.30	0.720
VariSource HDR	Pt/Ir-10%	241.3	10	0.29	0.572

F. Conclusion

In this study using a conservative burst formalism for helium production following decay of californium, a variety of source geometries and capsule materials were examined. For the ORNL-made AT sources, ^{252}Cf loadings of approximately 10 mg were possible.

Among the various parameters (chemistry, mechanical, He burst) examined in this chapter, the mechanical process was the most limiting for fabrication of a proposed ^{252}Cf HDR source.

CHAPTER 9

DISSERTATION SUMMARY AND FUTURE DIRECTIONS

I. DISSERTATION SUMMARY

While many aspects of ^{252}Cf dosimetry, moderated neutron energy spectra, and NCT applications were examined in this dissertation so as to provide a certain level of thoroughness, the implications of some results are more important than others. Following is a short discussion of the most notable results determined herein.

A. ^{252}Cf Dosimetry

Chapter 2 presented results of measurements and calculations of the ^{252}Cf fast neutron, photon, and total dose rates in water to muscle. The methodology, employing a GM counter with a relative neutron sensitivity of zero and application of ICRU 45 formalism, was original to ^{252}Cf . Significant differences in dose rates between those obtained in this study and those presented in the literature were explained by differences in nuclear data, experimental methodology, and dosimetry formalisms.

B. Clinical ^{252}Cf Dosimetry Formalism

Derivation of AAPM TG-43 dosimetric parameters, instead of use of out-dated along-away lookup tables, was performed for the first time for ^{252}Cf sources. The overwhelming dependence of the ^{252}Cf fast neutron dose on the geometry factor was demonstrated in Chapter 3, and radiation attenuation by encapsulation or source self-shielding was negligible as expected from the physical properties of the sources and radiation studied. Also, noteworthy was the derivation of the fast neutron dose distribution for a general ^{252}Cf source for a variety of clinically relevant media.

C. ^{252}Cf Thermal Neutron Flux

Chapters 4 through 6 examined the feasibility of enhancing ^{252}Cf brachytherapy with neutron capture therapy using ^{10}B and ^{157}Gd as NCT agents. In comparison to the fast neutron and photon dose components, the thermal neutron dose component was insignificant considering the NCT agent loadings currently obtainable. Notable was the dependence of *in vivo* thermal neutron flux on the phantom size and the NCT agent loading. There was substantial non-linearity in dose from neutron capture reactions with NCT agent loading. The ^{252}Cf fast neutrons, which deposited the majority of kerma, were not effected by considerable loadings of NCT agents. This was demonstrated through spectral analysis and implied that concurrent NCT enhanced ^{252}Cf brachytherapy may be performed without perturbation of the ^{252}Cf fast neutron dose component.

D. Health Physics of ^{252}Cf

Since the carcinogenic potential of ^{252}Cf neutrons is unknown, as determined from inspection of BEIR V in Chapter 7, there is concern to protect and shield personnel from ^{252}Cf radiation emissions. As expected, an analysis of a lead-doped acrylic material revealed hydrogen content to be the key factor for providing fast neutron shielding even though the lead significantly attenuated the ^{252}Cf photons. Experiments performed with ^{252}Cf Applicator Tube type sources using personnel monitoring badges showed exposures exceeding regulatory levels utilizing ALARA principles are likely if ^{252}Cf brachytherapy implants are performed with patient loads of 3 or more per month per radiation worker.

E. Source Development at ORNL

The current ^{252}Cf source fabrication procedure was examined in Chapter 8, and efforts were made to improve upon the process to increase the ^{252}Cf specific activity for

fabrication of a ^{252}Cf HDR source. Results of radiochemical and metallurgical studies suggested that a prototype HDR source with $860\ \mu\text{g}\ ^{252}\text{Cf}$ per mm^3 may be fabricated. A conservative, general equation relating source dimensions, capsule dimensions, and material compositions was formulated which permitted derivation of the maximum ^{252}Cf loading for a variety of source geometries. With the current helium burst calculation model, a prototype HDR source with ^{252}Cf source strengths exceeding $500\ \mu\text{g}$ is feasible.

A ^{252}Cf HDR source would be especially useful in developing countries where the quality of health care is less than in the U.S. as patients who present late in disease development, may benefit from the high LET radiation from ^{252}Cf instead of ^{137}Cs as currently used in developing countries. An HDR device employing a ^{252}Cf source may be feasible as it would be a low technology, low maintenance device in comparison to linear accelerators which demand regular technical support.

II. FUTURE DIRECTIONS

While the studies performed within this dissertation were extensive, an enormity of work still remains before clinical application of ^{252}Cf has been completely characterized. Of the many additional and important research tracks remaining, analysis of ^{252}Cf photon dosimetry in various phantoms using AAPM TG-43 formalism may be first on the list. Dosimetry calculations and measurements of $^1\text{H}(n,\gamma)^2\text{H}$ dose, $^{14}\text{N}(n,p)^{14}\text{C}$ dose, and possibly electron dose from ^{252}Cf and spontaneous fission products for an HDR source remain to be performed.

Since the fast neutron dose is significantly more radiobiologically effective than the low LET radiation from photons and electrons, and since the majority of absorbed dose is from fast neutrons, there is merit to measure the ^{252}Cf prompt neutron energy spectrum

more accurately than has currently been performed; this is a major project. A cascade evaporation model (CEM)¹¹⁷ or generalized Madland-Nix model (GMNM)¹¹⁸ for the ²⁵²Cf neutron energy spectrum may be more accurate than the Maxwellian used herein.

Progress in radiochemical research is necessary such as demonstration of high specific activity sources, possibly through ²⁵²Cf oxide source extrusion or development of new source matrices. One may also investigate new capsule or catheter designs to alter the ratio of high and low LET dose components. Measurement of helium production for a variety of ²⁵²Cf alloys will provide experimental evidence in support of a less constraining burst calculation model than is currently utilized for ²⁵²Cf source registration. These efforts would permit fabrication and registration of smaller ²⁵²Cf sources.

A multitude of radiobiological studies are necessary to examine dose and dose rate effects for the variable high and low LET dose components intrinsic to a ²⁵²Cf HDR source. This is project of enormous extent, and is necessary as the neutron RBE is variable with dose rate. Advances in computing power will most certainly facilitate Monte Carlo based, full physics modeling of patient-specific and/or inhomogeneity-specific treatment planning for ²⁵²Cf brachytherapy. The intent of this approach is to provide more accurate patient treatment planning than currently available.

It is clear that the future of ²⁵²Cf brachytherapy lies in use of a HDR source. Development and characterization of this therapy modality appears likely considering the scientific advances presented herein.

REFERENCES

- ¹J. F. Briesmeister MCNP- A General Monte Carlo N-Particle Transport Code System, Version 4B, LA-12625-M, (1997).
- ²D. J. Whalen, D. E. Hollowell, and J. S. Hendricks, "MCNP- photon benchmark problems," Los Alamos National Laboratory, LA12196, (1991).
- ³C. Wong, J. D. Anderson, P. Brown, L. F. Hansen, J. L. Kammerdiener, C. Logan, and B. Pohl, "Livermore pulsed sphere program: program summary through July 1971," Los Alamos National Laboratory, UCRL-51144, Rev. 1 (1972).
- ⁴W. Webster and C. Wong, "Measurement of the neutron emission spectra from spheres of N, O, W, ²³⁵U, ²³⁸U, and ²³⁹Pu, pulsed by 14-MeV neutrons," Los Alamos National Laboratory, UCID-17332, (1976).
- ⁵L. F. Hansen, J. D. Anderson, E. Goldberg, E. F. Plechaty, M. L. Stelts, and C. Wong, "Time spectra from spheres pulsed with 14-MeV neutrons," Nuc. Sci. Eng. **35**, 227-239 (1969).
- ⁶L. F. Hansen, J. D. Anderson, E. Goldberg, J. Kammerdiener, E. F. Plechaty, and C. Wong, "Predictions for neutron transport in air, based on integral measurements in nitrogen and oxygen at 14 MeV," Nuc. Sci. Eng. **40**, 262-282 (1970).
- ⁷M. L. Stelts, J. D. Anderson, L. F. Hansen, E. F. Plechaty, and C. Wong, "Spectra of fast neutrons from water pulsed with 14-MeV neutrons," Nuc. Sci. Eng. **40**, 53-56 (1971).
- ⁸R. T. Santoro, R. G. Alsmiller Jr., J. M. Barnes, and G. T. Chapman, "Calculation of neutron and gamma-ray energy spectra for fusion reactor shield design: comparison with experiment," Nuc. Sci. Eng. **78**, 259-272 (1981).
- ⁹G. P. Estes, R. C. Little, R. E. Seamon, and P. D. Soran, "Air transport in connection with the Hiroshima-Nagasaki dose reevaluation effort," Los Alamos National Laboratory, LA-9369-MS (1982).
- ¹⁰R. F. Rose and R. W. Roussin, "Shielding benchmark compilation," Brookhaven National Laboratory, BNL-19302 (1983).
- ¹¹J. K. Fox, L. W. Gilley, and E. R. Rohrer, "Critical mass studies, part 8: aqueous solutions of ²³³U," Oak Ridge National Laboratory, ORNL-2143 (1959).
- ¹²H. C. Paxton, "Los Alamos critical data," Los Alamos National Laboratory, LA-3067-MS (1975).
- ¹³H. F. Finn, N. L. Provost, O. C. Kolar, and G. A. Pierce, "Summary of experimentally

- determined plutonium array critical configurations," Lawrence Livermore National Laboratory, UCRL-51041 (1971).
- ¹⁴G. E. Hansen and H. C. Paxton, "Reevaluated critical specifications of some Los Alamos fast neutron systems," Los Alamos National Laboratory, LA-4208 (1969).
- ¹⁵D. J. Whalen, D. A. Cardon, J. L. Uhle, and J. S. Hendricks, "MCNP- neutron benchmark problems," Los Alamos National Laboratory, LA12212, (1991).
- ¹⁶C. C. Schlea and D. H. Stoddard, "Californium isotopes proposed for intracavitary and interstitial radiation therapy with neutrons," *Nature* **206**, 1058-1059 (1965).
- ¹⁷D. H. Stoddard, "Radiation properties of ²⁵²Cf," Savannah River Laboratory DP-986, (1965).
- ¹⁸J. P. Nichols, "Design data for ²⁵²Cf neutron source experiments," *Nuc. App.* **4**, 382-387 (1968).
- ¹⁹G. D. Oliver and C. N. Wright, "Dosimetry of an implantable ²⁵²Cf source," *Radiol.* **92**, 143-147 (1969).
- ²⁰V. Krishnaswamy, "Calculation of the dose distribution about ²⁵²Cf needles in tissue," *Radiol.* **98**, 155-160 (1971).
- ²¹V. Krishnaswamy, "Calculated depth dose tables for ²⁵²Cf sources in tissue," *Phys. Med. Biol.* **17**, 56-63 (1972).
- ²²V. Krishnaswamy, "Solid geometry versus plane geometry for ²⁵²Cf sources," *ibid*, 860.
- ²³V. Krishnaswamy, "Letter to the editor: Calculated depth dose for ²⁵²Cf seed source in tissue," *Phys. Med. Biol.* **19**, 886-888 (1974).
- ²⁴H. Märten, D. Richter, D. Seeliger, W. D. Fromm, R. Böttger, and H. Klein, "The ²⁵²Cf(sf) neutron spectrum in the 5- to 20-MeV energy range," *Nuc. Sci. Eng.* **106**, 353-366 (1990).
- ²⁵A. Chalupka, L. Malek, S. Tagesen, and R. Böttger, "Results of a low background measurement of the fission neutron spectrum from ²⁵²Cf in the 9- to 29-MeV energy range," *ibid*, 367-376.
- ²⁶L. L. Anderson, "Status of dosimetry for ²⁵²Cf medical neutron sources," *Phys. Med. Biol.* **18**, 779-799 (1973).
- ²⁷R. D. Colvett, H. H. Rossi, and V. Krishnaswamy, "Dose distribution around a ²⁵²Cf needle," *Phys. Med. Biol.* **17**, 356-364 (1972).

- ²⁸R. G. Fairchild, (Brookhaven National Laboratory, Upton, NY, 1968) 12452.
- ²⁹F. T. Cross, Unpublished data, Radiological Physics, (Battelle Memorial Institute, Pacific Northwest Laboratory, Richland, WA, 1971).
- ³⁰T. D. Jones and J. A. Auxier, "Absorbed dose and linear energy transfer distributions from therapeutic sources of ²⁵²Cf," *Phys. Med. Biol.* 17, 206-217 (1972).
- ³¹J. P. Windham, A. Shapiro, and J. G. Kereiakes, "Calculated neutron dose rates for implantable ²⁵²Cf sources," *ibid*, 493-502.
- ³²ICRU Clinical neutron dosimetry, Part I: determination of absorbed dose in a patient treated by external beams of fast neutrons, International Commission on Radiation Units and Measurements (ICRU 45, Bethesda, MD, 1989).
- ³³L. L. Anderson, "²⁵²Cf physics and dosimetry," *Nuc. Sci. App.* 2, 273-281 (1986).
- ³⁴R. Nath, L. L. Anderson, G. Luxton, K. A. Weaver, J. F. Williamson, and A. S. Meigooni, "Dosimetry of interstitial brachytherapy sources: Recommendations of the AAPM Radiation Therapy Committee Task Group No. 43," *Med. Phys.* 22, 209-234 (1995).
- ³⁵A. Geist, A. Beguelin, J. Dongarra, W. Jiang, R. Manchek, and V. Sunderam, *PVM: Parallel Virtual Machine- A User's Guide and Tutorial for Networked Parallel Computing* (The MIT Press, Cambridge, MA, 1994).
- ³⁶F. Van den Heuvel, M. J. Rivard, J. G. Wierzbicki, and D. P. Ragan, "Implementation of distributed computing for Monte Carlo simulations using PVM in a low tech environment," *MEDICAL PHYSICS* 1997, Obninsk, Russia, 90-91 (1997).
- ³⁷M. J. Rivard, J. G. Wierzbicki, and F. Van den Heuvel, "Calculations of the ²⁵²Cf neutron spectrum in water for various positions and loadings of ¹⁰B and ¹⁵⁷Gd," in *American Nuclear Society Radiation Protection and Shielding Division: Technologies for the New Century*, edited by D.T. Ingersoll (ANS Inc., La Grange Park, IL, 1998), 2, pp. 211-218.
- ³⁸ICRU Tissue substitutes in radiation dosimetry and measurement, International Commission on Radiation Units and Measurements Bethesda, (ICRU 44, Bethesda, MD, 1989).
- ³⁹M. Awschalom, I. Rosenberg, and A. Mravca, "Kerma for various substances averaged over the energy spectra of fast neutron therapy beams: a study in uncertainties," *Med. Phys.* 10, 395-409 (1983).
- ⁴⁰V. E. Lewis and J. B. Hunt, "Fast neutron sensitivities of Geiger-Mueller counter gamma dosimeters," *Phys. Med. Biol.* 23, 888-893 (1978).

- ⁴¹J. J. Broerse, B. J. Mijnheer, and J. R. Williams, "European protocol for neutron dosimetry for external beam therapy," *British J. of Radiology* **54**, 882-898 (1981).
- ⁴²CRC, *CRC handbook of chemistry and physics* 65th edition (CRC Press Inc., Boca Raton, FL, 1985).
- ⁴³G. F. Knoll, "General properties of radiation detectors," in *Radiation detection and measurement* 2nd edition (John Wiley & Sons, New York, 1989), pp. 103-130.
- ⁴⁴R. Gastorf, L. Humphries, and M. Rozenfeld, "Cylindrical chamber dimensions and the corresponding values of A_{WALL} and $N_{GAS}/(N_X A_{ion})$," *Med. Phys.* **13**, 751-754 (1986).
- ⁴⁵L. J. Goodman and J. J. Coyne, "Wn and neutron kerma for methane-based tissue-equivalent gas," *Radiat. Res.* **83**, 491 (1980).
- ⁴⁶F. M. Waterman, F. T. Kuchnir, L. S. Skaggs, R. T. Kouzes, and W. H. Moore, "Energy dependence of the neutron sensitivity of C-CO₂, Mg-Ar, and TE-TE ionisation chambers," *Phys. Med. Biol.* **24**, 721 (1979).
- ⁴⁷R. L. Maughan, J. C. McDonald, B. D. Michael, and I. Ma., "A measurement of W_N/e for methane-based tissue-equivalent gas in a d(4)-Be neutron field," *Phys. Med. Biol.* **28**, 1105-1112 (1983).
- ⁴⁸J. C. Yanch and R. G. Zamenhof, "Dosimetry of ²⁵²Cf sources for neutron radiotherapy with and without augmentation by boron neutron capture therapy," *Rad. Res.* **131**, 249-256 (1992).
- ⁴⁹J. Zoetelief, C. A. Engels, J. J. Broerse, and B. J. Mijnheer, "Effect of finite size of ion chambers used for neutron dosimetry," *Phys. Med. Biol.* **25**, 1121 (1980).
- ⁵⁰M. Awschalom, I. Rosenberg, and R. K. Ten Haken, "A new look at displacement factor and point of measurement corrections in ionization chamber dosimetry," *Med. Phys.* **10**, 307-313 (1983).
- ⁵¹D. T. L. Jones, "The neutron sensitivity of a GM counter between 0.5 and 8 MeV," in *Radiation protection, 4th symposium on neutron dosimetry*, edited by G. Burger and H. G. Erbert (EUR 7448, Munich, Germany, 1981), **2**, 409-419.
- ⁵²M. J. Rivard, J. G. Wierzbicki, F. Van den Heuvel, and R. C. Martin, "Calculated variation in neutron spectra for water, brain, and muscle from a ²⁵²Cf point source," in *American Nuclear Society Radiation Protection and Shielding Division*, *ibid*, **2**, pp. 219-225.
- ⁵³R. S. Caswell, J. J. Coyne, and M. L. Randolph, "Kerma factors of elements and compounds for neutron energies below 30 MeV," *Intl. J. Appl. Rad. Isot.* **33**, 1227-1262

(1982).

⁵⁴R. Nath, L. L. Anderson, J. A. Meli, A. J. Olch, J. A. Stitt, and J. F. Williamson, "Code of practice for brachytherapy physics: Report of the AAPM Radiation Therapy Committee Task Group No. 56," *Med. Phys.* **24**, 1557-1598 (1997).

⁵⁵J. B. Knauer Jr. and R. C. Martin, "Californium-252 production and neutron source fabrication," in *Californium-252: Isotope for 21st Century Radiotherapy*, edited by J. G. Wierzbicki (Kluwer Academic Publishers, Netherlands, 1997) **29**, pp. 7-24.

⁵⁶J. G. Wierzbicki, M. J. Rivard, and W. A. Roberts, "Physics and dosimetry of clinical ²⁵²Cf sources," *ibid*, pp. 25-53.

⁵⁷ICRP Report of the task group on Reference Man, International Commission on Radiation Protection, (ICRP 23, Pergamon Press, New York, 1975).

⁵⁸Y. Maruyama, J. G. Wierzbicki, B. M. Vtyurin, and K. Kaneta, "²⁵²Cf neutron brachytherapy," in *Principles and Practices of Brachytherapy* edited by S. Nag (Futura, Pub. Co., Armonk, New York, 1997), pp. 649-687.

⁵⁹Y. Maruyama, J. R. Van Nagell, J. Yoneda, E. S. Donaldson, H. H. Gallian, D. Powell, and R. J. Kryscio, "A review of ²⁵²Cf neutron brachytherapy for cervical cancer," *Cancer* **68**, 1189-1197 (1991).

⁶⁰J. Fontanesi, private communication, WSU, September, 1995.

⁶¹L. A. Marjina, V. N. Kiseleva, M. I. Nechushkin, V. N. Chekhonadsky, and G. P. Elisyutin, "The results of treatment of patients with endometrial cancer and carcinoma cervix using ²⁵²Cf HDR," in *Californium-252: Isotope for 21st Century Radiotherapy*, edited by J. G. Wierzbicki (Kluwer Academic Publishers, Netherlands, 1997) **29**, pp. 115-130.

⁶²O. N. Denisenko, V. N. Ivanov, V. A. Kozlov, V. O. Sidorchenkov, A. A. Omarov, I. M. Chernichenko, and V. N. Chekhonadsky, "Dosimetry and treatment planning in high dose rate ²⁵²Cf brachytherapy," *ibid*, 221-231.

⁶³A. G. Konoplyannikov, "Biological effects of gamma-neutron radiation ²⁵²Cf or fission neutrons from the BR-10 reactor on tumor and normal cells and tissues," *ibid*, 257-261.

⁶⁴M. J. Rivard, J. G. Wierzbicki, F. Van den Heuvel, R. C. Martin, and R. R. McMahon, "Clinical brachytherapy with neutron emitting ²⁵²Cf sources and adherence to AAPM TG-43 dosimetry protocol," *Med. Phys.* **26**, xxx-xxx (1999).

⁶⁵J. F. Williamson and Z. Li, "Monte Carlo aided dosimetry of the microSelectron pulsed and high dose-rate ¹⁹²Ir sources," *Med. Phys.* **22**, 809-819 (1995).

- ⁶⁶A. S. Meigooni, M. T. Kleiman, J. L. Johnson, D. Mazloomdoost, and G. S. Ibbott, "Dosimetric characteristics of a new high-intensity ¹⁹²Ir source for remote afterloading," *Med. Phys.* **24**, 2008-2013 (1997).
- ⁶⁷L. L. Meisberger, R. Keller, and R. J. Shalek, "The effective attenuation in water of the gamma rays of ¹⁹⁸Au, ¹⁹²Ir, ¹³⁷Cs, ²²⁶Ra, and ⁶⁰Co," *Radiology* **90**, 953-957 (1968).
- ⁶⁸W. H. Press, S. A. Teukolsky, W. T. Vetterling, and B. P. Flannery, "Root finding and nonlinear sets of equations," in *Numerical Recipes in C: The Art of Scientific Computing* (Cambridge University Press, New York, 1988) pp. 347-393.
- ⁶⁹ASTM Standard test method for determining thermal neutron reaction and fluence rates by radioactivation techniques, American Society for Testing and Materials (ASTM E 262-86e, Philadelphia, PA 1991).
- ⁷⁰E. Browne and R. B. Firestone, *Table of Radioactive Isotopes* edited by V. S. Shirley (John Wiley & Sons, New York; 1986).
- ⁷¹Y. S. Horowitz, "The theoretical and microdosimetric basis of thermoluminescence and applications to dosimetry," *Phys. Med. Biol.* **26**, 765-824 (1981).
- ⁷²J. A. B. Gibson, "The relative tissue-kerma sensitivity of thermoluminescent materials to neutrons: a review of available data," (CENDOS EUR 10105, Harwell, U.K., 1985).
- ⁷³J. G. Wierzbicki, Y. Maruyama, and C. W. Alexander, "²⁵²Cf for teletherapy and thermalized ²⁵²Cf neutrons for brachytherapy," *Nuc. Sci. App.* **4**, 361-366 (1991).
- ⁷⁴J. G. Wierzbicki, Y. Maruyama, and C. W. Alexander, "Boron neutron capture enhancement in ²⁵²Cf brachytherapy," in *Progress in Neutron Capture Therapy for Cancer* edited by B. J. Allen, D. E. Moore, and B. V. Harrington (Plenum Press, New York, 1992), pp. 187-189.
- ⁷⁵J. G. Wierzbicki, Y. Maruyama, and A. T. Porter, "Measurement of augmentation of ²⁵²Cf implant by ¹⁰B and ¹⁵⁷Gd neutron capture," *Med. Phys.* **21**, 787-790 (1994).
- ⁷⁶J. G. Wierzbicki, private communication, Wayne State University, April, 1998.
- ⁷⁷R. G. Zamenhof, B. W. Murray, G. L. Brownell, G. R. Wellum, and E. I. Tolpin, "Boron neutron capture therapy for the treatment of cerebral gliomas: I. theoretical evaluation of the efficacy of various neutron beams," *Med. Phys.* **2**, 47-60 (1975).
- ⁷⁸G. M. Morris, J. A. Coderre, J. W. Hopewell, P. L. Micca, N. M. Nawrocky, H. B. Liu, and A. Bywaters, "Response of the central nervous system to boron neutron capture irradiation: Evaluation using rat spinal cord model," *Radiother. Oncol.* **32**, 249-255 (1994).

⁷⁹J. A. Coderre, D. D. Joel, P. L. Micca, N. M. Nawrocky, and D. N. Slatkin, "Control of intracerebral gliosarcomas in rats by boron neutron capture therapy with p-boronophenylalanine," *Radiat. Res.* **129**, 290-296 (1992).

⁸⁰F. H. Attix, "Cavity theory", in *Introduction to radiological physics and radiation dosimetry* (John Wiley & Sons, New York, 1986.)

⁸¹J. C. Yanch, R. G. Zamenhof, J. G. Wierzbicki, and Y. Maruyama, "Comparison of dose distributions with ¹⁰B augmented sources of ²⁵²Cf obtained by Monte Carlo simulation and by experimental measurement," *ibid*, 191-194.

⁸²R. C. Little, private communication, T-2 LANL, April 1998.

⁸³F. H. Attix, "Dosimetry fundamentals", in *Introduction to radiological physics and radiation dosimetry* (John Wiley & Sons, New York, 1986.)

⁸⁴Nuclides and isotopes, chart of the nuclides 14th Ed. (GE Nuclear Energy, San Jose, CA, 1989).

⁸⁵M. J. Rivard, D. S. Waid, J. G. Wierzbicki, and M. Yudelev, "Measured gadolinium neutron capture dose enhancement using ²⁵²Cf brachytherapy sources," in *Advances in Neutron Capture Therapy* edited by B. Larsson, J. Crawford, and R. Wienreich (Elsevier Science, Netherlands, 1997) **2**, pp. 430-435.

⁸⁶J. Stepanek, "Radiation spectrum of ¹⁵⁸Gd and radial dose distribution," in *Advances in Neutron Capture Therapy* edited by B. Larsson, J. Crawford, and R. Wienreich (Elsevier Science, Netherlands, 1997) **2**, pp. 425-429.

⁸⁷R. M. Brugger and J. A. Shih, "Evaluation of gadolinium-157 as a neutron capture therapy agent," *Stralenterapie Onkol.* **165**, 153 (1989).

⁸⁸National Academy of Sciences, National Research Council, *Health effects of exposure to low levels of ionizing radiation* (BEIR V, National Academy Press, Washington, D.C., 1990), pp. 9-64.

⁸⁹National Academy of Sciences, National Research Council, "Risks of cancer- all sites," *ibid*, pp. 161-241.

⁹⁰C. J. Shellabarger, D. Chmelevsky, A. M. Kellerer, J. P. Stone, and S. Holtzman, "Induction of mammary neoplasms in the ACI rat by 430-keV neutrons, x-rays, and diethylstilbestrol," *J. Natl. Cancer Inst.* **69**, 1135-1146 (1982).

⁹¹International Commission on Radiation Units and Measurements, "The quality factor in radiation protection," *Report of joint task group of the ICRP and the ICRU* (ICRU Report 40, Bethesda, MD, 1986).

- ⁹²A. Han, C. K. Hill, and M. M. Elkind, "Enhanced transformation of mouse 10T $\frac{1}{2}$ cells by 12-O-tetradecanolyphorbol-13-acetate following exposure to x-rays or to fission-spectrum neutrons," *Cancer Res.* **42**, 585-589 (1982).
- ⁹³J. M. Feola, Y. Maruyama, A. Pattarasumunt, and R. M. Kryscio, "²⁵²Cf Leukemogenesis in C57BL Mice," *Int. J. Radiat. Oncol. Biol. Phys.* **13**, 69-74 (1987).
- ⁹⁴National Academy of Sciences, National Research Council, "Radiogenic cancer at specific sites," *ibid*, pp. 242-351.
- ⁹⁵Y. Maruyama and J. M. Feola, "²⁵²Cf Leukemogenesis in C57BL Mice," *Nuc. Sci. App.* **4**, 139-147 (1991).
- ⁹⁶Nuclear Associates *Clear-Pb[®] technical data literature and product specifications of Kyowaglas-XA H* (Victoreen, Inc., New York, 1998).
- ⁹⁷J. H. Hubbell and S. M. Seltzer, "Tables of x-ray mass attenuation coefficients and mass energy-absorption coefficients 1 keV to 20 MeV for elements Z=1 to 92 and 48 additional substances of dosimetric interest," *Rad. Res.* **136**, 147 (1993).
- ⁹⁸G. F. Knoll, "Counting statistics and error prediction," in *Radiation detection and measurement* 2nd edition (John Wiley & Sons, New York, 1989), pp. 65-102.
- ⁹⁹A. C. Melissinos, "Elements from the theory of statistics," in *Experiments in modern physics* (Academic Press, New York, 1966), pp. 438-487.
- ¹⁰⁰J. H. Hubbell, "Photon mass attenuation coefficients and energy absorption coefficients from 1 keV to 20 MeV," *Intl. J. Appl. Rad. Isot.* **33**, 1269 (1982).
- ¹⁰¹International Commission on Radiological Protection *Recommendations of the International Commission on Radiological Protection* (ICRP Report 60, Pergamon Press, Oxford, 1991) 21.
- ¹⁰²R. C. Martin, R. R. Laxson, J. H. Miller, J. G. Wierzbicki, M. J. Rivard, and D. L. Marsh, "Development of high-activity ²⁵²Cf sources for neutron brachytherapy," *Appl. Radiat. Isot.* **48**, 1567-1570 (1997).
- ¹⁰³G. Friedlander, J. W. Kennedy, and J. M. Miller, "Techniques in nuclear chemistry," in *Nuclear and Radiochemistry*, 2nd ed. (John Wiley & Sons, New York, 1964), pp. 388-455.
- ¹⁰⁴Guide for fabricating and handling ²⁵²Cf sources (U.S. Atomic Energy Commission, Savannah River Operations Office SRO-153, Aiken, South Carolina, 1971).
- ¹⁰⁵R. R. Laxson, private communication, CF-ORNL, June 1996.

- ¹⁰⁶J. B. Knauer Jr., private communication, REDC-ORNL, August 1996.
- ¹⁰⁷R. G. Haire, private communication, TRL-ORNL, August 1996.
- ¹⁰⁸G. Friedlander, J. W. Kennedy, and J. M. Miller, "Tracers in chemical applications," in *Nuclear and Radiochemistry*, *ibid*, 191-220.
- ¹⁰⁹C. W. Alexander, private communication, REDC-ORNL, August 1996.
- ¹¹⁰R. R. McMahon, private communication, CF-ORNL, August 1996.
- ¹¹¹Code of Federal Regulations, "Research and special programs administration," in *Transportation* (49 CFR, section 173-469, U.S. Department of Transportation, Washington D.C., 1994).
- ¹¹²W. R. McDonell, "Integrity of ²⁵²Cf neutron sources after long-term service in normal and elevated temperature environments," in *Californium-252 Source Technology, Scientific and Industrial Applications* (CONF-760436, Paris, 1976), 2, pp. 183-212.
- ¹¹³C. Kittel and H. Kroemer, "Chapter 6: ideal gas," in *Thermal Physics*, 2nd ed. (W. H. Freeman and Co., San Francisco, 1980), pp. 151-180.
- ¹¹⁴W. F. Riley and L. W. Zachary, "Axial loading applications and pressure vessels," in *Introduction to Mechanics of Materials* (John Wiley & Sons, New York, 1989), pp. 87-142.
- ¹¹⁵P. H. Permar, "Safety analysis of doubly-encapsulated ²⁵²Cf medical sources (models ALC, SALC, and AT)," Savannah River Laboratory, SRL-76002 (1977).
- ¹¹⁶D. Peckner and I. M. Bernstein, "Mechanical and physical properties of austenitic chromium-nickel stainless steels at ambient and elevated temperatures," in *Handbook of Stainless Steels* (McGraw-Hill Book Co., New York, 1963).
- ¹¹⁷R. Böttger, H. Klein, A. Chalupka, and B. Strohmaier, "Investigation of the spectral fluence of neutrons from spontaneous fission of ²⁵²Cf(sf) by means of time of flight spectroscopy," *Nuc. Sci. Eng.* **106**, 377-398 (1990).
- ¹¹⁸D. G. Madland and J. R. Nix, "Prompt fission neutron spectra and average prompt neutron multiplicities," in *NEANDC Specialist's Meeting on Yields and Decay Data of Fission Product Nuclides* edited by R. E. Chrien and T. W. Burrows (Brookhaven National Laboratory, Upton, NY, 1984) **51778**, pp. 423-448.

ABSTRACT

NEUTRON DOSIMETRY, MODERATED ENERGY SPECTRUM, AND NEUTRON CAPTURE THERAPY FOR ^{252}Cf MEDICAL SOURCES

by

MARK JOSEPH RIVARD

December 1998

Advisor: Dr. Jacek G. Wierzbicki

Major: Medical Physics

Degree: Doctor of Philosophy

Examination of neutron dosimetry for ^{252}Cf has been conducted using calculative and experimental means. Monte Carlo N-Particle (MCNP) transport code was used in a distributed computing environment as a parallel virtual machine (PVM) to determine the absorbed neutron dose and neutron energy spectrum from ^{252}Cf in a variety of clinically relevant materials. Herein, a Maxwellian spectrum was used to model the ^{252}Cf neutron emissions within these materials.

^{252}Cf mixed-field dosimetry of Applicator Tube (AT) type sources was measured using 1.0 and 0.05 cm³ tissue-equivalent ion chambers and a miniature GM counter. A dosimetry protocol was formulated similar that of ICRU 45. The ^{252}Cf AT neutron dosimetry was determined in the cylindrical coordinate system formalism recommended by the AAPM Task Group 43. These results demonstrated the overwhelming dependence of dosimetry on the source geometry factor as there was no significant neutron attenuation within the source or encapsulation.

Gold foils and TLDs were used to measure the thermal flux in the vicinity of ^{252}Cf

AT sources to compare with the results calculated using MCNP. As the fast neutron energy spectrum did not markedly change at increasing distances from the AT source, neutron dosimetry results obtained with paired ion chambers using fixed sensitivity factors agreed well with MCNP results and those in the literature. Calculations of moderated ^{252}Cf neutron energy spectrum with various loadings of ^{10}B and ^{157}Gd were performed, in addition to analysis of neutron capture therapy dosimetry with these isotopes.

Radiological concerns such as personnel exposure and shielding of ^{252}Cf emissions were examined. Feasibility of a high specific-activity ^{252}Cf HDR source was investigated through radiochemical and metallurgical studies using stand-ins such as Tb, Gd, and ^{249}Cf . Issues such as capsule burst strength due to helium production for a variety of proposed HDR sources were addressed. A recommended ^{252}Cf source strength of at least 1 mg was necessary for fabrication of a ^{252}Cf HDR source.

AUTOBIOGRAPHICAL STATEMENT

MARK JOSEPH RIVARD

EDUCATION

- 1992 Bachelor of Science in Engineering and Physics, University of Michigan, Ann Arbor
1995 Master of Science in Radiological Physics, Wayne State University, Detroit, MI

PROFESSIONAL APPOINTMENTS

- 1988-1990 Laboratory Assistant, University of Michigan
1990-1995 Research Assistant, University of Michigan & FERMILAB
1996-1998 ASTRO/AAPM Clinical Medical Physics Resident,
Department of Radiation Oncology, Harper Hospital, Detroit, MI
1996-1998 Department of Energy Predoctoral Research Fellow,
Chemical Technology Division, Oak Ridge National Laboratory, TN

MEMBERSHIPS IN PROFESSIONAL SOCIETIES

- American Association of Physicists in Medicine
American Brachytherapy Society
American Physical Society
American Society of Therapeutic Radiology and Oncology
International Society for Neutron Capture Therapy
Great Lakes Chapter of American Association of Physicists in Medicine

HONORS AND AWARDS

- 1995 Graduate Student Research Award, Oak Ridge National Laboratory
1995-1998 Graduate Professional Scholarship, Wayne State University, MI
1996-1997 Travel Contract Award, Oak Ridge Institute for Science and Education, TN
1996 Professional Internship Program, Oak Ridge National Laboratory, TN
1996 International Delegate Travel Award, The Paul Scherrer Institute,
University of Zurich, and the Institute for Medical Radiobiology, Switzerland
1996-1998 Department of Energy Laboratory Graduate Program Award,
Oak Ridge Institute for Science and Education, TN
1997 Dissertation Research Support Award, Wayne State University, MI
1997 American College of Medical Physics Graduate Scholarship Award
1997-1998 Blue Cross Blue Shield of Michigan Doctoral Student Award, SAP #276/97
1997 External Graduate Support Award, Wayne State University, MI
1998 Neuroscience Travel Award, School of Medicine, Wayne State University, MI

PUBLICATIONS

- Sixteen articles as first author, fifteen articles as co-author
Nineteen abstracts as first author, seventeen abstracts as co-author
Two book chapters as co-author